Level Set and Boundary Element Method for Reconstruction of Phase Boundaries in Capacitance Tomography

Dipl.-Ing. Bernhard Kortschak

---

submitted as thesis to attain the academic degree ”Dr. techn.” at

Graz University of Technology

Institute of Electrical Measurement and

Measurement Signal Processing

supervisor:

Univ.-Doz. Dipl.-Ing. Dr.techn. Bernhard Brandstätter

Graz, April 2006

Abstract

Electrical Capacitance Tomography (ECT) is a reliable tool for imaging industrial processes. Basically, it reveals information on the interior distribution of the material in a pipe or vessel. Due to its soft-field modality and due to the ill-posed nature of the involved inverse problem, only a limited spatial resolution is obtained. Especially the reconstruction of sharp phase boundaries is challenging. In many applications, however, an accurate determination of these boundaries is necessary, for instance the identification of mixing zones in stirred reactors, interface measurements in complex separation processes, measurements of two or more phase boundaries in pipes with applications to multi-phase flow measurements, and non-invasive testing of materials to find e.g. inclusions. Additionally, the identification of phase sizes and boundaries within vessels and pipelines provides information on fundamental reaction kinetics and it can be used for model validations and for finding out an optimal geometry of the equipment.

Commonly used imaging techniques yield blurred images with less spatial resolution. In this work a shape reconstruction technique is suggested for piecewise constant permittivities. The level set method, which is utilized to describe and evolve non-trivial contours, is combined with the boundary element method, which solves field problems with high accuracy. The Gauss-Newton method is applied to obtain a fast convergence and yields an imaging technique, which reconstructs the involved materials simultaneously to their boundaries in an iterative optimization process. Due to the treatment of physical constraints for the material value and for the geometry, a stable optimization can be achieved under all kinds of potential conditions. The measurement noise is considered as well and improves the reconstruction of real world measurement data considerably. Experimental results validate the good performance and accuracy of the proposed imaging technique. As far as the author knows it is the first treatment of the inverse problem in ECT by the combination of boundary elements and the level set method.

The application of a single type of sensor is not the only opportunity for a tomography system. In this work a dual-mode system is considered as combination of ECT and ultrasonic reflection tomography (URT). The information about edges from URT provides a physically meaningful regularization (a priori information) for reconstruction of ECT data. This new technique for data fusion performs, based on the level set method, an edge detection of an URT image simultaneously to the ECT reconstruction. This yields closed contours for the URT and improved accuracy of boundaries in ECT.

Keywords: Boundary Element Method, Capacitance Tomography, Level Set Method, Inverse Problems

Kurzfassung

Elektrische Kapazitätstomografie (ECT) ist ein zuverlässiges, bildgebendes Verfahren für industrielle Prozesse. Grundsätzlich erhält man Schnittbilder der Materialverteilung in Rohren oder Behältern. Aufgrund der so genannten „soft-field“ Eigenschaft und der „Schlechtgestelltheit“ des Problems ist nur eine beschränkte Auflösung möglich. Insbesondere die Rekonstruktion von scharfen Materialübergängen ist eine Herausforderung. Diese ist in vielen Anwendungen erwünscht, wie z.B. bei der Separation von Stoffen oder beim Testen von Materialien auf Einschlüsse. Zusätzlich kann eine Rekonstruktion von Phasengrenzen verwendet werden, um Modelle zu validieren oder um optimale Geometrien von Anlagen zu entwickeln.

Die normalerweise verwendeten bildgebenden Verfahren zeigen nur verschwommene Bilder mit einer begrenzten örtlichen Auflösung. In dieser Arbeit wird eine Rekonstruktionsmethode für stückweise konstante Leitfähigkeiten vorgestellt. Diese basiert auf der Kombination der Level-Set Methode, um Deformationen von komplexen Konturen und Formen zu beschreiben, mit der Randelemente Methode, um das Feldproblem mit guter Genauigkeit zu lösen. Die Gauss-Newton Methode wird für eine schnelle Konvergenz verwendet und die Materialwerte werden im iterativen Prozess simultan mit der Form rekonstruiert. Physikalische Randbedingungen, wie die der Materialwerte oder der Geometrie, werden mit der Active-Set Methode berücksichtigt um eine stabile Optimierung unter allen möglichen Bedingungen zu garantieren. Zusätzlich wird Messrauschen berücksichtigt und das beschriebene Verfahren wird anhand von Messungen validiert. So weit es dem Autor bekannt ist, ist das die erste Behandlung des Inversen Problems in der ECT mit der Kombination der Level-Set und der Randelemente Methode.

Die Anwendung eines einzelnen Messprinzips ist nicht die alleinige Möglichkeit eines Tomografie Systems. In dieser Arbeit wird ein System mit der Kombination von ECT mit Ultraschall Reflexions Tomografie (URT) betrachtet. Die Information über Materialgrenzen stellt eine physikalisch sinnvolle Regularisierung (a priori Information) für die ECT Rekonstruktion bereit. Diese neue Technik der Fusion von Sensordaten führt, basierend auf der Level-Set Formulierung, eine Kantendedektion vom URT Bild simultan zur ECT Rekonstruktion durch. Durch diese Fusion erhält man geschlossene Ränder in der URT und verbesserte Genauigkeit der Materialgrenzen in der ECT.

Schlagwörter: Randelemente Methode, Kapazitätstomografie, Level-Set Methode, Inverse Probleme

Danksagung

Diese Dissertation entstand im Laufe der Jahre 2004-2006 am Institut für Elektrische Meßtechnik und Meßsignalverarbeitung an der Technischen Universität Graz. Diese Arbeit ist eine Fortsetzung meiner Diplomarbeit. Schon im Herbst 2002 begann ich mich mit der elektrischen Kapazitätstomografie zu befassen.

Ganz besonders möchte ich meinem Betreuer Univ.-Doz. Bernhard Brandstätter für die großartige Unterstützung in den letzten dreieinhalb Jahren danken. Bedanken möchte ich mich auch bei Univ.-Prof. Georg Brasseur und allen anderen am Institut, die mich bei der Arbeit unterstützt haben. In diesem Zusammenhang möchte ich Dipl.-Ing. Hannes Wegleiter erwähnen, der einen hervorragenden ECT-Sensor gebaut hat. Mit dessen Messwerten sind die Rekonstruktionen in dieser Arbeit entstanden. Auch möchte ich mich bei Univ.-Prof. Hermann Scharfetter für die Durchsicht dieser Arbeit und für die anregenden Diskussionen bedanken.

Letztendlich möchte ich meinen Eltern, meinen Studienkollegen, all meinen Freunden und meiner Freundin Christina für Mithilfe, Unterstützung und Verständnis danken.

Graz, im April 2006 Bernhard Kortschak

Contents

Chapter 1

Introduction

Tomography and its non-invasive principle of imaging are not restricted to the medical field. Over the last decade, industrial tomography systems have been developed and they are used for many industrial applications as a reliable tool for imaging [23, 64, 71]. Basically a number of sensors are mounted around a pipe or vessel and they reveal information on the interior distribution of material. The output signals depend for example on the position of the boundaries of different components. This spatial variation of the parameter of interest is represented as a cross-sectional image. This process is known as image reconstruction and the obtained image is further analyzed quantitatively for example to improve process control or to develop models for individual processes. Tomography systems are used in a wide field of industrial applications, for example (see [23, 64, 71])

- imaging of multi-phase processes such as for conveying systems (pneumatic conveying for particulate solids, powders, and flakes), for oil field pipelines (component fraction and velocity distribution in flow regimes for control purposes), in centrifugal or gravity separators (liquid/liquid, gas/liquid mixing, and solid/liquid separation), and hydro-cyclone imaging,
- measurement and control of multi-phase flows (e.g. [27, 32]) to study the dynamic behavior in fast flows or to measure mass flow rates in complex regimes,
- in pipeline conveying (slug flow) to control the air flow to prevent blockage and to decrease the energy demand and pipeline erosion,
- monitoring of filtration processes,
- flame imaging in an internal combustion engine cylinder,
- in stirred tank reactors to get information of the effective mixing zone,
- to visualize gas or liquid bubbles in fluidized bed, and
- for material testing to find inclusions and to give quality characteristics.

One sensor method beside many others is electrical tomography, which is based on measurement of capacitance (ECT), resistance (ERT), or magnetic induction (MIT). The

term Electrical Impedance Tomography (EIT) is justified if the complex impedance is measured. Commonly, these techniques are easy to operate (no safety problems e.g. by radiation), relatively inexpensive, and have a robust construction. The capturing time of the measurements is fast and this yields a good temporal resolution for dynamic processes. Such sensors can operate in aggressive materials, in fast moving fluids, and for multi-phase mixtures. The choice of a specific sensing method is determined by

- the components in the vessel or pipeline (appropriate difference or contrast in the physical properties of the involved material),
- the required spatial resolution and sensitivity,
- the time dynamic of the flow, and
- the environmental conditions (e.g. temperature, pressure).

Electrical tomography is more sensitive to bulk material rather than to phase boundaries. This allows to reconstruct the material properties and to calculate integral parameters, for instance material fractions.

The drawback of electrical tomography is its soft-field modality [91]. This means that the sensing field tends to spread by the material to be imaged and it is related to its electrical properties. This is distinctly different from other tomography techniques, like X-ray computer tomography, where the source lines pass directly through the object. The distortion of the sensing field by the material is inherently non-linear.

Another point is that the set of data is obtained by a limited number of sensors. For instance in electrical capacitance tomography usually eight up to 16 electrodes are used. A higher number of sensors leads to less available surface area of one electrode and thus to a small input signal and to less sensitivity. This small number of measurements complicates the reconstruction of an image. Due to the limited sensitivity, measurement errors have a large influence on the reconstructed image as well. An unique solution can not be guaranteed and the image reconstruction is therefore called an ill-posed problem [87]. For these reasons the reconstructed images have a relatively low spatial resolution. Figures between 5 to 10 percent of the pipe diameter are commonly given for the resolution.

In many applications, however, an accurate determination of phase boundaries is necessary. For example if one is interested in

- the identification of the distribution of mixing zones in stirred reactors,
- interface measurement in complex separation processes,
- comprehensive information about the shape of the slugs' nose and tail in pipeline conveying,
- imaging of the air core in hydro-cyclones for quantitative measurements to obtain information about the operating condition,
- measurements of two or more phase boundaries in pipes with applications to multi-phase flow measurements, and

- non-invasive testing of the quality of materials (inclusions, etc.).

Additionally, the identification of phase sizes and boundaries within vessels and pipelines provides information on fundamental reaction kinetics and it can be used for model validations and for finding an optimal geometry of the equipment. Commonly used imaging techniques yield blurred images with less spatial resolution [54]. Arbitrary criteria are applied in order to establish the boundaries between various materials from such blurred images (e.g. amplitude thresholding techniques for two-phase flow imaging). For quantitative measurements this is not satisfactory. Techniques, which focus especially on the reconstruction of phase boundaries, improve the image significantly [48]. In this work a shape reconstruction method with implicit representation of the boundary is presented for electrical capacitance tomography. This method images the shape, location, size and geometry of different and unknown materials.

In process tomography one is mainly interested in quantities, which are used for controlling the process, i.e. quantities like the volume fractions rather than tomographic images itself. ECT provides an inexpensive method to obtain tomographic images of a process, however resolution is very limited. The application of a single type of sensor is not the only opportunity for a tomography system. A multi-mode system, which employs two or more different sensing principles, improves the image and the information gained from the process to be monitored. They are used to locate or to measure different properties of the involved materials. A possible dual-mode imaging system is to use data of ultrasonic tomography systems and of capacitance tomography. Applications for such systems are for example in imaging of oil/gas/water mixtures in flows or in separators and they can be used to inspect multilayer materials. This work presents a data fusion technique, which incorporates an image from Ultrasound Reflection Tomography (URT) for the shape reconstruction in capacitance tomography. The edge information, which comes from URT, improves the reconstruction of phase boundaries with ECT data significantly.

The next sections in this chapter are organized as follows. In the first two sections, a short overview of the measurement setup and of the inverse problem is given to provide background information on ECT. Next the state of the art of shape reconstruction methods is given. A section with the novelty of this work follows next. The structuring and mathematical notation of this thesis are the last two parts in this chapter.

1.1 Measurement Setup and Forward Problem

At the Institute of Electrical Measurement and Measurement Signal Processing at Graz University of Technology, a capacitance tomography system has been developed in the last years [38, 37, 9, 89]. This system is designed to examine the interior of a PVC pipe by means of evaluating coupling capacitances of a multi-electrode assembly. These capacitances are in a wide range from 1 fF to 5 pF and they pose high demands on the sensor hardware. Figure 1.1 presents the latest developed sensor. 16 electrodes are mounted on the outer area of the pipe and they can operate in different and selectable modes. According to a chosen control pattern, each electrode can either be used as a transmitting or receiving segment. Exploiting the different sensitive areas in the pipe interior, which

Figure 1.1: Prototype of an ECT sensor. 16 electrodes are mounted on the outer surface of a PVC tube and each electrode has an amplifier and output driver.

are caused by the control pattern, the permittivity distribution of the pipe content can be obtained and reconstructed. Figure 1.2 shows the measurement setup of the developed prototype sensor. It is comprising electrodes mounted on the outer pipe surface, the corresponding frontend amplifiers, as well as the signal preprocessing unit. Each frontend is individually controlled by a micro processor and the 16 frontends are connected via a serial bus to the signal preprocessor unit. To allow fast data acquisition a PC is connected to the setup via local area network.

Two hardware concepts with different frontends have been developed and implemented. One principle is designed to determine coupling capacitances by means of measuring electrode potentials (high-impedance measurement) and a second principle is based on the measurement of displacement currents (low-impedance measurement) [3]. They differ with respect to the impedance of the measurement electrodes, which are ideally floating electrodes (high-impedance) or virtual grounded electrodes (low-impedance). Both concepts rely on a carrier frequency system [12] with a frequency of 5.5 MHz and 40 MHz, respectively. For a robust ECT system that is capable of working under harsh environmental conditions, it is essential that the setup is insensitive to stray capacitances. Due to the tuned input bandwidth filter in the low-impedance approach the frontend is insensitive against stray capacitances. This insensitivity allows a proper shielding and makes the sensor immune to different kinds of contamination. Additionally, the circuitry is less affected by electromagnetic compatibility (EMC) influences due to a narrow frequency characteristic. This narrow bandwidth implicates better signal-to-noise ratio compared to the high-impedance approach. A thorough discussion of the advantages of the displacement current measurement can be found in [89]. The imaging results presented in this thesis are based on low-impedance measurements.

A direct method of obtaining the permittivity distribution from such boundary measurements is not available. Instead, starting from a guessed distribution, the field problem is solved iteratively in an appropriate computer model. Then the initial guess is improved

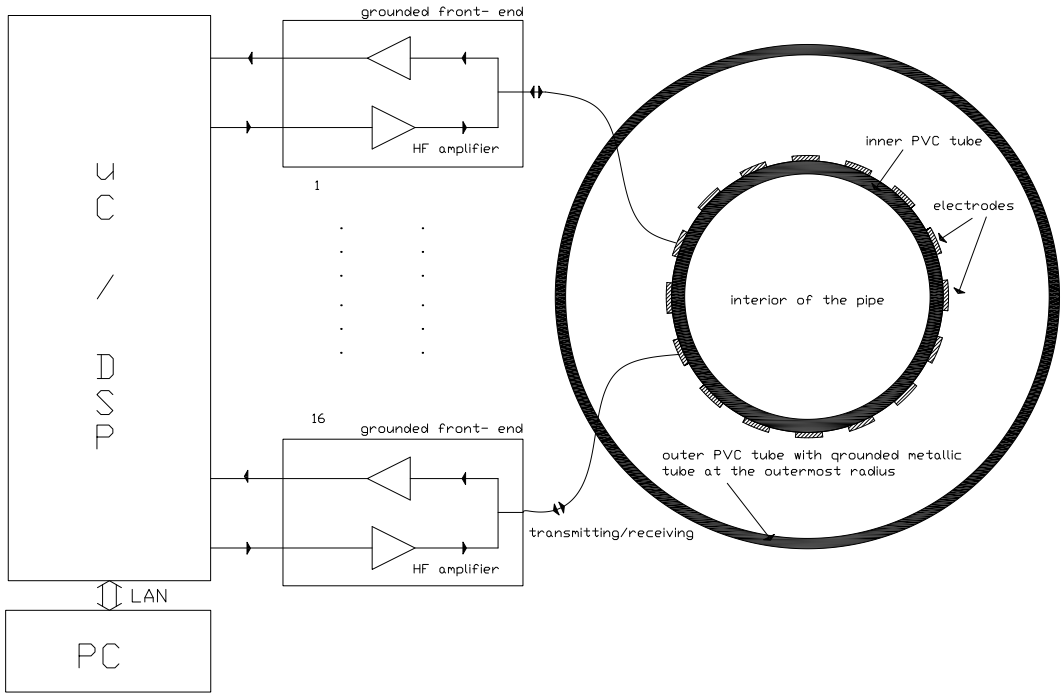

Figure 1.2: ECT measurement setup with 16 electrodes, sensor frontends, and preprocessing unit.

by minimizing the error between the calculated and measured boundary data. Thus a computer model, which corresponds to the measurement setup, is an essential part for the imaging process. Some simplifications are used to obtain a suitable model. First the wave length of the applied excitation frequency (40 MHz) is larger than the dimension of the sensor[1] (about 15 cm). Thus an electrostatic approximation of the field problem is feasible. Further it is assumed that only the imaginary part of the current is measured. The sensor frontend, however, measures the absolute value including a real part coming from a conductive material. In this case an erroneous permittivity value is imaged and a careful interpretation of the material value is important. Edge effects in longitudinal direction are neglected because the ratio of the length of the electrodes (5 centimeters) to the diameter of the pipe (10.3 centimeters) is large enough. Additionally, it is assumed that the material to be imaged does not vary in longitudinal direction for the length of the electrodes. Thus a 2-dimensional model of the whole domain of interest can be employed. On the right hand side in figure 1.2 the cross-section of the ECT sensor is shown. The field problem can be solved for certain permittivity distributions and boundary conditions e.g. with the Finite Element Method (FEM) or Boundary Element Method (BEM). This problem is called the forward problem.

[1]This comparison depends on the material inside the sensor. However, it holds true for the involved materials like air, oil, and tap water.

1.2 Definition of the Inverse Problem

The imaging process itself is considered as an inverse problem to find the spatial distributed permittivities for a given set of boundary measurements. This is performed iteratively by an optimization problem with a fit to data functional. In this section it is assumed that displacement currents are measured. It can be adapted easily to measurements of voltages (frontends with high impedance).

Let ε denote the permittivity value of a medium, u the electric scalar potential[2], u_0 a Dirichlet boundary condition on the exciting electrodes with the boundary Γ_0, and the measurement electrodes with the boundary Γ_e, then the forward problem is described by

$$\boxed{\begin{aligned} \nabla \cdot (\varepsilon \nabla u) &= 0 \\ u|_{\Gamma_0} &= u_0 \\ u|_{\Gamma_e} &= 0. \end{aligned}} \tag{1.1}$$

The charges on the electrodes correspond to measured displacement currents. The charge is calculated e.g. by the flux integrating method for the ith electrode

$$q_i = \int_{\Gamma_{e,i}} \varepsilon \frac{\partial u}{\partial n} \, \mathrm{d}s \tag{1.2}$$

with $\Gamma_{e,i}$ the electrode surface and $\vec{n}$ the inward normal vector. The calculated and the measured charges for different electrodes and different measurement patterns are summarized into $\vec{q}(\varepsilon) \in \mathbb{R}^{n_i}$ and $\vec{q}_m \in \mathbb{R}^{n_i}$ respectively (n_i is the number of all charges).

In [65] it is shown that an assumption of additive and Gaussian distributed measurement noise (noise vector $\vec{m}$) with zero mean is valid. The noise is defined to be independent from the material distribution. The probability density function reads

$$\pi_{noise}(\vec{m}) \sim \exp\left(-\frac{1}{2}\vec{m}^T \mathbf{C}^{-1} \vec{m}\right) \tag{1.3}$$

with $\mathbf{C} \in \mathbb{R}^{n_i \times n_i}$ a symmetric and positive definite covariance matrix of the noise. In the experimental measurement system an approximation for the noise covariance can be obtained by using a set of repeated measurements or by analyzing the measurement system. Next a prior probability density π_{pr} is defined which is assumed to be independent to the measurement noise n. The so called regularizing prior density is written in the form

$$\pi_{pr}(\varepsilon) \sim \exp(-\alpha^2 R(\varepsilon)) \tag{1.4}$$

where α^2 is a scaling parameter that is related to the confidence on the regularizing prior and $R(\varepsilon)$ is the regularization functional. Then the conditional probability density

[2]The electric scalar potential is linked to the electric field strength by $\vec{E} = -\nabla u$.

$\pi_{post}(\varepsilon) = \pi(\varepsilon|\vec{q}_m)$ is calculated by the well known Bayes formula. The density has the following structure

$$\pi(\varepsilon|\vec{q}_m) \sim \pi_{noise}(\vec{q}(\varepsilon) - \vec{q}_m)\pi_{pr}(\varepsilon). \tag{1.5}$$

and it is called the solution of the inverse problem in a statistical sense. The estimation of the whole a posteriori distribution is too computational expensive. Additionally, it is impossible to visualize the distribution directly. Commonly, the maximum a posteriori (MAP) estimate is used as reconstructed permittivity distribution

$$\varepsilon_{MAP} = \arg\max_{\varepsilon} \pi(\varepsilon|\vec{q}_m). \tag{1.6}$$

It is the most probable configuration of the model for the given outcome of the experiment, the prior information, and the physical laws that are applied to the system. The particular assumptions in this section lead to an optimization problem with weighted least squares structure and Tikhonov regularization (see e.g. [87])

$$\varepsilon = \arg\min_{\varepsilon} \left[\frac{1}{2} (\vec{q}(\varepsilon) - \vec{q}_m)^T \mathbf{C}^{-1} (\vec{q}(\varepsilon) - \vec{q}_m) + \alpha^2 R(\varepsilon) \right]. \tag{1.7}$$

The covariance matrix $\mathbf{C}$ incorporates a weight on the different measurements. The parameter α^2 is the regularization parameter and $R(\varepsilon)$ the regularization functional. With the technique of regularization one can cope with instabilities due to the strong influence of the noise on the solution (e.g. [28, 87]) and the term can ensure an unique solution. If a prior information is available (like an image form URT or prior information on the permittivity values) one can incorporate this information by the regularization term. Other possibilities are to use ad hoc terms like a smoothness assumption on the solution [8] or an assumption of small total variation [6].

For a shape imaging method the material distribution is a piecewise constant function. Figure 1.3 sketches the cross-section of the sensor and an example illustrates an unknown shape. The two different regions have the permittivities ε_1 and ε_2 respectively. The interface where the jump of material value occurs is denoted by Γ. For all unknown regions (more than two are allowed) the material values are summarized into $\vec{\varepsilon}$. Then the cost functional in (1.7) is written as follows

$$\boxed{I(\vec{\varepsilon}, \Gamma) = \frac{1}{2} \left\| \mathbf{W} \left(\vec{q}(\vec{\varepsilon}, \Gamma) - \vec{q}_m \right) \right\|^2 + \alpha^2 R(\vec{\varepsilon}, \Gamma),} \tag{1.8}$$

with $\mathbf{W}^T\mathbf{W} = \mathbf{C}^{-1}$. This function depends on the piecewise constant permittivity values and on the boundary of the shapes.

Numerical optimization tools provide a stable and fast way to solve (1.7). For instance the Gauss-Newton algorithm [29] is a deterministic approach to solve the optimization problem of least squares structure. For this a Jacobian matrix is necessary, which describes the influence of change of material values and geometry on the calculated charges.

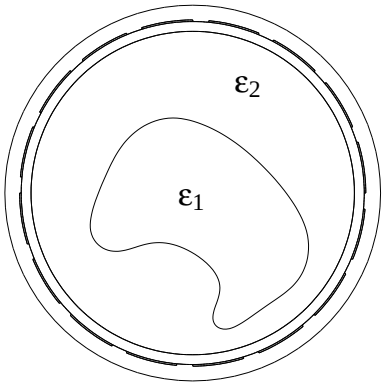

Figure 1.3: Sketch of the sensor model with piecewise constant permittivities.

Hence an analytical calculation of the so called material and shape derivative [75] is necessary. These derivatives can be obtained easily by the adjoint variable approach. The advantage of a deterministic approach with information about the gradient is for instance the fast convergence rate. Especially if one is interested in on-line process monitoring, a fast rate of reconstructed images is desired.

1.3 State of the Art

The underlying field problem in ECT is described by the Laplace equation. Similar field problems arise e.g. in ERT and Electrical Impedance Tomography (EIT). Partial Differential Equations (PDE) occur also if one solves inverse scattering problems (acoustic or electromagnetic waves). Many of the techniques, which are applied to solve these different inverse problems, resemble each other. Therefore, this section of the state of the art makes no further distinction between them. Table 1.1 summarizes some criteria to classify the numerous publications. These publications are presented next and they are ordered in the following paragraphs. First different approaches to overcome the blurring of images, which are based on a fixed discretization, are presented. The second paragraph is about shape reconstruction methods, which rely on the FEM. Next inverse problems are presented, which are solved by the level set method. Then shape reconstruction methods with the boundary element method are discussed. The last paragraph deals with the fusion of different sensor data.

Electrical Tomography on a Fixed Grid. The finite element method does not match the needs of a shape reconstruction perfectly. The unknown interface is not treated naturally and the finite elements incorporate an upper limit for the spatial resolution. However many toolboxes and algorithms based on the FEM already exist. For instance Brandstätter *et al.* [8] present a reconstruction algorithm based on a fixed grid. The permittivity value of each finite element in the pipe, in which the material is to be resolved spatially, is treated as unknown. Sharp discontinuities are not reconstructed due to a smoothness assumption as regularization term. To overcome the blurring of the image, Borsic [6]

Solver for the forward problem.	Inverse problems, coming from optimal design, shape optimization, and identification of distributed parameters in PDE, are closely related to this work. Numerous publications deal with these problems and they propose many different solvers for the forward problem, like FEM or BEM.
Description of the boundary.	For the description of the boundary different parameterizations or other types like implicit representations of the interface are utilized. This has an important influence on the flexibility and on the necessary a priori information about the number of unknown regions.
Regularization method.	A regularization method is mandatory to overcome the ill-posed nature of the inverse problem. Different approaches are suggested, like total variational regularization and the Mumford-Shah functional.
Parameter space.	The parameter space has an influence on the convergence behavior of the inverse problem. Only a few papers assume unknown material values and perform the reconstruction of shape and material simultaneously.
Optimization technique.	The imaging process can be based on a deterministic approach where a descent direction is calculated by direct differentiation or by an adjoint variable approach. Other optimization techniques are for example genetic algorithms.
Validation.	A validation of the proposed techniques can be obtained e.g. by simulated experiments. Few papers apply real measurement data for the reconstruction.

Table 1.1: Different aspects of shape optimization problems in literature.

proposes a regularization term, which penalizes the total variation of the image (total variation regularization). Thus the sharpness of the interface is improved. Experimental results for this regularization term are presented in [79]. A finer mesh to improve the spatial resolution leads to an increase in the computational effort for the forward problem and for the inversion of the fully occupied Hessian matrix in the Gauss-Newton approach.

For two-phase flows one idea is mesh grouping (e.g. [45, 47]). This technique can overcome the increase of the computational burden and the poor convergence characteristics in the Gauss-Newton (Newton-Raphson respectively) algorithm as the finite elements increase. The material values are classified iteratively in different groups. Another idea is the monotonicity method [83], which provides a non-iterative inversion technique with low computational costs. Mesh grouping and the monotonicity method are restricted to two components mixtures. Additionally, only a partial classification of the pixels to one

of the material is obtained. Rondi and Santosa [66] introduce the Mumford-Shah functional as regularization term for the linearized problem in EIT. An image segmentation is performed in the same time as the reconstruction. Simulated experiments are promising, however, the method requires tuning of several parameters.

FEM and Shape Reconstruction. Kolehmainen *et al.* [48] present a shape reconstruction method, which assumes known material values. The paper introduces a general framework for elliptic problems with a parameterization of the interface by Fourier coefficients. To overcome the fixed discretization in finite elements a subdivision of the elements is performed. The descent direction is calculated by the Levenberg-Marquardt method and an example in optical tomography with synthetic data is given. It is reported that the method has the tendency to produce self-intersecting boundaries if the starting condition is far away from the true contour. For EIT, estimations of phase boundaries are performed in [46], where the boundary is described by interpolation of front points, and [43], where truncated Fourier coefficients are used. Simulated data is used to verify the algorithms. Difficulties are the unknown number of regions and that knowledge of the material properties of the involved phases must be available. Another estimation of boundaries based on the FEM is described in [85] where a Bezier curve approach is used. The boundary to a non-conductive phase is reconstructed as well as the material distribution of the outer phase. In this paper simulations and real world data are used to verify the method.

Level Set Method and Inverse Problems. To overcome the limitations of a parameterization of the curve a level set method can be used. With this method the shape can evolve iteratively and any arbitrary topology can occur (merging and splitting of regions is handled easily). In the early paper [68] from Santosa a level set approach is used for the linear inverse problems in deconvolution and for diffraction screen reconstruction in optic and acoustic. It assumes known material values and suggests an optimization approach as alternative to a shape evolution approach. In [55] Litman *et al.* solve an inverse scattering problem with the level set method and the method of moments. The movement of the shape is performed by a velocity field to minimize the residual in the data fit and the gradient is calculated analytically by the adjoint variable method. Another inverse scattering problem is discussed in [24] and numerical examples are shown based on the finite element method. Ito *et al.* [42] propose an immersed interface method (a version of finite difference method). The problem in [42] and Ito [41] is motivated by electrical tomography. The gradient direction of the boundary is calculated for known conductivities. Deng *et al.* present in [22] a fast immersed interface method in 3D for interface problems of piecewise constant coefficients. They successfully solve an inverse problem of shape identification. Burger [14] describes a framework for shape optimization and reconstruction of elliptic boundary value problems. This is based on a gradient flow and on a FEM discretization. In [15] the descent direction is calculated by the Levenberg-Marquardt method and in [16] the shape optimization approach is extended by topological derivatives. The idea of topological derivatives calculates the sensitivity of the objective function with respect to a hole in the material and the reconstruction of the correct topol-

ogy is improved.

Chan and Tai [17, 18] present a level set method, which reconstructs the material value simultaneously to the shape. This method solves the inverse problem of recovering discontinuous coefficients from boundary measurements in elliptic problems. A variational augmented Lagrangian formulation is proposed instead of the commonly used speed (velocity) method. Additionally, Chan and Tai propose a multiple level set framework to describe more than two phases. After 100 to 1000 iterations the shape and material value can be reconstructed successfully. This method uses total variational regularization. This regularization term is used as well by Chung *et al.* in [20]. The optimization problem for EIT is solved by the gradient descent. Simulated data with simulated noise validates this method. In [2] a shape sensitivity analysis and level set method for elliptic problems are presented, where a singular surface with known coefficients in each region is reconstructed. Numerical simulations are performed by the FEM. In [77] experimental results are presented for ECT with a level set based algorithm. The level set approach reconstructs the images on a fixed discretization into finite elements. However, less information is given about the material values (assumed to be known a priori, constant during the reconstruction, etc.). The possibility to reconstruct more than two phases is not discussed.

Shape Reconstruction with the Boundary Element Method. A natural way to solve the forward problem with piecewise constant material values is to use the boundary element method. The variable contour is discretized easily in each iteration step. In the early paper [5] Bonnet solves a geometrical inverse problem for linearly acoustic and elastic medium by boundary integral equations. The boundary is described by parameters or by the movement of mesh nodes in two and three dimensions. A quasi-Newton method is proposed to solve the optimization and the material derivative concept is applied to the formulation of an inverse obstacle problem. In [25, 26] Legendre polynomials are used for EIT in two and three dimensions. The method reconstructs the shape of internal regions with zero conductivity. The number of known regions has to be available a priori. The optimization is performed by downhill simplex, Powell, and conjugate gradient (the Jacobian for the conjugate gradient method is calculated by finite differences). No analytically derived Jacobian calculation is performed and thus up to 2000 evaluations of the forward problem are necessary. In [40] a hybrid Powell and genetic algorithm is proposed. As before Legendre polynomials are used and no gradient computation is necessary. Two and three dimensional results are shown on basis of simulated data. In [62] a front tracking, which adjusts the nodes of the boundary elements, is suggested for EIT-monitored cryosurgery. Simulated phantom images are used to reconstruct the sharp discontinuity in the physical properties across the interface. The Jacobian is calculated by direct differentiation of the BEM system matrices.

Sensor Fusion. Multisensor data fusion is successfully applied in different disciplines of engineering. They are applied to problems where single sensors are only capable of yielding incomplete or inaccurate information. Multisensor fusion techniques are already implemented with other tomographic imaging principles than ECT and URT. In [7], the

inspection of sandwiched structures is performed by Computed Tomography (CT), laser range measurements, and ultrasound thickness measurements. The range and thickness data are used to impose geometrical constraints on the linear equation system for the reconstruction. These constraints reduce the degree of freedom of the CT problem, which leads to an improved reconstruction result. Two different tomographic principles are fused by Zhao in [93]. Diffuse Optical Tomography (DOT) is structurally guided by ultrasound tomography. The results from ultrasound tomography are used as a rough estimate of the location of phase boundaries. The finite element mesh, used for DOT, is then locally refined in regions with potential phase transitions. As a result, the spatial resolution of the imaging system is considerably improved. The design of an integrated multi-modal process tomography system is described by Hoyle [39]. System engineering is used for the hardware and software design. An algorithm based on a different multi-modal data is proposed in [78]. It is assumed that one point of the boundary is determined from ultrasonic time of flight data. Then a reconstruction is performed by the level set method on a finite element discretization with simulated ERT data.

1.4 Novelty and Publications

In this thesis an image reconstruction technique is presented, which is based on a boundary element method to solve the forward problem and on a level set formulation for the description of object boundaries. As discussed, the utilization of the boundary element method is very natural for a shape reconstruction algorithm and it is of advantage compared with e.g. a finite element approach. As far as the author knows it is the first treatment of the inverse problem in ECT by the combination of boundary elements and the level set method. With this formulation the topology of a disturbance can change easily and any arbitrary shape can occur in the iterative reconstruction. The technique presented in this work features

- reconstruction of multiple phase flows where the number of phases is not available a priori,
- non-trivial geometries are allowed due to the implemented level set method,
- reconstruction of the unknown material values for each region simultaneous to the shape,
- treatment of the field problem with boundary elements instead of a finite element method to allow higher spatial resolution,
- fast convergence because a Gauss-Newton approach is implemented to calculate the descent direction of the cost functional and because a line search algorithm is implemented,
- physical constraints for the material values and for the geometry are incorporated by an active set method, which is important for a stable reconstruction with real world data,

- measurement noise is considered as well and improves the image quality significantly, and

- real world measurement data validates the algorithm and illustrates the good performance of this method.

In this thesis a Gaussian measurement noise is considered and the object to be recovered is assumed to be stationary for one measurement cycle. A survey of this reconstruction technique is also published in [49, 51] where the reconstruction is performed by Dirichlet boundary data and examples based on real world data are presented. In these publications a coupled FEM-BEM is utilized in contrary to this work where only a BEM approach is discussed because the recently developed prototype has a simplified sensor design. The paper [50] gives a detailed discussion of the influence of different types of boundary data on the imaging process. It is shown that both types of data, corresponding to the developed high and low impedance frontends, deliver images of equal quality if a similar signal to noise ratio is assumed. Reconstruction results, which have been submitted recently to the journal of Measurement Science and Technology (see [52]), are shown in figure 1.4. Two PVC objects are located in the interior of the sensor. First the reconstruction is performed by a standard imaging technique based on a fixed finite element mesh. The second image is obtained by the new developed shape reconstruction technique. It illustrates the gain in spatial resolution by the shape reconstruction method.

For the regularization term prior information can be incorporated into the ECT imaging process. A sensor fusion technique of URT and ECT data is presented in [82] for the finite element method. A novel regularization term for a level set based reconstruction is presented in [11, 10]. An edge detection of an URT image simultaneously to the ECT reconstruction combines information about edges from URT with ECT data, which is more sensitive to bulk material. This leads to an increased accuracy of the estimated object boundaries and material values. The results in these papers are based on simulation because the combined sensor hardware, ECT and URT, is currently under development.

Further publications are [30, 31] where ECT results with experimental data are presented to detect tracer particles in phase flow measurements. In [89] the new hardware concept, which is based on the measurement of displacement current, is presented.

1.5 Structuring of this Work

In chapter 2 the description of object boundaries is considered. It starts with a short overview over possible implicit and explicit representations and it gives the motivation to use the level set framework. Additionally, this chapter explains briefly the deformation of objects and the concept of shape derivatives is introduced.

In the next chapter these derivatives are applied to the forward problem to calculate the sensitivity of the electrode potential or charge with respect to a deformation of the contour and with respect to the material values. This chapter deals with the first term (least squares) in the cost functional (1.8). Therefore the adjoint variable method is utilized for the two dimensional ECT model. A proof for the sensitivity equations and the

(a) Measurement setup: two PVC objects.

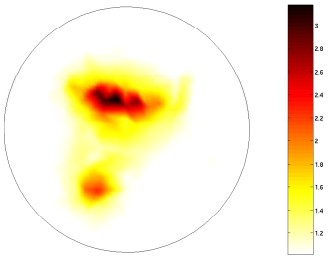

(b) Reconstruction with a FEM based algorithm.

(c) Reconstruction with BEM and level set algorithm.

Figure 1.4: Performance of the shape reconstruction method. This example is based on real world measurements and illustrates the gain in the spatial resolution by a shape reconstruction method. With the BEM and level set based algorithm, the contours are reconstructed within small tolerances compared to the true objects.

corresponding adjoint problems is given. Additionally, this chapter describes the implementation of the boundary element method.

Chapter 4 deals with appropriate regularization terms (second term in (1.8)). Ad hoc approaches are discussed as well as a regularization technique where a priori information is available from ultrasonic reflection tomography. The calculation of a Newton-type speed function is discussed for the proposed regularization terms.

The last chapter demonstrates the performance of the algorithm with experimental results. A discussion concludes the main features and opportunities of the proposed shape imaging technique.

In appendix A one can find an introduction on shape derivatives for PDE. An one-dimensional example of a plate capacitor is presented. First the shape differentiation is performed by direct differentiation of an analytical solution. Additionally, it is carried out by the adjoint variable method and both methods are compared. Appendix B gives details about the discretization of the gradient and the Hessian matrix of the regularization term.

1.6 Mathematical Notation

A comprehensive list of symbols and variables can be found on page 93. The notation of shape and material derivatives, as defined in [76], are introduced in chapter 2. Tangential derivatives are used as well and they are defined in corresponding context. This work is an application of different mathematical methods. Especially the correct function spaces, theoretical foundations, and proofs are neglected and the interested reader can find comprehensive information in the referred literature.

Chapter 2

Description and Deformation of Objects

In image processing (e.g. image segmentation) and computer vision one task is often to recover the shape of objects in two and three dimensions. Many of the existing shape modeling schemes require that the topology of the object is known before the recovery can commence [25, 26, 43]. In the case of industrial tomography it is difficult to specify the number of unknown objects a priori and an assumption is a significant limitation of the reconstruction algorithm. In the case of ECT, the regions are distinguished by their permittivity values. The contour is described by the boundaries between distinct regions. In the iterative reconstruction process this contour is deformed and the ability to describe this movement is another important aspect of shape models. Additionally, the models have different attributes concerning the calculation of differential quantities such as normals and curvature.

First a short description of several methods is given and the motivation to use the level set method is discussed. A comprehensive discussion of different deformable contours is given e.g. in [80, 57]. First, shape models can be classified in discrete and continuous ones. A discrete representation of a shape is a set of points or the discrete mesh of boundary elements. Contrary to these discrete representations a continuous one offers the ability to compute differential quantities almost everywhere. For this reason the second approach is discussed further and two possible representations are suggested.

First a contour can be represented explicitly by parameterization of the boundary trace. A two dimensional parametric contour is described by a vector-valued function $C(s,t) \in \mathbb{R}^2$ where s is usually the arc length and t the time. The movement and deformation is achieved by temporal and spatial discretization e.g. with finite differences. Possible parameterizations are Legendre polynomials and Fourier coefficients. Another representation proposed in literature is for example B-splines [4, 84]. These models present the contour by as few parameters as possible while still meeting the requirements of the given application. This formulation, however, has several drawbacks. When tracking the motion of the interface, problems arise if different parts of the front cross each other. Additionally, difficulties arise if the shape tries to break into pieces or if two shapes try to merge into one. The main drawback of this explicit approach is that the evolving model is not capable to undergo topological changes. Additional procedures must be added to detect and deal with these situations and this is usually a cumbersome task.

The opposition is the implicit representation. The contour is described by the zero level set of a higher dimensional function. The deformation of the contour in time is linked to the evolution of this function and its discretization constrains the resolution of the contour. The contour is usually closed and an open boundary is only possible on the border of the underlying grid of the higher dimensional function. The main advantage of this formulation is its ability to automatically change the topology during the deformation. In contrast to a parametric contour the implementation of the implicit approach requires a little more care. The level set method, which has been utilized in this work, belongs to this group of shape representations.

In the following sections an overview of the implemented level set method is given. Next the definition of shape derivatives is presented to differentiate boundary and domain integrals with respect to a deformation of the contour. These definitions are applied in chapter 3 and additionally they are necessary later in chapter 4 to calculate the shape derivatives of possible regularization terms.

2.1 Level Set Framework

The main advantage of the level set method is, as explained, its ability to undergo a topological transformation. This formulation can elegantly describe shapes, which split and merge freely. The method was originally introduced by Osher and Sethian in [61] and is now widely used in lots of applications (for instance the simulation of two-phase oil-water flows in pipes [74]) and a lot of literature can be found e.g. [72, 73, 60, 59, 58, 88, 90]. Some additional attributes of the level set method are given below.

1. The formulation remains unchanged for different dimensions. Surfaces in 3D can be represented as well as contours in 2D.

2. Geometry properties of the front, like the normal and the curvature, are easily determined by differentiation of the level set function.

3. It is not necessary to have a priori information about the number of unknown phases in the flow and their topology. The topology of the initial condition is not necessarily the same as the one at convergence.

The idea of this method is to define a smooth function $\Phi : D \times \mathbb{R}^+ \to \mathbb{R}$ in the domain $D \subset \mathbb{R}^2$ that represents the interface as the set where

$$\Phi(\vec{x},t) = 0. \tag{2.1}$$

The domain D is divided by the interface in distinct regions such that following conditions hold.

$$\begin{aligned} \Omega_1 &= \{\vec{x} \in D : \Phi(\vec{x},t) < 0\} && (2.2)\\ \Omega_2 &= D \backslash \overline{\Omega}_1 = \{\vec{x} \in D : \Phi(\vec{x},t) > 0\} && (2.3)\\ \Gamma &= \partial\Omega_1 = \{\vec{x} \in D : \Phi(\vec{x},t) = 0\} && (2.4) \end{aligned}$$

The trajectory of a particle $\vec{x}(t)$ on the interface is defined by the movement $\frac{\mathrm{d}}{\mathrm{d}t}\vec{x}(t) = \vec{V}_F$. The deformation of the whole domain is described by this velocity field $\vec{V}_F : D \to \mathbb{R}^2$. Commonly this field depends on position, time, geometry, or some external physics. Partial differentiation of (2.1) leads to

$$\frac{\partial \Phi}{\partial t} + \nabla\Phi \cdot \vec{V}_F = 0. \tag{2.5}$$

This partial differential equation is of type Hamilton-Jacobi, which is also known as transport equation. Actually, only the projection of the velocity on the normal, denoted by $\tilde{F} : D \to \mathbb{R}$, is necessary and (2.5) becomes

$$\boxed{\frac{\partial \Phi}{\partial t} + |\nabla\Phi|\tilde{F} = 0} \tag{2.6}$$

The last equation is solved by spatial discretization on a fixed grid. The resulting ordinary differential equation is solved by an appropriate time stepping method. The CFL (Courant, Friedrichs, and Lewy) condition [59] $\Delta t|\tilde{F}| < \Delta x$ must hold if one is interested in the correct and stable evolution of the interface. In this work, however, an optimization is performed and a fast convergence is more important than the evolution of the interface itself. This means that it is not important to track a very smooth propagation of the interface. A line search algorithm is used to determine an optimal step size and to relax the CFL condition. A simple forward Euler step is applied for time discretization. To speed up the calculation of the level set function one idea is to localize Φ to a small tube (e.g. [63]) about the contour $\Gamma(t)$. This is appropriate for small time steps, which is usually the case if the CFL condition holds. As mentioned above in this work the step size is as large as possible and thus a localization is an unnecessary restriction on the step size.

As already mentioned geometric properties have simple representations in terms of Φ, like the outward normal of region Ω_1

$$\vec{n}_1 = \frac{\nabla\Phi}{|\nabla\Phi|} \tag{2.7}$$

and the curvature

$$\kappa = \nabla \cdot \frac{\nabla\Phi}{|\nabla\Phi|}. \tag{2.8}$$

The velocity $\tilde{F}$ is chosen as descent direction of the cost-functional (1.8). Therefore a velocity $F : \Gamma(t) \to \mathbb{R}$ is calculated for points on the contour. At this point three issues of practical importance arise.

Velocity Extension. First, the calculated velocity must be extended off the interface to the whole domain of Φ to solve (2.6). This process is called velocity extension and is commonly not trivial. One idea to perform this is based on the solution of an additional partial differential equation. A detailed discussion is given in subsection 2.1.1.

Reinitialization. Second, it is of importance that the level set function remains well behaved. That implies bounds on the gradient such as

$$0 < c_1 \leq |\nabla\Phi| \leq c_2 \tag{2.9}$$

for some constants c_1 and c_2. Commonly the level set function is supposed to be a signed distance function, i.e.

$$|\nabla\Phi| = 1. \tag{2.10}$$

Figure 2.1 illustrates a slice of the level set function. The interface is well defined due to (2.10). Additionally, the numerical approximations of (2.7) and (2.8) are stable. With this definition the distance of an arbitrary point $\vec{x}$ to the surface Γ is equal to the function value $|\Phi(\vec{x},t)|$. Even if accurate numerical schemes are applied to solve (2.6), the level set function often becomes very flat or steep at the interface Γ. For that reason a correction is necessary to satisfy (2.10). This procedure is called reinitialization and it is discussed in subsection 2.1.2. For both procedures, velocity extension and reinitialization, ideas coming from [63] are used and presented briefly. Alternatively one can use a fast marching algorithm [1, 73] to determine the extension velocity and the signed distance function. The PDE based approach, however, leads to a flexible and accurate method and it is easy to implement.

The spatial discretization of Φ is determined by the necessary accuracy of the contour. It is chosen fine enough to ensure the accuracy of the contour. A course grid, however, performs faster. Additionally first order finite differences are used to get a moderate computational burden.

Multiphase level set method. Another question arises if one assumes more than two unknown phases in the pipe. An extension of the level set framework is introduced in [86], namely the multiphase level set method. In other publications the method is called multiple level set method (e.g. [18]). This method is implemented in this work and the corresponding idea is presented in subsection 2.1.3.

2.1.1 Velocity Extension

One way to extend the velocity off the front is to let $\tilde{F}$ be constant along the curve normal to $\Gamma(t)$. This condition ensures that Φ keeps being a signed distance function. In other words let

$$\vec{n} \cdot \nabla\tilde{F} = 0. \tag{2.11}$$

This suggests the following partial differential equation

$$\frac{\partial}{\partial\tau}\tilde{F} + S(\Phi)\frac{\nabla\Phi}{|\nabla\Phi|} \cdot \nabla\tilde{F} = 0, \tag{2.12}$$

where $S(\Phi)$ is the signature defined as

$$S(\Phi) = \begin{cases} -1 & \text{if } \Phi < 0, \\ 0 & \text{if } \Phi = 0, \\ 1 & \text{if } \Phi > 0. \end{cases} \tag{2.13}$$

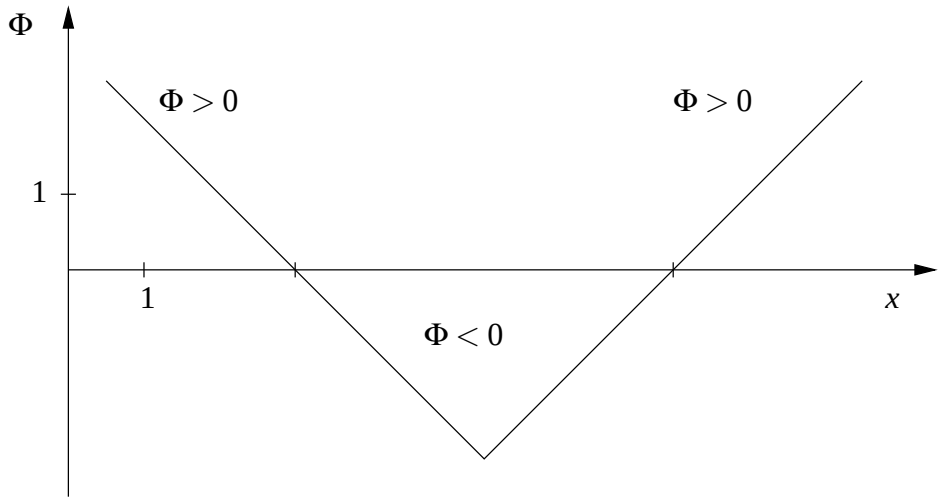

Figure 2.1: Slice of the level set function. The interface is described by $\Phi = 0$. The absolute value of the gradient equals one to ensure a numerical accurate calculation.

This problem is solved by applying the initial condition $\tilde{F}|_{\Gamma(t)} = F$ until a steady state is achieved. A highly accurate numerical scheme is presented in [44]. In this work following first order scheme coupled with a forward Euler discretization is utilized. An important characteristics of (2.12) is that information flows out of the interface. This is an essential attribute, which must be enforced numerically to ensure stability. The method is called upward scheme since only values biased to Γ are used to approximate $\nabla\tilde{F}$ numerically. $S(\Phi)\frac{\nabla\Phi}{|\nabla\Phi|}$ is constant for the iterative algorithm. The signature is smeared for numerical reasons by

$$S_\sigma(\Phi) = \frac{\Phi}{\sqrt{\Phi^2 + \sigma^2}}, \tag{2.14}$$

where σ is a smoothing parameter in the size of the spatial discretization Δx. The normal vector is denoted by

$$(n_x \;\; n_y)^T = \frac{\nabla\Phi}{|\nabla\Phi|} \tag{2.15}$$

and is calculated by central finite differences. The nodal values of a 2D grid with uniform spacing Δx in x-direction and in y-direction are denoted by the indices i and j. The first coordinate of $\nabla\tilde{F}$ is calculated by forward finite differences by

$$D_x^+\tilde{F}_{ij} = \frac{\tilde{F}_{i+1,j} - \tilde{F}_{ij}}{\Delta x} \tag{2.16}$$

and by backward finite differences by

$$D_x^-\tilde{F}_{ij} = \frac{\tilde{F}_{ij} - \tilde{F}_{i-1,j}}{\Delta x}. \tag{2.17}$$

The same notation is used for the second coordinate. The usage of forward and backward finite differences depends on the sign of the corresponding component of the normal vector (direction) and on the sign of the level set function (inner/outer region). This is illustrated in figure 2.2 for the x-direction. Forward differences are chosen if the product

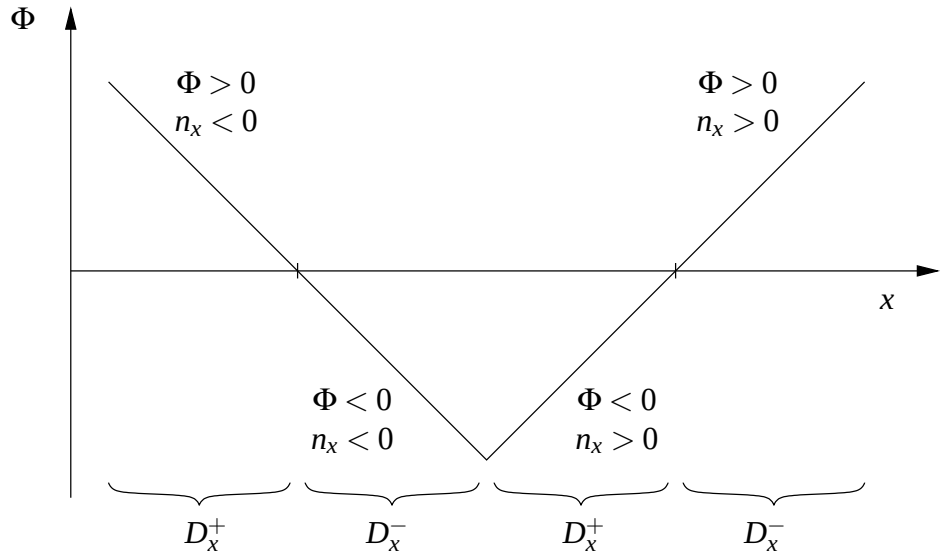

Figure 2.2: The choice between forward and backward finite differences for an upward scheme depends on the sign of normal vector and level set function.

$S(\Phi)n_x$ is negative and, respectively, backward differences are chosen for a positive product. The numerical scheme to solve (2.12) reads as follows (indices i and j are neglected, the iteration step is indicated by k)

$$\tilde{F}^{k+1} = \tilde{F}^k - \Delta\tau \Big\{ (S_\sigma n_x)^+ D_x^- \tilde{F}^k + (S_\sigma n_x)^- D_x^+ \tilde{F}^k + (S_\sigma n_y)^+ D_y^- \tilde{F}^k + (S_\sigma n_y)^- D_y^+ \tilde{F}^k \Big\} \tag{2.18}$$

where $(\cdot)^+ = \max(\cdot, 0)$ and $(\cdot)^- = \min(\cdot, 0)$. For this scheme the CFL condition must hold. The process, however, converges quickly near the interface Γ because information is only transported away from the interface.

2.1.2 Reinitialization

Reinitialization is necessary because flat or steep regions, which are caused by numerical inaccuracies, complicate the determination of the contour. Additionally, the computation of the normal and curvature becomes inaccurate. For these numerical reasons the level set function is corrected to ensure that it remains a signed distance function and that it remains well behaved.

This is simply done by replacing Φ by another function that has the same zero level set but behaves better. Among other methods to perform this, one elegant way is based on following partial differential equation

$$\frac{\partial}{\partial\tau}\Phi + S(\Phi)(|\nabla\Phi| - 1) = 0, \tag{2.19}$$

which is solved until a steady state is achieved. Similar to the velocity extension a first order upwind scheme for the spatial and a forward Euler time discretization is used (indices

i and j neglected, the iteration step is indicated by k)

$$\begin{aligned}\Phi^{k+1} = \Phi^k &- \Delta\tau S^+(\sqrt{\max[(a^+)^2,(b^-)^2]+\min[(c^+)^2,(d^-)^2]}-1)\\ &- \Delta\tau S^-(\sqrt{\max[(a^-)^2,(b^+)^2]+\min[(c^-)^2,(d^+)^2]}-1).\end{aligned} \tag{2.20}$$

$(\cdot)^+ = \max(\cdot,0)$ and $(\cdot)^- = \min(\cdot,0)$ and following abbreviations are used for the finite differences

$$a = D_x^- \Phi_{ij}^k \tag{2.21}$$
$$b = D_x^+ \Phi_{ij}^k \tag{2.22}$$
$$c = D_y^- \Phi_{ij}^k \tag{2.23}$$
$$d = D_y^+ \Phi_{ij}^k. \tag{2.24}$$

This method has a good convergence as discussed in [63]. The reinitialization step is performed in every iteration because the interface changes rapidly. This is the case because the step size for (2.6) is chosen as far as possible by a line search algorithm.

2.1.3 Multiphase Level Set Method

For image segmentation of more than two phases Vese and Chan introduce in [86] a multiphase level set framework. In this paper it is shown that complex topologies can be represented. The idea is to describe n_l phases by $n_p = \log_2 n_l$ level set functions. For instance, with two level set functions Φ_1 and Φ_2 it is possible to express four regions of constant values ε_l by

$$\begin{aligned}\varepsilon =&\varepsilon_0 H(\Phi_1)H(\Phi_2) + \varepsilon_1 H(-\Phi_1)H(\Phi_2)\\ &+\varepsilon_2 H(\Phi_1)H(-\Phi_2) + \varepsilon_3 H(-\Phi_1)H(-\Phi_2),\end{aligned} \tag{2.25}$$

where $H(\Phi)$ is the Heaviside function defined as follows.

$$H(\Phi) = \begin{cases} 1 & \text{if } \Phi > 0, \\ 0 & \text{if } \Phi \leq 0 \end{cases} \tag{2.26}$$

Figure 2.3 demonstrates these four regions with their distinct material value and the corresponding sign of the level set function.

The union of the zero-level sets represent the edges in the image. The regions are disjoint sets. An image of unique region numbers is calculated easily by

$$I_R = \sum_{p=1}^{n_p} H(-\Phi_p) 2^{p-1}, \tag{2.27}$$

where the background region is defined by the value 0. It can be seen that n_p level set functions describe a total number of 2^{n_p} regions. The multiphase framework is implemented in this work and it gives several advantages, i.e.

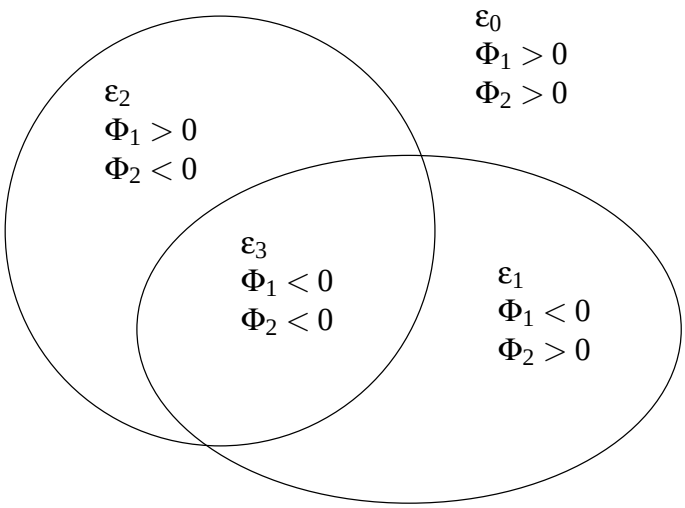

Figure 2.3: More than two phases are described by the combination of different level set functions.

- if one level set function splits into two regions, an additional level set function is generated adaptively,
- the level set function is removed if it describes no region anymore (in the case if the function is non-negative), and
- the tracking of the phases with their material values is performed easily due to the distinct region numbers.

Thus the number of unknown phases is adjusted adaptively and no a priori information is necessary. Additionally, the importance of the initial condition is reduced.

2.2 Definition of Shape Derivatives

The level set formulation describes a deformation of the boundary by the solution of (2.6). Therefore a descent direction of (1.8) must be calculated. Generally, this is a shape optimization problem and one has to calculate sensitivities of a functional with respect to a geometric variable such as the boundary of an open domain. In [76, 21] shape derivatives are introduced and this section gives a short overview over essential results. In this work the boundary $\Gamma(t) = \partial\Omega$ of an open set is supposed to be as smooth as necessary.

A real-valued shape functional J for an appropriate set of domains E is described by

$$J : E \to \mathbb{R}. \tag{2.28}$$

First two possible mathematical descriptions of deformations are explained. Next the shape derivative is introduced and the results for two simple shape functions (boundary and domain integrals) are given. In the following section the shape derivative concept is extended by material derivatives. This is necessary for more complex shape functions where a spatial distributed variable depends on the geometry itself. At last, results of the shape derivative concept applied to the level set function are presented. Additionally, second order derivatives are considered.

2.2.1 Flows of Velocity Fields

Instead of a parametrized curve, the interface is described by the boundary of an open set $\Omega \subset D$ in a given domain $D \subset \mathbb{R}^N$. Two types of deformation can be found in literature, namely, transformation and velocity method. The velocity method is also referred to as the speed method.

First consider the transformation around Ω along the one dimensional path

$$\forall \vec{X} \in D, t \geq 0, \quad T(t,\vec{X}) = T_t(\vec{X}) = \vec{X} + t\vec{V}(\vec{X}). \tag{2.29}$$

for some vector fields $\vec{V} : D \to \mathbb{R}^N$. This deformation is not completely satisfactory since it is a nonlocal transformation. In other words the velocity field $\frac{\mathrm{d}}{\mathrm{d}t}\vec{x}(t) = \vec{V}(\vec{X})$ at the point $\vec{x}(t) = T_t(\vec{X})$ depends on the point $\vec{X}$ instead on $\vec{x}(t)$.

More natural is the approach by the velocity (or speed) method. It describes the movement as flow for a given (smooth) vector field $\vec{V} : D \to \mathbb{R}^N$. Consider the trajectory of a point in the artificial time t, which is defined by following differential equation (initial value problem)

$$\frac{\mathrm{d}}{\mathrm{d}t}\vec{x}(t) = \vec{V}(\vec{x}(t)) \tag{2.30}$$

$$\vec{x}(0) = \vec{X} \tag{2.31}$$

for $t \geq 0$. This is now a local deformation or flow and it defines following mapping with respect to $\vec{V}$

$$T_t(\vec{X}) = \vec{x}(t), \quad t \geq 0 \tag{2.32}$$

by the solution of the differential equation. $\vec{V}$ is also called perturbation vector field. The deformation is a local deformation and the velocity of the point $\vec{x}(t)$ equals the field $\vec{V}$ evaluated at $\vec{x}(t)$. In literature one can find both deformations (transformation and velocity method) and they yield equal results for first order derivatives.

Two different kinds of vector fields can be defined. The field is named autonomous if it does not depend on t. In the other case it is non-autonomous if $\vec{V}(t)(x) = \vec{V}(t,x)$. Then the trajectory of a point is defined by following differential equation

$$\frac{\mathrm{d}}{\mathrm{d}t}\vec{x}(t) = \vec{V}(t,\vec{x}(t)), \tag{2.33}$$

$$\vec{x}(0) = \vec{X}. \tag{2.34}$$

In this work the vector field is assumed to be an autonomous field. To ensure that $T_t(\vec{x})$ maps $\overline{D}$ onto $\overline{D}$, the normal component of the velocity must vanish at ∂D

$$\vec{V}(\vec{x}) \cdot \vec{n}\Big|_{\partial D} = 0 \tag{2.35}$$

and on points where ∂D is not smooth the velocity is zero

$$\vec{V}(\vec{x})\Big|_{\partial D} = 0. \tag{2.36}$$

By utilization of the map $T_t(\vec{x})$ one can define the perturbation of a domain or boundary by

$$\Omega_t = \{T_t(\vec{x}) : \vec{x} \in \Omega\} = T_t(\Omega) \tag{2.37}$$

and

$$\Gamma_t = \{T_t(\vec{x}) : \vec{x} \in \Gamma\} = T_t(\Gamma). \tag{2.38}$$

2.2.2 Shape Derivative

The shape functional J has a Eulerian semiderivative at Ω in the direction $\vec{V}$ if the following limit exists and is finite

$$\mathrm{d}J(\Omega;\vec{V}) = \lim_{t\to 0} \frac{J(\Omega_t(\vec{V})) - J(\Omega)}{t}. \tag{2.39}$$

The functional J is said to be differentiable at Ω if the map $\vec{V} \mapsto dJ(\Omega;\vec{V})$ is linear and continuous for perturbation fields $\vec{V}$. In the analogous way one can define semiderivatives for Γ.

A simple example of a shape functional is given by the volume integral over a bounded open domain $\Omega \subset D$ with Lipschitzian boundary Γ and normal $\vec{n}$. Under appropriate assumptions on the vector field $\vec{V}$ and on the function $\psi : D \to \mathbb{R}$ the shape functional

$$J_1(\Omega_t(\vec{V})) = \int_{\Omega_t(\vec{V})} \psi \,\mathrm{d}x \tag{2.40}$$

yields the semiderivative

$$\mathrm{d}J_1(\Omega;\vec{V}) = \int_\Gamma \psi \vec{V} \cdot \vec{n} \,\mathrm{d}s. \tag{2.41}$$

The derivative of the surface integral

$$J_2(\Gamma_t(\vec{V})) = \int_{\Gamma_t(\vec{V})} \psi \,\mathrm{d}s \tag{2.42}$$

yields

$$\mathrm{d}J_2(\Gamma;\vec{V}) = \int_\Gamma \left(\frac{\partial \psi}{\partial n} + \kappa\psi\right) \vec{V} \cdot \vec{n} \,\mathrm{d}s \tag{2.43}$$

with the curvature $\kappa = \nabla \cdot \vec{n}$.

2.2.3 Material and Shape Derivative

More interesting is the case if ψ depends on the geometric variables themselves i.e. $\psi = \psi(\Omega)$. This yields more complex shape functionals and the derivatives have to be corrected by terms which take care of the derivative of ψ.

First the material derivative of the function ψ is defined by

$$\dot{\psi}(\Omega;\vec{V}) = \lim_{t\to 0} \frac{1}{t} \left(\psi(\Omega_t) \circ T_t(\vec{V}) - \psi(\Omega)\right) \tag{2.44}$$

if the limit exists. An analogous definition holds for functions $\psi(\Gamma)$. This is the derivative with respect to the geometry for a moving (Lagrangian) coordinate system[1]. In the special case that ψ does not depend on Ω one finds $\dot{\psi}(V) = \nabla\psi \cdot \vec{V}$. This leads to the definition of the shape derivative of ψ

$$\psi'(\Omega;\vec{V}) = \dot{\psi}(\Omega;\vec{V}) - \nabla\psi \cdot \vec{V}. \tag{2.45}$$

The shape derivative is zero for every function which does not depend on Ω. It is the derivative with respect to a fixed (Eulerian) coordinate system[2]. The shape and material derivatives for the level set function are given in subsection 2.2.4.

The derivatives of integrals like

$$J_1(\Omega) = \int_\Omega \psi(\Omega,\vec{x})\,\mathrm{d}x \tag{2.46}$$

and

$$J_2(\Gamma) = \int_\Gamma \psi(\Omega,\vec{x})\,\mathrm{d}s \tag{2.47}$$

yield following results

$$\boxed{\mathrm{d}J_1(\Omega;\vec{V}) = \int_\Omega \psi'(\Omega;V)\,\mathrm{d}x + \int_\Gamma \psi\vec{V}\cdot\vec{n}\,\mathrm{d}s} \tag{2.48}$$

and for boundary functions (note that it is assumed that $\psi : D \to \mathbb{R}$)

$$\mathrm{d}J_2(\Gamma;\vec{V}) = \int_\Gamma \psi'(\Omega;V)\,\mathrm{d}s + \int_\Gamma \left(\frac{\partial\psi}{\partial n} + \kappa\psi\right)\vec{V}\cdot\vec{n}\,\mathrm{d}s. \tag{2.49}$$

The last equation is simplified if one assumes a perturbation field of the form $\vec{V}_F = F\vec{n}$. This leads to

$$\boxed{\mathrm{d}J_2(\Gamma;\vec{V}_F) = \int_\Gamma \dot{\psi}(\Omega;F\vec{n})\,\mathrm{d}s + \int_\Gamma \kappa\psi F\,\mathrm{d}s.} \tag{2.50}$$

[1]Note that $\circ$ means *composed with*. The term $\psi(\Omega_t)\circ T_t(\vec{V})$ corresponds to the function value of ψ, which is altered by the deformed domain Ω_t and is evaluated in the new coordinating system.

[2]A possible interpretation of (2.45) is the total differentiation of ψ and in an analogous way (2.45) can be written as $\frac{\partial\psi}{\partial t} = \frac{\mathrm{d}\psi}{\mathrm{d}t} - \nabla\psi\cdot\frac{\mathrm{d}\vec{x}}{\mathrm{d}t}$.

2.2.4 Shape Derivative of Signed Distance Functions

In chapter 4 it is necessary to calculate the derivatives of different regularization terms. Additionally, second order derivatives are necessary. In this subsection shape and material derivatives of the signed distance function are discussed. The signed distance function is equal to the level set function, which has been utilized to describe the deformation. In [35, 36] one can find a detailed description of these calculations. In this section the main results are summarized.

First a distance function for a subset $A \subset \mathbb{R}^n$ is defined by

$$d_A(\vec{x}) = \inf_{\vec{y} \in A} |\vec{y} - \vec{x}|. \tag{2.51}$$

This leads to the definition of the signed distance function

$$b_\Omega(\vec{x}) = \begin{cases} d_\Gamma(\vec{x}) & \text{for } \vec{x} \in D \backslash \overline{\Omega} \\ 0 & \text{for } \vec{x} \in \Gamma \\ -d_\Gamma(\vec{x}) & \text{for } \vec{x} \in \Omega \end{cases}. \tag{2.52}$$

It is easy to see that $|\nabla b_\Omega| = 1$ almost everywhere. One can identify b_Ω with the level set function Φ, which has been introduced in section 2.1. In the special case of a signed distance function the normal and the curvature is calculated by

$$\vec{n} = \nabla \Phi \tag{2.53}$$

and

$$\kappa = \nabla \cdot \nabla \Phi. \tag{2.54}$$

The interface is described by the zero level set. Thus the derivative with respect to a moving coordinate system yields

$$\dot{\Phi} = 0 \tag{2.55}$$

on the interface $\Gamma(t)$. The shape derivative is calculated by (2.45)

$$\Phi' = -\vec{V}_F \cdot \vec{n} = -F \tag{2.56}$$

and yields a similar result as (2.6).

Second order derivatives are introduced in [35, 36]. The aim is to calculate

$$\mathrm{d}^2 J(\Gamma; \vec{V}_F; \vec{V}_G) = \mathrm{d}(\mathrm{d}J(\Gamma; \vec{V}_F))(\Gamma; \vec{V}_G) \tag{2.57}$$

for the perturbations $F, G : \Gamma \to \mathbb{R}$. Hintermüller and Ring suggest a few assumptions to simplify this calculation. These assumptions perfectly match the level set framework. First the velocity fields are restricted to a normal component, like

$$\vec{V}_F = F \cdot \vec{n}, \qquad \vec{V}_G = G \cdot \vec{n}. \tag{2.58}$$

Additionally, the following condition must hold near the interface Γ

$$\nabla \tilde{F} \cdot \vec{n} = 0, \qquad \nabla \tilde{G} \cdot \vec{n} = G. \tag{2.59}$$

This leads to $\frac{\partial}{\partial n}(\vec{V}_F \cdot \vec{n})\Big|_\Gamma = 0$ for $\tilde{F}$ and for $\tilde{G}$, respectively. Note that (2.59) is equal to (2.11). Hence this condition is satisfied if the velocity on the interface is extended as described in section 2.1.1. These restrictions on the velocity fields are necessary to obtain a symmetric second order derivative. The second order derivative of the shape function

$$J(\Gamma) = \int_\Gamma \psi \, \mathrm{d}s \tag{2.60}$$

is

$$\boxed{\mathrm{d}^2 J(\Gamma; \vec{V}_F; \vec{V}_G) = \int_\Gamma \left[\left(\frac{\partial^2 \psi}{\partial n^2} + 2 \frac{\partial \psi}{\partial n} \kappa \right) FG + \psi \nabla_\Gamma F \cdot \nabla_\Gamma G \right] \mathrm{d}s,} \tag{2.61}$$

whereas tangential calculus is used to define the tangential gradient of a function $h(\Gamma)$

$$\nabla_\Gamma h = \nabla \tilde{h}|_\Gamma - \frac{\partial \tilde{h}}{\partial n} \vec{n}. \tag{2.62}$$

for an arbitrary smooth extension $\tilde{h}$.

Concluding Remarks. In the first part of this chapter the level set framework is introduced. It is shown that this framework is a versatile tool to describe the interfaces of distinct regions. Additionally, the deformation of the contours is easily obtained by a velocity field. The second part of this chapter introduces shape and material derivatives. The differentiation of domain and boundary integrals is presented. In the following two chapters these derivatives are applied to the two terms of the cost functional (1.8). In chapter 3 the sensitivity of the potential and of the flux with respect to the deformation is calculated (least squares term). The consecutive chapter deals with the regularization term.

Chapter 3

Sensitivity Calculation and Boundary Element Method

In this work, the inverse problem of ECT is formulated as a shape optimization problem. The task is to find the minimizer of the cost functional (1.8) for all possible shapes and material values in the pipe. This chapter deals with the problem of finding an expression for the derivative of the potential and of the flux with respect to the deformation of a contour. Additionally, the sensitivity with respect to the permittivity values is calculated. Depending on the applied boundary condition, one is interested in the shape derivative of the potential in the domain of the electrode Ω_e

$$u'\big|_{\Omega_e} \tag{3.1}$$

or of the flux on the electrode surface Γ_e

$$\int_{\Gamma_e} \left(\varepsilon \frac{\partial u}{\partial n} \right)' \mathrm{d}s, \tag{3.2}$$

where u satisfies the partial differential equation (1.1) of the field problem. The interfaces of the different regions are separating the piecewise constant permittivity values. These boundaries are assumed to be sufficiently smooth.

One may use different approaches for this differentiation, like

- finite differences [25, 26],
- direct differentiation of an analytical expression,
- direct differentiation of system matrices [62], and
- the Adjoint Variable Method (AVM) [42, 41].

Finite differences lead to a high number of field problems and therefore it is very time consuming. Additionally, numerical instability occurs very often. An analytical expression is only available for simple geometries. For the direct differentiation of the BEM system matrices one has to construct matrices with the partial derivatives of each node

point (see e.g. [62]). In this work the adjoint variable method is utilized and it is shown that few additional computation time is necessary to calculate the sensitivity.

In appendix A one can find an introducing, one dimensional example. For this simple example an analytical expression exists and it is compared to the result of the adjoint variable method. This appendix illustrates the necessary steps to gain a suitable equation for the shape derivative. In the first section in this chapter the adjoint variable method is applied to the geometry of the ECT sensor and an expression for the shape derivative is obtained. Two distinct adjoint problems are defined, one for the derivative of the electrode potential and the other for the derivative of the charge on the electrode. At last details about the implemented BEM are given and the computational effort is discussed.

3.1 Shape Derivatives in 2D

The construction of a sensitivity formula in 2D is similar to the process in 1D. The derivation in this section has a similar procedure as described in [56, 5]. The velocity field is restricted to the case where it consists only of the normal component similar to (2.58) ($\vec{V}_F = F\vec{n}$). First only one region with constant permittivity is considered and

$$\varepsilon \Delta u = 0 \tag{3.3}$$

is fulfilled in the domain Ω with the sufficiently smooth boundary Γ (note that the application of Dirichlet and Neumann conditions is discussed later in this section). The shape derivative (2.45) of the primary variable u and adjoint variable $\overline{u}$ is defined as follows.

$$u' = \dot{u} - \frac{\partial u}{\partial n} F \tag{3.4}$$

$$\overline{u}' = \dot{\overline{u}} - \frac{\partial \overline{u}}{\partial n} F \tag{3.5}$$

First the weak formulation is considered

$$\underbrace{\int_\Omega \varepsilon \nabla u \cdot \nabla \overline{u} \, \mathrm{d}x}_{S_1} - \underbrace{\int_\Gamma \overline{u} \varepsilon \frac{\partial u}{\partial n} \, \mathrm{d}s}_{S_2} = 0. \tag{3.6}$$

The shape derivative of the domain integral yields

$$\mathrm{d}S_1(\Omega; \vec{V}_F) = \int_\Omega (\varepsilon \nabla u \cdot \nabla \overline{u})' \, \mathrm{d}x + \int_\Gamma \varepsilon \nabla u \cdot \nabla \overline{u} F \, \mathrm{d}s \tag{3.7}$$

and it is simplified by the Gauss' theorem to

$$\mathrm{d}S_1(\Omega; \vec{V}_F) = \int_\Omega \left(\varepsilon' \nabla u \cdot \nabla \overline{u} - u' \varepsilon \Delta \overline{u} \right) \mathrm{d}x + \int_\Gamma \left(u' \varepsilon \frac{\partial \overline{u}}{\partial n} + \overline{u}' \varepsilon \frac{\partial u}{\partial n} + \varepsilon \nabla u \cdot \nabla \overline{u} F \right) \mathrm{d}s. \tag{3.8}$$

Similar to the 1D example in appendix A.2, the shape derivatives on the boundary are replaced by the material derivative such that

$$\begin{aligned} \mathrm{d}S_1(\Omega;\vec{V}_F) = &\int_\Omega \left(\varepsilon'\nabla u\cdot\nabla\bar{u} - u'\varepsilon\Delta\bar{u}\right)\mathrm{d}x \\ &+\int_\Gamma\left(\dot{u}\varepsilon\frac{\partial\bar{u}}{\partial n}+\dot{\bar{u}}\varepsilon\frac{\partial u}{\partial n}+\varepsilon\nabla u\cdot\nabla\bar{u}F-2\varepsilon\frac{\partial u}{\partial n}\frac{\partial\bar{u}}{\partial n}F\right)\mathrm{d}s. \end{aligned} \tag{3.9}$$

Later the material derivatives of the interface conditions are used to eliminate these terms. The shape derivative of the boundary integral S_2 is achieved by (2.50) and yields

$$\mathrm{d}S_2(\Omega;\vec{V}_F) = \int_\Gamma\left[\dot{\bar{u}}\varepsilon\frac{\partial u}{\partial n}+\bar{u}\left(\varepsilon\frac{\partial u}{\partial n}\right)^{\cdot}+\bar{u}\varepsilon\frac{\partial u}{\partial n}\kappa F\right]\mathrm{d}s. \tag{3.10}$$

Both shape derivatives $\mathrm{d}S_1$ and $\mathrm{d}S_2$ lead to following result.

$$\begin{aligned} &\int_\Omega u'\varepsilon\Delta\bar{u}\,\mathrm{d}x+\int_\Gamma\left[\bar{u}\left(\varepsilon\frac{\partial u}{\partial n}\right)^{\cdot}-\dot{u}\varepsilon\frac{\partial\bar{u}}{\partial n}\right]\mathrm{d}s \\ &=\int_\Omega\varepsilon'\nabla u\cdot\nabla\bar{u}\,\mathrm{d}x+\int_\Gamma\left(\varepsilon\nabla u\cdot\nabla\bar{u}-2\varepsilon\frac{\partial u}{\partial n}\frac{\partial\bar{u}}{\partial n}-\bar{u}\varepsilon\frac{\partial u}{\partial n}\kappa\right)F\,\mathrm{d}s \end{aligned} \tag{3.11}$$

The left hand side of this equation consists of the shape and material derivatives of the primary variable u. The domain integral on the right hand side corresponds to a change in the permittivity value and the boundary integral corresponds to a deformation of the boundary.

Two Subregions. The result (3.11) is applied to the setup shown in figure 3.1. The region Ω_1 is inside of Ω_2 and the interface between them is denoted by Γ_1. Dirichlet and Neumann boundary conditions are applied on $\Gamma_0 = \Gamma_d \cup \Gamma_n$. It is assumed that the velocity field $\vec{V}_F$ satisfies (2.35) and (2.36) on Γ_0. Thus the outer boundary of this setup is not deformed. Additionally, it is assumed that the boundary conditions do not depend on the geometry (i.e. Γ_1). The interface conditions on Γ_1 are (if necessary the quantities of each region are distinguished by the corresponding subscript)

$$u_1 = u_2 \tag{3.12}$$

$$\varepsilon_1\frac{\partial u_1}{\partial n} = \varepsilon_2\frac{\partial u_2}{\partial n} \tag{3.13}$$

with $\vec{n}$ the outward normal vector of region Ω_1. These conditions are fulfilled for all Γ_t and their material derivatives lead to

$$\dot{u}_1 = \dot{u}_2 \tag{3.14}$$

$$\left(\varepsilon_1\frac{\partial u_1}{\partial n}\right)^{\cdot} = \left(\varepsilon_2\frac{\partial u_2}{\partial n}\right)^{\cdot}. \tag{3.15}$$

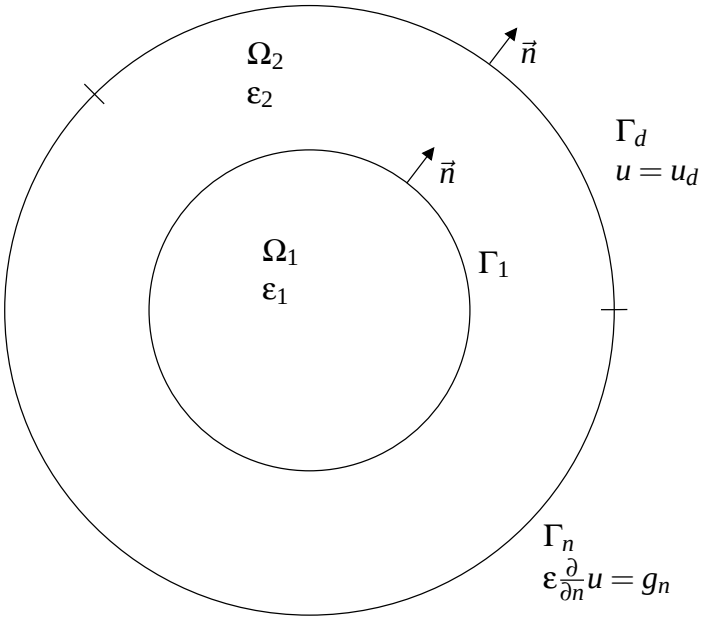

Figure 3.1: Two subregions Ω_1 and Ω_2 with different constant permittivity values. On the boundaries Γ_d and Γ_n Dirichlet and Neumann boundary conditions are applied. The interface between the two regions is described by Γ_1.

Similar interface conditions are applied for the adjoint variable $\bar{u}$

$$\bar{u}_1 = \bar{u}_2 \tag{3.16}$$

$$\varepsilon_1 \frac{\partial \bar{u}_1}{\partial n} = \varepsilon_2 \frac{\partial \bar{u}_2}{\partial n}. \tag{3.17}$$

The shape derivative (3.11) is applied for both domains. The material derivatives on the boundary Γ_1 and the term with the curvature are eliminated if both shape derivatives are summed up and if their interface conditions are applied. This yields

$$\int_\Omega u' \varepsilon \Delta \bar{u} \, \mathrm{d}x + \int_{\Gamma_0} \left[\bar{u}_2 \left(\varepsilon_2 \frac{\partial u_2}{\partial n} \right)^{\cdot} - \dot{u}_2 \varepsilon_2 \frac{\partial \bar{u}_2}{\partial n} \right] \mathrm{d}s = \int_\Omega \varepsilon' \nabla u \cdot \nabla \bar{u} \, \mathrm{d}x$$
$$+ \int_{\Gamma_1} \left(\varepsilon_1 \nabla u_1 \cdot \nabla \bar{u}_1 - 2\varepsilon_1 \frac{\partial u_1}{\partial n} \frac{\partial \bar{u}_1}{\partial n} - \varepsilon_2 \nabla u_2 \cdot \nabla \bar{u}_2 + 2\varepsilon_2 \frac{\partial u_2}{\partial n} \frac{\partial \bar{u}_2}{\partial n} \right) F \, \mathrm{d}s. \tag{3.18}$$

The material derivatives of the primary variable only occur on the outer boundary Γ_0. This boundary consists of two parts with different boundary conditions. In ECT, these boundary conditions do not depend on the geometry. On Γ_d Dirichlet boundary conditions are applied and the material derivative equals zero.

$$u|_{\Gamma_d} = u_d \tag{3.19}$$

$$\dot{u}|_{\Gamma_d} = 0 \tag{3.20}$$

Similar the material derivative of the displacement on Γ_n yields

$$\varepsilon \frac{\partial u}{\partial n}\bigg|_{\Gamma_n} = g_n \tag{3.21}$$

$$\left(\varepsilon \frac{\partial u}{\partial n}\right)^{\cdot}\bigg|_{\Gamma_n} = 0. \tag{3.22}$$

The boundary integral over Γ_1 is further simplified by splitting ∇u in a normal and tangential component. The tangential component is denoted by $E_t\vec{t}$ [1] and the normal component is given by $E_{n,1}\vec{n}$ and $E_{n,2}\vec{n}$ [2] for each region. The over line denotes the adjoint variable.

$$\begin{aligned}
&\varepsilon_1(E_t\vec{t}+E_{n,1}\vec{n})\cdot(\overline{E}_t\vec{t}+\overline{E}_{n,1}\vec{n}) - 2\varepsilon_1 E_{n,1}\overline{E}_{n,1}\\
-&\varepsilon_2(E_t\vec{t}+E_{n,2}\vec{n})\cdot(\overline{E}_t\vec{t}+\overline{E}_{n,2}\vec{n}) + 2\varepsilon_2 E_{n,2}\overline{E}_{n,2}\\
=&\varepsilon_1 E_t\overline{E}_t - \varepsilon_1 E_{n,1}\overline{E}_{n,1} - \varepsilon_2 E_t\overline{E}_t + \varepsilon_2 E_{n,2}\overline{E}_{n,2}\\
=&(\varepsilon_1-\varepsilon_2)(E_t\overline{E}_t + E_{n,1}\overline{E}_{n,2})\\
=&(\varepsilon_1-\varepsilon_2)\nabla u_1\cdot\nabla\overline{u}_2
\end{aligned} \tag{3.23}$$

Hence (3.18) is simplified to

$$\boxed{\begin{aligned}
&\int_\Omega u'\varepsilon\Delta\overline{u}\,\mathrm{d}x + \int_{\Gamma_d}\overline{u}_2\left(\varepsilon_2\frac{\partial u_2}{\partial n}\right)^{\cdot}\mathrm{d}s - \int_{\Gamma_n}\dot{u}_2\varepsilon_2\frac{\partial\overline{u}_2}{\partial n}\,\mathrm{d}s\\
=&\int_\Omega \varepsilon'\nabla u\cdot\nabla\overline{u}\,\mathrm{d}x + (\varepsilon_1-\varepsilon_2)\int_{\Gamma_1}\nabla u_1\cdot\nabla\overline{u}_2 F\,\mathrm{d}s.
\end{aligned}} \tag{3.24}$$

Generally, a similar result is obtained if more than two regions are considered. On the left hand side shape and material derivatives of the primary variable occur. The adjoint problem is defined in such way that the desired sensitivity is obtained. The right hand side consists of two terms. The first term corresponds to the sensitivity with respect to the material value. The second integral is related to a material jump and to a deformation of the interface with velocity F.

3.1.1 Sensitivity of the Potential

In ECT, the electrodes are not deformed and thus $\dot{u} = u'$ holds ($\tilde{F} = 0$ on the electrode surface). To calculate the sensitivity of the potential, consider the region of the electrode

[1] E_t is the tangential component of the electric field strength (the negative sign is omitted for sake of simplicity).

[2] $E_{n,1}$ and $E_{n,2}$ denote the electric field strength in normal direction for region 1 and 2, respectively.

Ω_e and its characteristic function χ_e. The characteristic function equals 1 if $x \in \Omega_e$ and 0 else. Then the adjoint problem is defined as follows.

$$\begin{aligned} \nabla \cdot (\varepsilon \nabla \bar{u}) &= \chi_e \\ \bar{u}|_{\Gamma_d} &= 0 \\ \varepsilon \frac{\partial \bar{u}}{\partial n}\Big|_{\Gamma_n} &= 0 \end{aligned} \tag{3.25}$$

With these definitions (3.24) leads to

$$\int_{\Omega_e} \dot{u}\,\mathrm{d}x = \int_{\Omega} \varepsilon' \nabla u \cdot \nabla \bar{u}\,\mathrm{d}x + (\varepsilon_1 - \varepsilon_2) \int_{\Gamma_1} \nabla u_1 \cdot \nabla \bar{u}_2 F\,\mathrm{d}s. \tag{3.26}$$

This equation is used if one is interested in the change of the electrode potential. This corresponds to the high impedance approach of the measurement circuit. The new hardware concept [89] is based on low impedance electrodes [3] and this case is considered in the following subsection.

An identical result for the second term in (3.26) is obtained in [41] for electrical impedance tomography. In this paper the sensitivity with respect to a deformation is calculated for two regions with a priori known and constant conductivity values.

3.1.2 Sensitivity of the Charge

If one is interested in the change of the electrode charge, a different adjoint problem is defined. This is necessary for the low impedance approach i.e. the forward problem is defined by (1.1). In this case, only Dirichlet boundary conditions are applied to the electrodes. The boundary of the electrode of interest is denoted by $\Gamma_{e,i}$ and following adjoint problem is defined.

$$\begin{aligned} \nabla \cdot (\varepsilon \nabla \bar{u}) &= 0 \\ \bar{u}|_{\Gamma_0} &= 0 \\ \bar{u}|_{\Gamma_{e,i}} &= 1 \end{aligned} \tag{3.27}$$

The sensitivity of the measured charge is obtained by

$$\int_{\Gamma_{e,i}} \left(\varepsilon \frac{\partial u}{\partial n}\right)^{\cdot} \mathrm{d}s = \int_{\Omega} \varepsilon' \nabla u \cdot \nabla \bar{u} \, \mathrm{d}x + (\varepsilon_1 - \varepsilon_2) \int_{\Gamma_1} \nabla u_1 \cdot \nabla \bar{u}_2 F \, \mathrm{d}s. \tag{3.28}$$

where $\vec{n}$ on Γ_e is the inward normal vector of the electrode. Similar to the previous section it is assumed that $\tilde{F} = 0$ on Γ_e.

3.2 Boundary Element Method

The boundary element method is utilized to solve the forward problem. In the practical application different questions arise. First the discretization into boundary elements of the sensor and of interior objects is discussed. Next the formulation of the boundary element method is introduced. The subsection deals with the discretization of the boundary integrals for the sensitivity calculation.

Discretization into Boundary Elements. Figure 3.2 shows the discretization of an expedient model of the ECT sensor into boundary elements. Section 1.1 gives a detailed discussion about the appropriate assumptions for the application of a two dimensional model. Without interior material, it consists of three regions of interest, namely, the PVC pipe, the interior of the pipe, and the region with the grounded shield at the outermost circumference. The 16 electrodes are assumed to be perfectly conductive and each of them is an equipotential surface. Thus it is not necessary to solve the Laplace equation for these regions.

The interior objects are described by the level set function Φ. To discretize the boundary it is necessary to track the contour i.e. one has to solve (2.1). This is illustrated in figure 3.3. The level set function is discretized on a fixed Cartesian grid and the function is assumed to be linear between the grid points. Additional points are computed on the grid line, where $\Phi = 0$. These points are connected to a polygon of boundary elements. Similar one can construct the boundary elements for the multiphase level set method.

The front-ends of the prototype measure the displacement current for different active electrodes. In fact, each electrode acts successively as transmitting electrode whereas the other 15 electrodes are measuring. A total number of 240 measurements is obtained. Due to the symmetry of the measurement this is twice the number of independent capacitances. In other words, the displacement current remains the same if measuring and exciting electrodes are reversed. Averaging of these measured displacement currents is used to reduce this redundancy.

Formulation of the Boundary Element Method. One advantage of the boundary element method is that it reduces the dimension of the problem by one [53]. In 2D it

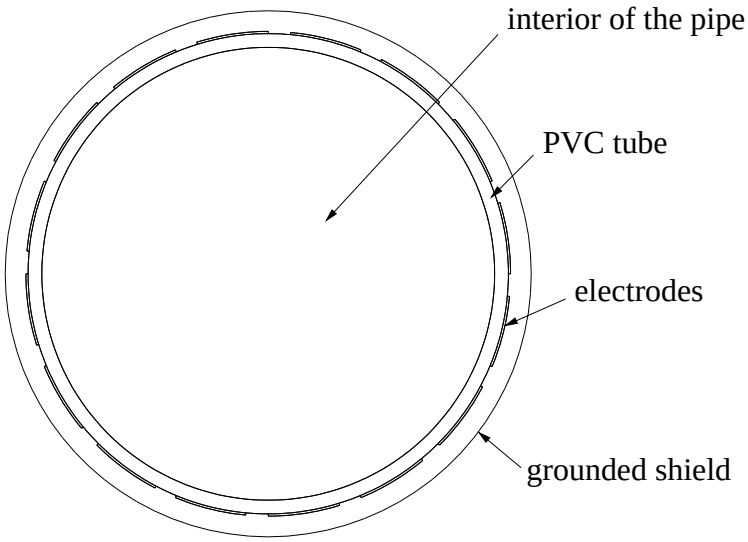

Figure 3.2: The sensor is discretized into boundary elements. It consists of the PVC pipe, the interior region with the unknown materials, the 16 electrodes that are mounted around the pipe, and the outermost region with the grounded shield.

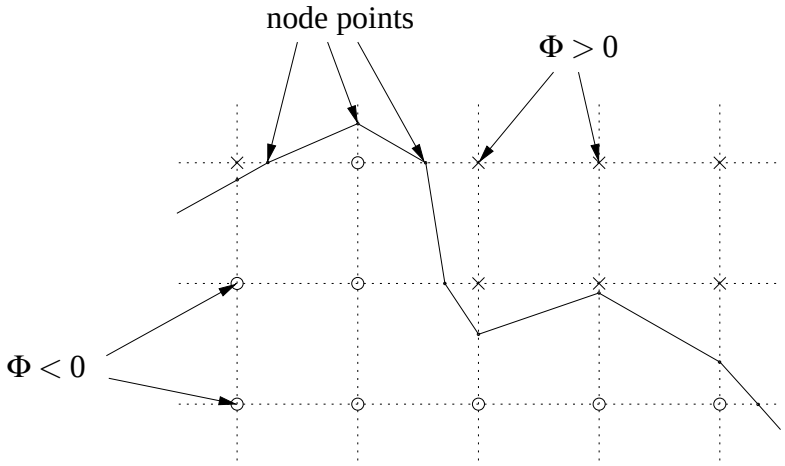

Figure 3.3: Discretization of the interior object into boundary elements. The level set function is discretized on a fixed grid (dotted lines). The sign of the level set function is marked by small circles and x symbols. The node points of the straight boundary elements are calculated on the grid lines by linear interpolation.

discretizes only the interface of regions with constant permittivity. A further advantage is that it gives the solution of the partial differential equation explicitly. This is in contrast to the finite element method where an interpolation of the solution onto a grid is performed. For a moving geometry and a changing topology it is a great advantage to have an accurate solution without the need of remeshing of the whole domain. The boundary element method is mainly restricted to linear partial differential equations. In this work, however, it is assumed that the materials in the interior of the pipe are linear. In other words the material value does not depend on the electric field strength.

A short introduction in inverse problems with boundary elements is given in [53]. An application to elasticity is given. A detailed description of the BEM itself is given

for instance in [13]. The BEM leads to dense stiffness matrices, which restrict its usage to problems of small size. To speed up the calculation, especially in three dimensions, fast boundary element techniques [81] are utilized. These techniques improve the BEM with respect to storage requirements as well as the complexity of matrix times vector multiplications.

Basically, the solution of $\Delta u = 0$ in terms of boundary integrals is

$$\frac{1}{2}u(\vec{x}) + \int_\Gamma u(\vec{y})\frac{\partial}{\partial n}U^*(\vec{x},\vec{y})\,\mathrm{d}s_y = \int_\Gamma U^*(\vec{x},\vec{y})\frac{\partial}{\partial n}u(\vec{y})\,\mathrm{d}s_y \tag{3.29}$$

for $\vec{x} \in \Gamma$. [3] U^* is the so called fundamental solution and in 2D one obtains

$$U^*(\vec{x},\vec{y}) = -\frac{1}{2\pi}\log|\vec{x}-\vec{y}|. \tag{3.30}$$

In this work a direct formulation for the Dirichlet boundary value problem is used [81]. The unknown variables in the resulting equation system are physical values. One starts with the boundary integral equation (3.29) and the integrals are discretized in linear boundary elements in a geometrical sense. Each element has constant values u_i and $f_i = \frac{\partial}{\partial n}u$. The collocation method is used to assemble the corresponding matrices of the boundary integrals and the discretization of (3.29) is evaluated at each midpoint of a boundary element. An analytical evaluation of the integrals is possible due to the constant and linear boundary elements. This results in

$$\mathbf{H}_b\vec{u} = \mathbf{G}_b\vec{f} \tag{3.31}$$

where $\vec{u}$ and $\vec{f}$ summarize the physical quantities at each boundary element. For additional subregions interface conditions are used to combine the individual matrices.

This simple formulation leads to dense blocks in the resulting system matrix, which is not symmetric in general. The equation is solved by a direct approach with Gauss elimination. Possible improvements are e.g. a symmetric Galerkin formulation or the usage of elements of higher order.

3.2.1 Discretization of the Sensitivity Equation

The first term of the cost functional (1.8) consists of the weighted least squares of the calculated and measured electrode charges. At iteration step k this term reads as follows.

$${I_1}^k = \frac{1}{2}\left\|\mathbf{W}\left(\vec{q}^k - \vec{q}_m\right)\right\|^2. \tag{3.32}$$

The gradient and an approximated Hessian matrix of this part of the cost functional are calculated by the Jacobian matrix. This matrix consists of the partial derivatives of each charge with respect to the change in geometry and material properties. The deformation is described by the velocity F_j on different node points along the boundary and they are

[3] The term $\frac{1}{2}$ in (3.29) is obtained for a smooth boundary Γ.

summarized into $\vec{F}$ of size n_j. The change in the material values is denoted by $\vec{\delta\varepsilon}$ (size n_l). By neglecting higher order terms the charges $\vec{q}$ are represented by Taylor expansion

$$\vec{q}^{k+1} = \vec{q}^{k} + \mathbf{J}_\Gamma \vec{F} + \mathbf{J}_\varepsilon \vec{\delta\varepsilon} \tag{3.33}$$

with the Jacobian matrices $\mathbf{J}_\Gamma$ of size $n_i \times n_j$ and $\mathbf{J}_\varepsilon$ of size $n_i \times n_l$. The Jacobian matrices are assembled with the partial derivatives

$$J_{\Gamma,ij} = \frac{\partial q_i}{\partial F_j} \tag{3.34}$$

and

$$J_{\varepsilon,il} = \frac{\partial q_i}{\partial \varepsilon_l}. \tag{3.35}$$

The function value at iteration step $k+1$ is written as

$$I_1{}^{k+1} = I_1{}^{k} + \vec{\delta}^T \vec{g}_1 + \frac{1}{2}\vec{\delta}^T \mathbf{G}_1 \vec{\delta} \tag{3.36}$$

where the change in geometry and permittivity is summarized into

$$\vec{\delta} = \begin{pmatrix} \vec{F} \\ \vec{\delta\varepsilon} \end{pmatrix}. \tag{3.37}$$

The gradient of the weighted least squares (3.32) is defined by (note that $\mathbf{W}^T\mathbf{W} = \mathbf{C}^{-1}$)

$$\vec{g}_1 = \begin{pmatrix} \mathbf{J}_\Gamma{}^T \mathbf{C}^{-1}(\vec{q}^k - \vec{q}_m) \\ \mathbf{J}_\varepsilon{}^T \mathbf{C}^{-1}(\vec{q}^k - \vec{q}_m) \end{pmatrix} \tag{3.38}$$

and the Hessian is approximated by

$$\mathbf{G}_1 = \begin{pmatrix} \mathbf{J}_\Gamma{}^T \mathbf{C}^{-1} \mathbf{J}_\Gamma & \mathbf{J}_\Gamma{}^T \mathbf{C}^{-1} \mathbf{J}_\varepsilon \\ \mathbf{J}_\varepsilon{}^T \mathbf{C}^{-1} \mathbf{J}_\Gamma & \mathbf{J}_\varepsilon{}^T \mathbf{C}^{-1} \mathbf{J}_\varepsilon \end{pmatrix}. \tag{3.39}$$

Jacobian Matrix $\mathbf{J}_\Gamma$. The boundary integral of the right hand side of (3.28) determines the change of the electrode charge with respect to F. For the adjoint problem for the electrode i a Dirichlet boundary condition is valid on the corresponding electrode surface $\Gamma_{e,i}$. The integral is discretized by the boundary elements $\Gamma_{b,j}$. The outward normal vector of the boundary element defines an interior and an exterior region, which are denoted by the subscript 1 and 2, respectively. Under assumption of a constant velocity F_j on each boundary element in the direction of the normal vector, the entries of the Jacobian are

$$J_{\Gamma,ij} = (\varepsilon_1 - \varepsilon_2) \int_{\Gamma_{b,j}} \nabla u_1 \cdot \nabla \bar{u}_2 \, \mathrm{d}s. \tag{3.40}$$

If a linear velocity function is assumed on each boundary element, the unknown elements F_j are defined on the node points. A similar equation for the elements in the Jacobian

can be derived. Further details on the discretization of the velocity function are given in appendix B.

The gradient is expressed by a normal and a tangential component. The normal component is known from the solution of the boundary element method. The necessary tangential component can be obtained e.g. by direct differentiation of the system matrices, by differentiation of equation (3.29), and by finite differences of the potential u along the boundary elements. In this work central finite differences are utilized for a fast calculation of this part of the gradient.

Jacobian Matrix $\mathbf{J}_\varepsilon$. An element of this Jacobian is obtained by evaluation of the domain integral in (3.28). The adjoint problem is determined as before and the electrode $\Gamma_{e,i}$ acts as exciting electrode. The domain with constant material value ε_l is denoted by Ω_l and its boundary is Γ_l. With the Gauss' theorem the domain integral is transformed into a boundary integral

$$J_{\varepsilon,il} = \int_{\Omega_l} \nabla u \cdot \nabla \bar{u} \, \mathrm{d}x = \int_{\Gamma_l} u \frac{\partial \bar{u}}{\partial n} \, \mathrm{d}s \tag{3.41}$$

since $\nabla \cdot \nabla \bar{u} = 0$. The resulting integral can be evaluated easily due to the fact that the necessary quantities are computed directly by the boundary element method.

Computational Effort. The necessary computations for one iteration step are summarized as follows.

1. Find the zero level set by (2.1) and discretize the unknown objects into boundary elements.

2. Calculate the electrode charges $\vec{q}^k$ by the flux integrating method (1.2). Therefore 16 forward problems of type (1.1) are solved. The boundary conditions are defined by the corresponding measurement setup.

3. For each forward problem 15 adjoint problems (for each measurement electrode) are defined according to (3.27) and solved. In fact, only 120 independent measurements exist due to the symmetry. Thus only one half of the adjoint problems is necessary.

4. Next the tangential component of the gradients ∇u and $\nabla \bar{u}$ is determined by finite differences.

5. The Jacobian matrices $\mathbf{J}_\Gamma$ and $\mathbf{J}_\varepsilon$ are assembled by numerical evaluation of the corresponding boundary integrals.

For these steps a charge based prototype is assumed with 16 electrodes. In the case of the charge based measurement principle, only Dirichlet boundary conditions are applied for the forward and adjoint problems. Therefore it is straightforward to use the superposition of only 16 independent field problems to calculate all necessary field problems. This principle can be applied under the assumption that the permittivities do not depend on the electric field strength. Each independent field problem applies a Dirichlet boundary

condition $u = 1$ on a different electrode and homogeneous Dirichlet boundary conditions on all other electrodes. It is also possible to apply this procedure to the case of voltage based measurements. Hence the overall number of field problems, which have to be solved, is equal to the number of electrodes. Furthermore only the boundary conditions change for each field problem. That means that the system matrix remains the same and merely the right hand side of the equation systems differs.

Chapter 4

A Priori Information and Regularization Terms

A problem is called well-posed in the sense of Hadamard if for every data a solution exists, this solution is unique, and the solution is stable with respect to perturbations in the data. If any of these three conditions does not hold, the problem is called ill-posed (compare with [28, 87]). Unfortunately, the inverse problem of electrical capacitance tomography is ill-posed and its solution is unstable with respect to data perturbations. This creates serious numerical problems. The Hessian matrix (3.39) is ill-conditioned, which is indicated by the decay of its singular values. To cope with this instability, so called regularization methods are implemented. In section 1.2 the knowledge of a prior probability density $\pi_{pr}(\varepsilon)$ is assumed. The reconstruction is stable with this additional information, which is incorporated by the regularization term R with the regularization parameter α^2. This kind of regularization is of Tikhonov type.

In the community of image processing and level set techniques one idea is to use so called shape priors. Even though shape priors are possible regularization techniques, it is necessary to have a good idea of the shape of the objects to be recovered. Generally, this is not fulfilled in capacitance tomography for industrial processes and thus this technique is not applicable.

Commonly, no particular a priori information is available. In absence of this information it is reasonable to apply a smoothness assumption on the solution. In ECT, this means that the permittivity value in the interior pipe is assumed to be smooth. The disadvantage is that the reconstructed image is blurred and has less spatial resolution. Even for a shape reconstruction method, which assumes piecewise constant permittivity values, additional information is necessary. As a consequence of describing the interfaces between regions with constant permittivities, a regularization, which smoothes the solution in a region, is no longer applicable. Instead a smoothness assumption on the contour has to be applied to avoid zig-zagging of the interfaces. Following regularization methods are proposed in literature:

- implicit regularization where a parameterization of the contour with as few coefficients as possible is applied,
- penalization of the arc length of the interface between materials as suggested in

[42, 41],

- the Mumford-Shah functional [66],
- total variation regularization [17, 18, 20].

In the case of a parameterization of the interface, a limited number of coefficients is used. For instance the Fourier coefficients of higher order are truncated and high frequencies in the trace of the contour are avoided. This characteristic is, however, not easy to control. Often the arc length of the interface is penalized which also results in smooth contours between different materials. This term does not depend on the material values themselves. This regularization term is often applied if the material values are assumed to be known a priori. This can rise a problem if the material values are reconstructed simultaneously to the shape. The Mumford-Shah functional consists of two parts with particular parameters. One term leads to piecewise smooth images and the second term yields simplicity of the edge set between the different smooth parts of the image. The Mumford-Shah functional has more than one tuning (regularization) parameter, which are difficult to determine in practical applications. At last the Total Variational Regularization (TVR) can be used. This method originates from image processing (as well as the Mumford-Shah functional). It is suitable for blocky images (piecewise smooth images) similar to the Mumford-Shah functional but it has only one regularization parameter.

Many different approaches exist for the choice of the regularization parameter. Common methods are the Generalized Cross Validation (GCV), the discrepancy principle, or the L-curve method. A detailed discussion of these methods can be found e.g. in [28, 87]. The influence of the regularization parameter on the reconstructed image quality is presented in chapter 5.

In this chapter appropriate regularization terms are discussed. First of all the Newton method, which is applied to find the minimum of shape functionals, is introduced. In the following three sections different regularization terms are discussed, namely, the regularization of the arc length, a regularization, which consists of the squared jump in the material value multiplied by the arc length, the Mumford-Shah functional, and total variational regularization. Details about the discretization and about the assembling of the gradient and Hessian matrix are given in appendix B. Section 4.5 introduces a regularization where prior information is known from ultrasonic reflection tomography. The last section deals with constraints. These constraints incorporate some kind of a priori information on the solution. In case of ECT the permittivity is constrained to values above one and geometrical constraints are applied to the unknown interface.

4.1 Newton Method

As discussed in chapter 3, the Gauss-Newton method is appropriate for the first term of the cost functional (1.8). A Newton-type method converges much faster, however one needs to know the Hessian matrix. Thus, the second order derivative of the second term (regularization term) is necessary as well. Generally, the regularization term can be

considered of type (2.60)

$$J(\Gamma) = \int_{\Gamma} \psi \, ds.$$

Commonly, the descent direction, which is defined by the shape derivative, is used. This shape gradient based flow has slower propagation compared with a Newton type flow. In [35, 36] the Newton-type speed function is defined as follows.

$$\boxed{d^2J(\Gamma;\vec{V}_F;\vec{V}_G) = -dJ(\Gamma;\vec{V}_G) \qquad \text{for all } G : \Gamma \to \mathbb{R}} \tag{4.1}$$

This equation is used to assemble the Hessian matrix and the gradient of the regularization term. The conditions (2.58) and (2.59) are assumed to hold for $\vec{V}_F$ and $\vec{V}_G$ as discussed in section 2.2.4. G is an appropriate test function and a detailed discussion of the discretization is given in the appendix B. The Hessian matrices for both terms in (1.8) are combined and weighted by the regularization parameter. Finally, the Newton-type descent direction is calculated in the optimization framework.

One important issue is that the Hessian must be positive definite, which means that the curvature of the objective function is always positive. This assures that a descent direction is calculated. The Gauss-Newton approximation of the Hessian is at least positive semidefinite. Generally, the Hessian of the regularization parameter is calculated by (2.61). This part is only positive definite under some assumptions on ψ and in practical applications it is necessary to modify this term in such a way that it is convex. This problem is addressed in the sections 4.3 and 4.5.

Another issue is that complex topologies can occur if the multiphase level set framework is applied. For instance, if two level set functions overlap, junctions occur and arbitrary angles are allowed at these edges. The regularization term, however, is written as sum over all individual level set functions. The contour of one level set function is smooth enough to allow a shape sensitivity calculation.

4.2 Regularization by the Arc Length

Many shape reconstruction methods assume a priori known material values of the distinct phases. These values are held constant during the reconstruction process. A straight forward way to implement a regularization is to penalize the arc length of the interface. This is done by

$$\boxed{R_{arc} = \sum_{p=1}^{n_p} \int_{\Gamma_p} ds.} \tag{4.2}$$

where the arc length of all level set functions is summed up. The weight between the least squares part of the cost functional and the regularization term is adjusted by the regularization parameter α^2. The reconstructed trace of each region is smooth because zig-zagging is effectively avoided. Numerical results are presented in chapter 5.

By setting $\psi = 1$, the shape sensitivity calculated by (2.43) and (2.61) yields

$$\mathrm{d}R_{arc}(\Gamma;\vec{V}_G) = \int_\Gamma \kappa G \,\mathrm{d}s \tag{4.3}$$

and

$$\mathrm{d}^2R_{arc}(\Gamma;\vec{V}_F;\vec{V}_G) = \int_\Gamma \nabla_\Gamma F \cdot \nabla_\Gamma G \,\mathrm{d}s. \tag{4.4}$$

For the sake of simplicity it is assumed that only one level set function exists. The integral in (4.4) represents the so called Laplace-Beltrami operator, which is defined e.g. in [76]. It is easy to see that the shape Hessian is positive semi-definite i.e. $\mathrm{d}^2R_{arc}(\Gamma;\vec{V}_F;\vec{V}_F) \geq 0$. The assembling of the gradient and the Hessian matrix is shown in appendix B.1.

4.3 Squared Jump and Arc Length

If material values are reconstructed simultaneously to the shape, a more complex regularization term is necessary. In this thesis, heuristic arguments are given why the jump in the material value must be penalized as well. These arguments are based on experimental results, which are shown in section 5.1. A simple idea is to multiply the arc length by the squared jump in the material value

$$\boxed{R_{SJ}(\vec{\varepsilon},\Gamma) = (\varepsilon_1 - \varepsilon_2)^2 \int_\Gamma \mathrm{d}s.} \tag{4.5}$$

As above it is assumed without loss of generality that only one level set function exists. The material values ε_1 and ε_2 are similar to chapter 3 the inner and outer permittivity. For this functional the first and second order derivatives with respect to ε_l are calculated easily. The first order derivative with respect to shape and material value is

$$\mathrm{d}R_{SJ}(\Gamma;\vec{V}_G) = (\varepsilon_1 - \varepsilon_2)^2 \int_\Gamma \kappa G \,\mathrm{d}s + 2(\delta\varepsilon_1 - \delta\varepsilon_2)(\varepsilon_1 - \varepsilon_2) \int_\Gamma \mathrm{d}s \tag{4.6}$$

with $\delta\varepsilon_l$ the change in the material value. The second order derivative yields

$$\begin{aligned}\mathrm{d}^2R_{SJ}(\Gamma;\vec{V}_F;\vec{V}_G) =& (\varepsilon_1 - \varepsilon_2)^2 \int_\Gamma \nabla_\Gamma F \cdot \nabla_\Gamma G \,\mathrm{d}s + 2(\delta\varepsilon_1 - \delta\varepsilon_2)^2 \int_\Gamma \mathrm{d}s \\ &+ 2(\delta\varepsilon_1 - \delta\varepsilon_2)(\varepsilon_1 - \varepsilon_2) \int_\Gamma \kappa(F+G) \,\mathrm{d}s.\end{aligned} \tag{4.7}$$

As mentioned above, it is of importance that the regularization term is positive definite. It is easy to see that the first and the second term in (4.7) are positive (semi-)definite. The third term, however, rises problems. For instance, the last equation yields for constant $F = G = F_c$ and $\delta\varepsilon_2 = -\delta\varepsilon_1$

$$\mathrm{d}^2 R_{SJ}(\Gamma;\vec{V}_F;\vec{V}_F) = 8(\delta\varepsilon_1)^2 \int_\Gamma \mathrm{d}s + 8(\delta\varepsilon_1)(\varepsilon_1-\varepsilon_2)\int_\Gamma \kappa F_c \,\mathrm{d}s. \tag{4.8}$$

In the last equation there exists a combination of $\delta\varepsilon_1$ and F_c such that the Hessian is negative. One idea is to modify the regularization term to assure a convex functional. Consider following inequality, which is further simplified by the Cauchy-Schwarz inequality.

$$\begin{aligned}
2\left[(\delta\varepsilon_1-\delta\varepsilon_2)\int_\Gamma \mathrm{d}s + (\varepsilon_1-\varepsilon_2)\int_\Gamma \kappa F\,\mathrm{d}s\right]^2 &\geq 0\\
2(\delta\varepsilon_1-\delta\varepsilon_2)^2\int_\Gamma \mathrm{d}s + 4(\delta\varepsilon_1-\delta\varepsilon_2)(\varepsilon_1-\varepsilon_2)\int_\Gamma \kappa F\,\mathrm{d}s + 2(\varepsilon_1-\varepsilon_2)^2\frac{\left[\int_\Gamma \kappa F\,\mathrm{d}s\right]^2}{\int_\Gamma \mathrm{d}s} &\geq 0\\
2(\delta\varepsilon_1-\delta\varepsilon_2)^2\int_\Gamma \mathrm{d}s + 4(\delta\varepsilon_1-\delta\varepsilon_2)(\varepsilon_1-\varepsilon_2)\int_\Gamma \kappa F\,\mathrm{d}s + 2(\varepsilon_1-\varepsilon_2)^2\int_\Gamma \kappa^2 F^2\,\mathrm{d}s &\geq 0
\end{aligned}$$

This result leads to following modified Hessian, which is now positive semi-definite.

$$\mathrm{d}^2 R^*_{SJ}(\Gamma;\vec{V}_F;\vec{V}_G) = \mathrm{d}^2 R_{SJ}(\Gamma;\vec{V}_F;\vec{V}_G) + 2(\varepsilon_1-\varepsilon_2)^2\int_\Gamma \kappa^2 F G\,\mathrm{d}s \tag{4.9}$$

A detailed discussion of the discretization of these integrals is given in appendix B.2. Note that the discretization of the last term in (4.9) adds positive values to the leading diagonal of the discretized Hessian matrix. This implements a small correction of the Newton direction to the steepest descent direction.

4.4 Mumford-Shah Functional and Total Variational Regularization

The Mumford-Shah functional, which has been introduced in electrical impedance tomography by Rondi [66], consists of two parts.

$$R_{MS}(\varepsilon) = \int_{\Omega\setminus\Gamma} |\nabla\varepsilon|^2\,\mathrm{d}x + \nu\int_\Gamma \mathrm{d}s \tag{4.10}$$

The first term in this equation leads to smooth images. Γ is usually called the edge set. It is removed from the domain of integration and the reconstructed permittivity can be discontinuous across the interface. The second term yields simplicity of the edge set. This term is tuned by an additional parameter ν, which is difficult to determine in practical application.

Total variation was originally introduced for image de-noising [67, 59]. A restoration algorithm, which is based on total variation, preserves edges i.e. jumps in noisy

and blurred images. This kind of regularization is well suited for inverse problems of distributed parameters. The regularization term is defined over the region of interest by

$$R_{TV}(\varepsilon) = \int_{\Omega} |\nabla \varepsilon| \, \mathrm{d}x.$$

This functional can be interpreted geometrically as the lateral surface area of ε. For piecewise constant ε it consists of the length of the boundary multiplied by the height of the jump in the material value. The length of the curves is penalized as well as the jump in the discontinuity. Both properties are held relatively small. However, the non-differentiability of the Euclidean norm at the origin rises problems in the numerical solution.

Both regularization functionals are not straight forward to implement in this work. Thus the experimental results in chapter 5 are based on the squared jump and arc length regularization.

4.5 Sensor Fusion

Electrical capacitance tomography images the spatial distribution of material permittivities. For further quantitative analysis one can calculate integral parameters, like material fractions of the process to be monitored. However, the imaging process is ill-posed and it usually strongly depends on regularization. This regularization is required to end up with acceptable results. In fact, the main problems are

- the soft-field characteristic of the electric field (ECT is known to provide information on bulk rather than on object boundaries) and
- that small disturbances near the center have almost no influence on the capacitances at the circumference of the tube.

Hence it is complicate to determine accurate volume fractions out of the tomographic image. In many applications it is reasonable to assume piecewise constant permittivities. Such situations arise e.g. in gas-liquid two-phase flows, where sharp transitions between the two phases exist. Even for shape reconstruction techniques a regularization is necessary, which incorporates specific assumptions about the material distribution, i.e. smoothness of the boundary between regions of different permittivities.

If additional information is provided, which is sensitive to object boundaries, one ends up with images that correspond better to reality than those obtained with bulk information and edge preserving regularization. Ultrasound tomography, which is sensitive to disturbance boundaries, provides this supplementary information. In this section, a concept for the fusion of Ultrasound Reflection Tomography (URT) and ECT for industrial applications is presented. The method is intended to combine the strengths of both principles while reducing their respective disadvantages.

Ultrasound Reflection Tomography. An alternative to ECT, which is as inexpensive, but is able to provide information about the shape of materials with different acoustic

impedance, is ultrasound tomography. This work focuses on Ultrasound Reflection Tomography URT due to its simplicity. It is based on Time-Of-Flight (TOF) measurements of reflected ultrasonic waves. It aims at reconstructing the acoustic reflectivity function of a cross-section of a pipe. URT has been successfully applied to industrial processes [70, 69]. One application is e.g. the identification of bubbly gas-liquid flows as described in [92]. Typically, there is a great difference between the acoustic impedance of the gas and liquid phase, resulting in a nearly perfect reflection of sound waves at phase boundaries. Gas bubbles can be treated as perfect reflectors as long as their geometrical dimensions are several times larger than the wavelength of the ultrasonic wave.

The layout of a URT system for pipelines is similar to that of the ECT sensor. Instead of electrodes, ultrasonic transducers are equally spaced around the circumference of the pipe. A sketch of an URT sensor is shown in figure 4.1. All transducers can be used as both transmitters and receivers. One transducer at a time is excited with a broadband pulse and emits an acoustic wave. This triggers the data acquisition where all transducers simultaneously act as receivers. To obtain sufficient information for the reconstruction process it is essential that the transducers have a wide beam angle in the lateral direction. On the contrary the beam should be very narrow in the azimuthal direction to treat only a thin slice of the pipe.

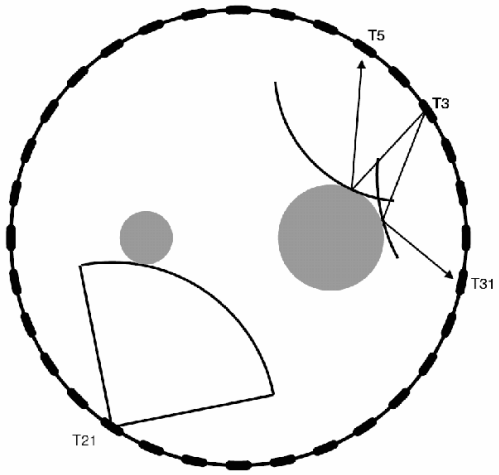

Figure 4.1: Sketch of an URT senor. The image is reconstructed by time-of-flight measurements of reflected ultrasonic waves.

The reconstruction is performed by a simple backprojection of the recorded arrival times. A pulse emitted by transducer T3 is partially reflected back to transducer T5. The backprojections take the form of ellipsoidal arcs with the foci at the transmitting and receiving transducers, respectively. The reconstruction is obtained by summing up all backprojections. At last some kind of thresholding is applied. The reconstruction does not explicitly rely on regularization but the images suffer from blurring. Figure 4.2 illustrates an URT result, which is based on the simulation of backprojections of two air bubbles in oil. To visualize the artifacts, no thresholding is applied. Many artifacts are visible especially between the two objects and this complicates the accurate determination of volume fractions.

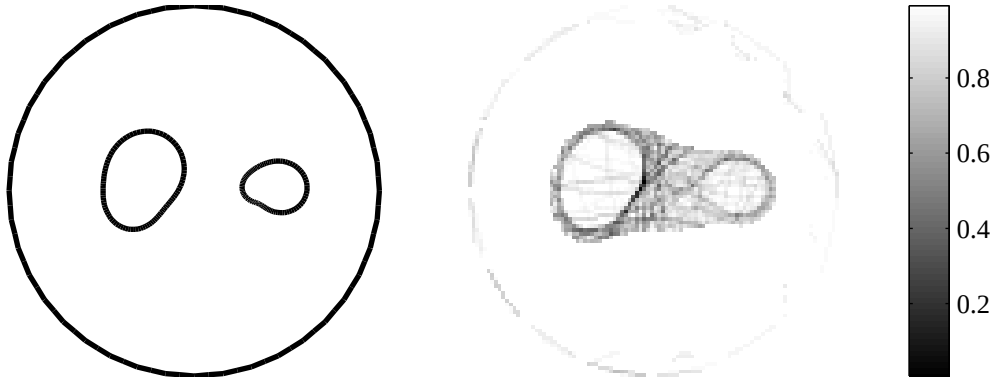

(a) Test distribution of two air bubbles in oil.

(b) URT result with simulated backprojections. The image is scaled such that possible edges have values near 0.

Figure 4.2: Example of an URT image of two air bubbles in oil.

URT offers almost opposite properties than ECT, like

- its sensitivity to the transitions between different phases and
- its sensitivity distribution, which has its maximum near the center of the pipe. This is contrary to ECT, which is sensitive at the margin of the region of interest.

A disadvantage of URT is that it can not be guaranteed that the reconstructed phase boundaries are closed contours. This may not be of major concern if one is interested in qualitative images, but seriously complicates the calculation of integral flow parameters. Additionally, it is not possible to reconstruct permittivity values of the involved materials. ECT, on the other hand, enables the quantification in terms of absolute permittivity values. The available boundary information perfectly supplements the information gathered from capacity measurements. Usually, a high number of ultrasonic transducers are used to obtain images of sufficient quality. For a sensor fusion method it is reasonable to assume that less transducers compared to a stand-alone URT system are sufficient. Sufficient means that enough information about edges is available to considerably improve the overall image quality.

Fusion of Sensor Data. Both methods have proven to be useful for monitoring industrial processes. However, they have their respective advantages and limitations and the quality of the reconstructed images is limited in practice. Each sensor system collects only incomplete data about the material distribution in the region of interest. The usage of data from both tomographic sensors is a possible remedy. The data obtained from both methods is fused to yield better overall reconstruction results. ECT benefits from

- the supplementation of the soft field properties of the electric field and
- the introduction of a physically meaningful regularization.

URT takes advantage of the fact

- that the fusion yields closed contours and
- that material values of the distinct regions are determined.

An obvious way to implement the data fusion is a sequential coupling of information. The URT image is obtained first and it provides a prior information for ECT. Level set methods are a versatile tool for image processing, e.g. they are used for the segmentation of images. One idea is to perform such segmentation of the URT image simultaneously to the ECT reconstruction. Therefore the fusion between URT and ECT is based on the common level set method. This procedure is described in detail in the following subsection. Another possibility is explained in the second subsection. It is based on post-processing of the ECT and URT image by level sets. This method is not based on boundary elements. However, it is an illustrative example for the fusion of different sensor data. Both methods are validated by simulated experiments. A further discussion can be found in [10, 11].

For the sake of simplicity, it is assumed that the cross-sectional material distribution does not change between the ECT and the URT measurements (e.g. if ECT and URT sensors are in the same plane in flow direction). Otherwise one must take effects of fluid dynamics into account. For instance a statistical inversion with a state space formulation and an appropriate transition matrix can be performed in this case.

4.5.1 Segmentation of the URT Image and ECT Reconstruction

One idea for the segmentation of images is to use a deformable (active) contour. The curve is driven by an appropriate velocity function where the propagation is stopped at edges. A possible velocity function is given by (see e.g. [59])

$$F = -\nabla(g\vec{n})\,. \tag{4.11}$$

In (4.11), $\vec{n}$ is the normal vector of the interface and $g : \mathbb{R}^2 \to \mathbb{R}$ is an edge detector, which is chosen in such a way that $g = 0$ at ideal edges of the image and $g > 0$ elsewhere. The image obtained by URT contains information about edges and contours of objects. Therefore an edge detector is not necessary and g equals the intensity values of the URT image scaled to the range from 0 to 1 (as shown in figure 4.2(b)).

The velocity function (4.11) can be interpreted as the negative gradient direction for the cost functional

$$\boxed{R_{IS}(\Gamma) = \int_\Gamma g \,\mathrm{ds}.} \tag{4.12}$$

If the problem satisfies the necessary smoothness requirements, a shape sensitivity analysis can be performed. One obtains the first and second order derivatives (2.43) and (2.61). In [35], Hintermüller and Ring propose a second order approach for image segmentation based on (4.12). They observe that the shape Hessian is likely to be positive definite near

the optimal contour. This property must be maintained for contours away from the optimal contour. Hintermüller and Ring suggest following modification of the shape Hessian

$$\mathrm{d}^2 R_{IS}(\Gamma;\vec{V}_F;\vec{V}_G) = \int_\Gamma \left[\left(\frac{\partial^2 g}{\partial n^2} + 2\frac{\partial g}{\partial n}\kappa \right)^+ FG + g\nabla_\Gamma F \cdot \nabla_\Gamma G \right] \mathrm{d}s,$$

where $(\cdot)^+ = \max(\cdot, \sigma)$ for $0 \leq \sigma \ll 1$. The non convex part is cut off if $\delta = 0$. If $\delta > 0$, a small correction towards the steepest descent direction is realized.

The cost functional for the image segmentation method is similar to the regularization term in ECT. Obviously, a possible technique for sensor fusion is to incorporate the segmentation of the URT image as a regularization term for the capacitance tomography. Instead of using the conventional smoothness assumption on the active contour, the regularization term R_{IS} attracts the contour towards edges. The numerical discretization of (4.13) is performed similar as described in appendix B.

A test distribution is used to compare the ECT reconstruction with and without edge information from the URT. The true material distribution consists of two air bubbles ($\varepsilon_1 = 1$) in oil ($\varepsilon_2 = 2$) as shown in figure 4.2(a). The measured voltages are simulated by the boundary element method and a Gaussian distributed measurement noise with a standard deviation of 0.1 percent of the sending voltage is assumed. Figure 4.3(a) presents the result of the capacitance tomography. The shape of the two bubbles does not match the true distribution. By incorporating information from URT, which is shown in figure 4.2(b), the reconstruction can be improved significantly. This is illustrated in figure 4.3(b)) where the phase boundaries are reconstructed very well.

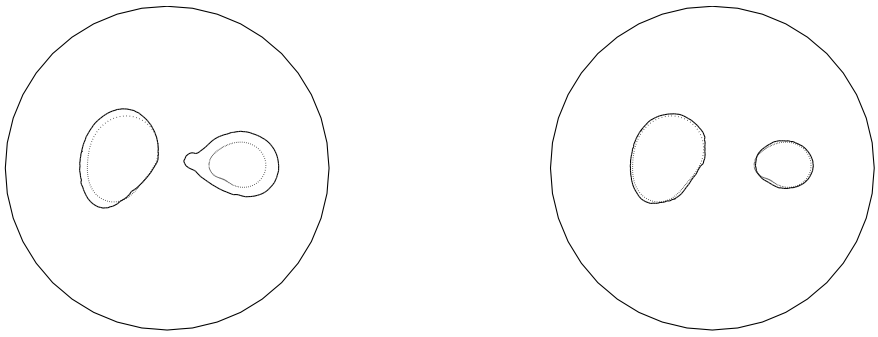

(a) BEM and level set based reconstruction without particular prior information.

(b) Reconstruction with edge information from URT.

Figure 4.3: Sensor fusion based on a physically meaningful regularization term. The accuracy of the reconstructed shape is improved significantly by prior information from URT (dotted line: test distribution, solid line: reconstructed shape).

4.5.2 Post-Processing of ECT and URT Images

Another possibility to combine both tomographic techniques is to post-process the obtained images. For this method the ECT reconstruction is performed by a discretization

into finite elements with constant permittivity values as described in [8]. The next step is a segmentation into distinct regions. Therefore information about the permittivity values from ECT and about edges from URT are processed into one combined image. In this essay a two-phase flow is assumed and only a set with two permittivity values is used for two or more disjoint regions. The piecewise constant material values are expressed by

$$\varepsilon = \varepsilon_1(1 - H(\Phi)) + \varepsilon_2 H(\Phi) \tag{4.13}$$

similar to the multiphase level set method (section 2.1.3). The two material values ε_1 and ε_2 are calculated as the mean permittivities in each region. The ECT image is denoted by ε^* and its segmentation is done by minimization of the following cost functional, which has been introduced in [19]

$$J_{IS,1} = \int_\Omega |\varepsilon - \varepsilon^*|^2 \, \mathrm{d}x. \tag{4.14}$$

Both image segmentation techniques can be combined into one cost functional by a weighting parameter α^2, which scales the URT term.

$$J_{IS} = \int_\Omega |\varepsilon - \varepsilon^*|^2 \, \mathrm{d}x + \alpha^2 \int_\Gamma g \, \mathrm{d}s \tag{4.15}$$

The fist order accurate velocity function for that functional is calculated by

$$F = -(\varepsilon_1 - \varepsilon^*)^2 + (\varepsilon_2 - \varepsilon^*)^2 - \alpha^2 \left(\frac{\partial g}{\partial n} + \kappa g \right). \tag{4.16}$$

The weighting parameter α^2 adjusts the confidence in the URT image and the ECT image, respectively. An example is shown in figure 4.4. First the ECT image ε^* is presented. Note that a somehow arbitrary threshold value is necessary to separate both phases in this image. Figure 4.4(b) presents the reconstructed shape with the image segmentation by (4.15). The shape is determined accurately (the URT image attracts the contour to the correct interface) and the mean permittivities of each region are obtained automatically. This simple method combines the strength of both imaging techniques. It operates on basis of the individual images and no modification of the reconstruction software is necessary.

4.6 Constraints on Material Value and Geometry

Another kind of a priori information is the restriction of the parameter space to feasible solutions. In case of ECT, constraints are imposed on the material value and on the geometry. To calculate the Newton type descent direction, one has to solve

$$(\mathbf{G}_1 + \alpha^2 \mathbf{G}_2)\vec{\delta}^k = -(\vec{g}_1 + \alpha^2 \vec{g}_2) \tag{4.17}$$

for iteration k, where the change in geometry and permittivity is summarized into

$$\vec{\delta}^k = \begin{pmatrix} \vec{F} \\ \vec{\delta\varepsilon} \end{pmatrix}. \tag{4.18}$$

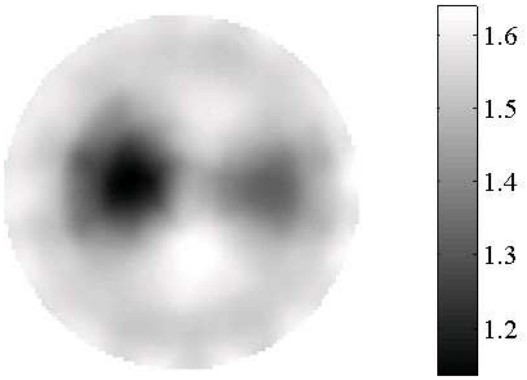

(a) ECT result based on a FEM grid. For the liquid phase $\varepsilon_r = 2$.

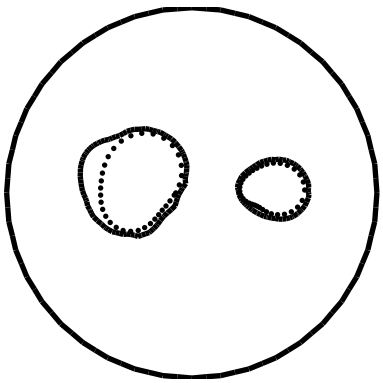

(b) Image segmentation. The combination of the URT and FEM image yields a good agreement of the shape (dotted line: test distribution, solid line: reconstructed shape).

Figure 4.4: Sensor fusion technique based on an image segmentation.

The gradient and Hessian for the first term of the cost functional (1.8) are calculated by (3.38) and (3.39), respectively. For the second term, the discrete derivatives are defined in (B.13).

In fact, the minimization problem is extended by the inequality

$$\varepsilon_l \geq 1 \qquad \forall l, \tag{4.19}$$

which constrains the relative permittivities of all distinct regions to values above one. Additionally, the reconstructed interface must be in the interior of the pipe. Thus, the pipe wall is an upper bound for the velocity F. In the negative direction (a contraction of the region), F is limited to the so called skeleton of the shape. Figure 4.5 illustrates these limits for F, which are calculated on each node point of the discrete boundary element mesh. The dashed line indicates the skeleton of the shape. Points on the skeleton are equidistant to both sides of the contour. The limit is found by a line search, which looks for the first minimum of the level set function in the direction of the inward normal vector.[1] This restriction is incorporated by the inequality

$$\vec{F}_{min} \leq \vec{F} \leq \vec{F}_{max}, \tag{4.20}$$

which must be fulfilled for each value of the velocity function.

The whole optimization process is solved by a Sequential Quadratic Programming (SQP) technique (see e.g. [29]). In each iteration step the objective function is replaced by a quadratic approximation. The Newton step is calculated by an active set method, which includes the linear constraint functions. The convergence properties of the SQP algorithm are improved by using a line search, which adjusts the step size. Implementation details about the optimization techniques can be found in [29, 33].

[1] Figure 2.1 illustrates the one dimensional level set function. The point, which minimizes Φ, is equidistant from the interface points.

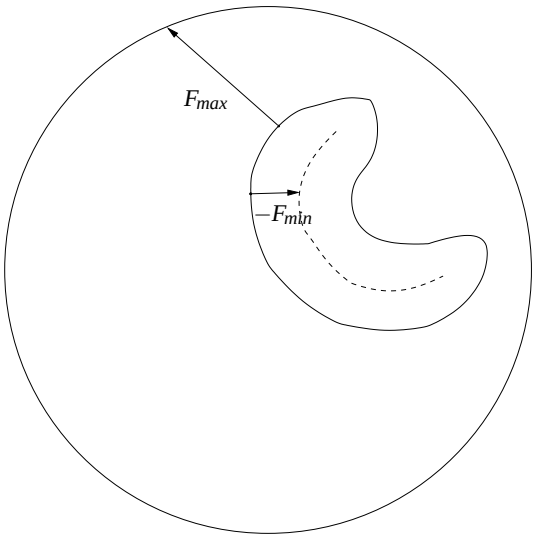

Figure 4.5: Geometrical constraints on the velocity function. The maximum value for $\vec{F}$ is the distance in normal direction to the pipe circumference. In the interior, the skeleton (dashed line) is the lower limit of the velocity. These distances are calculated for each node point and they act as an upper and lower bound for the optimization problem.

Concluding Remarks. In the previous two chapters, the objective function (1.8) is discussed in detail. The adjoint variable method is utilized to calculate the sensitivity of the electric field problem with respect to the deformation of the interface and the change in material values. Appropriate regularization terms are presented in chapter 4 and the calculation of the sensitivity of these terms is performed. At this point the reconstruction problem can be solved efficiently by the optimization technique SQP. The following chapter demonstrates the suggested reconstruction method by real world measurement data.

Chapter 5

Experimental Results and Discussion

This chapter validates the proposed reconstruction algorithm by experiments with real world measurement data. The images obtained by ECT are influenced by plenty of different factors, such as

- calibration of the measurement system and the BEM model,
- discretization of the forward problem,
- parameter space (unknown shape or unknown shape and material properties),
- regularization term,
- choice of the regularization parameter,
- measurement noise, and
- initial condition.

To measure the influence of these parameters on the reconstruction one has to examine the quality of the obtained images. In this work following criteria are evaluated

- surface area, which is measured in percent of the true area,
- material values of the reconstructed phases,
- stability under real world measurement noise, and
- stability with respect to the initial condition.

The next paragraphs depict the measurement setup and define two test distributions, which are used to examine the proposed shape optimization. Additionally, the calibration procedure of the computer model is discussed and details about the implementation are given. Especially, the necessary computational steps are summarized in a list.

Then two sections deal with the two different types of parameter spaces. First only an unknown shape is considered. Therefore it is assumed that the material values are known

a priori. The penalization of the arc length is used as regularization term. Mainly, two issues are analyzed, namely the influence of the regularization parameter and the influence if the assumed material values are altered. Additionally, the Newton-type optimization is compared with the gradient descent and the influence of the spatial discretization of the level set function is demonstrated. Second the parameter space is enlarged. Not only the shape but also the material values are reconstructed. As above the regularization parameter is an important issue. Further it is an essential attribute of a reconstruction technique to deliver stable results with respect to measurement noise. Therefore the influence of measurement noise on the result is analyzed. The initial condition (alteration of material value and geometry) could probably have some influence on the obtained image as well. Finally, a few limitations of the implementation of the imaging technique are shown. The last section gives a final discussion and conclusion.

Measurement Setup. The measurement setup consists of the charge based sensor (as described in the introduction of this work). The pipe diameter is 10.3 centimeters and it contains different materials in its interior. In this work following test materials are used for the measurement, namely

- PVC objects of different shapes (circles, semicircles),
- fill levels of different phases (tap water, diesel), and
- bubbles of air in water.

The materials are fixed for the measurement and they do not change in longitudinal direction. A set of 160 measurements is recorded for one material distribution whereas each measurement consists of 120 measured displacement currents. The data acquisition time for the measurement of 120 displacement currents, which are the necessary data for the reconstruction of one image, is less than 60ms. The covariance matrix is estimated and no averaging is performed for the reconstruction process.

First two test distributions are presented in figure 5.1(a) and figure 5.1(b). One distribution (measurement setup *A*) consists of two objects with a shape of a circle and a semicircle. Test distribution *B* consists of three equally shaped PVC rods. The diameter of the PVC rods is 20.9 mm and their surface area is $3.43\,\mathrm{cm}^2$. The semicircle shaped object has an area of $9.01\,\mathrm{cm}^2$. Figure 5.1(c) and figure 5.1(d) demonstrate the reconstruction result with a FEM based algorithm. The interior region is discretized into 316 triangles, whose permittivity values are the degrees of freedom. The results are quite blurred and it is difficult to estimate e.g. volume fractions out of these images.

The quality of the measurement hardware is defined by the Signal to Noise Ratio (SNR), which is calculated by the proportion of the measured displacement current to its standard deviation. Figure 5.2 illustrates the SNR for the setup *A* for all 120 displacement currents. The SNR is not evenly distributed because it depends on the operating point of the amplifier in the sensor frontend. The SNR is in the range between 32 and 52 dB. Further information about the utilized sensor hardware can be found in [89]. The influence of the measurement noise on the reconstructed image is discussed later in section 5.2.1.

(a) Measurement setup *A*: two PVC objects.

(b) Measurement setup *B*: three PVC rods.

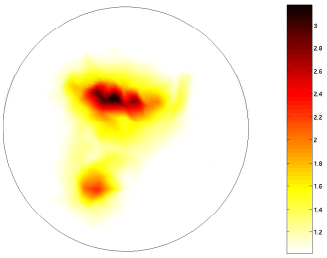

(c) Reconstruction with a FEM based algorithm.

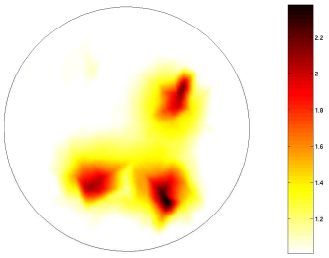

(d) Reconstruction with a FEM based algorithm.

Figure 5.1: Two test distributions to verify the reconstruction algorithm. The reconstructions are performed by a fixed discretization into finite elements.

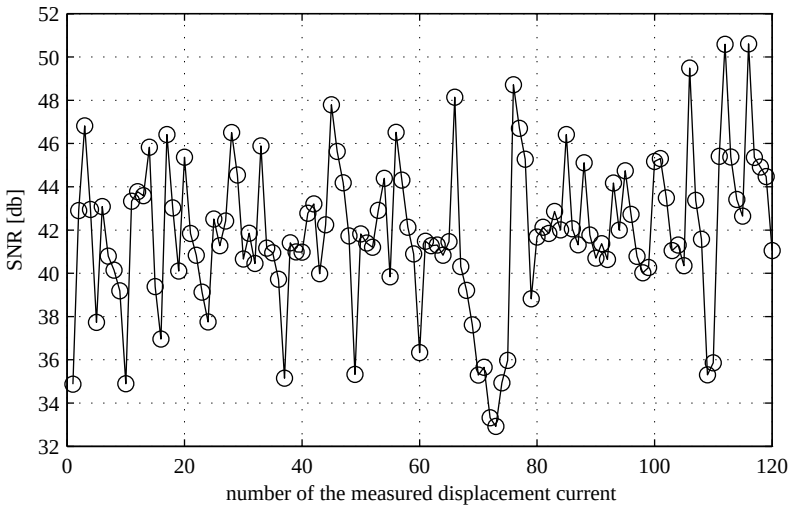

Figure 5.2: Signal to noise ratio of the measured displacement currents for setup *A*.

Calibration of the Boundary Element Model. An accurate calibration is essential for a successful reconstruction. A detailed description of the calibration of the sensor front-ends can be found in [89]. Generally, a characteristic curve is used to map values from the Analog to Digital Converter (ADC) to displacement currents. These displacement currents correspond to charges in the two dimensional computer model.

To calibrate the ECT system it is necessary to obtain a specific set of data i.e. one has to physically fill the sensor with low permittivity material and consecutively with a sample of a high permittivity material. Then geometrical properties of the BEM mesh and permittivity values are altered such that a conformity between measured and calculated capacitances is obtained. In this work, the calibration is based on two measurements. First the sensor is filled with air, then it is filled with tap water.

Figure 5.3 and figure 5.4 show the measured displacement currents. The electrodes are numbered consecutively from the one, which is adjacent to the exciting electrode, to the electrode, which is located opposite the exciting one. The first measurement in figure 5.3 is used as a reference. This is necessary because the exciting voltage is not known exactly. Both figures show a decrease in the measured displacement currents, whereas the setup with water has a smaller measurement range than the setup with air. Due to simplifications (e.g. the 3D to 2D simplification, compare with section 1.1), there exists a discrepancy between the sensor and the corresponding computer model. Thus parameters in the BEM mesh are altered such that the measured decrease matches the decrease in the calculated charges. In this work the distance of the radial screen and the permittivity values of the PVC and of the space between the pipe and the grounded screen are adjusted. The differences between measured and calculated values are shown in the second subfigure in figure 5.3 and figure 5.4 respectively. The conformity between sensor and model is satisfying.

The idea of normalized capacitances is used to map the measured displacement currents to charges in the boundary element model. Generally, the displacement currents are normalized between the currents of the low permittivity material i_l and that of the high permittivity material i_h.

$$i^* = \frac{i_{meas} - i_l}{i_h - i_l} \tag{5.1}$$

where i^* is the normalized current and i_{meas} is the actually measured one. The charges in the model, which are used for the reconstruction of an image, are calculated by linear interpolation between the charges of the low permittivity material q_l and that of the high permittivity material q_h, respectively.

$$q^* = q_l(1 - i^*) + q_h i^* \tag{5.2}$$

where q^* is the calibrated data for the reconstruction process.

Implementation Details. The discretized sensor model (figure 3.2) consists of 876 boundary elements and 860 node points. The discretization of the interior objects depends on the fixed grid of the level set function. The level set function in this work is defined on a uniform grid with a grid space of two millimeters. The number of boundary elements of the interior objects depends on the arc length of their contour.

The input parameters of the algorithm are the measurement data, the estimated covariance matrix, and the regularization parameter. The regularization parameter, which is chosen empirically, is constant during the optimization process. Not the determination of the parameter itself is discussed but its influence on the reconstruction result. At the beginning of the reconstruction process one has to define the initial condition, which is

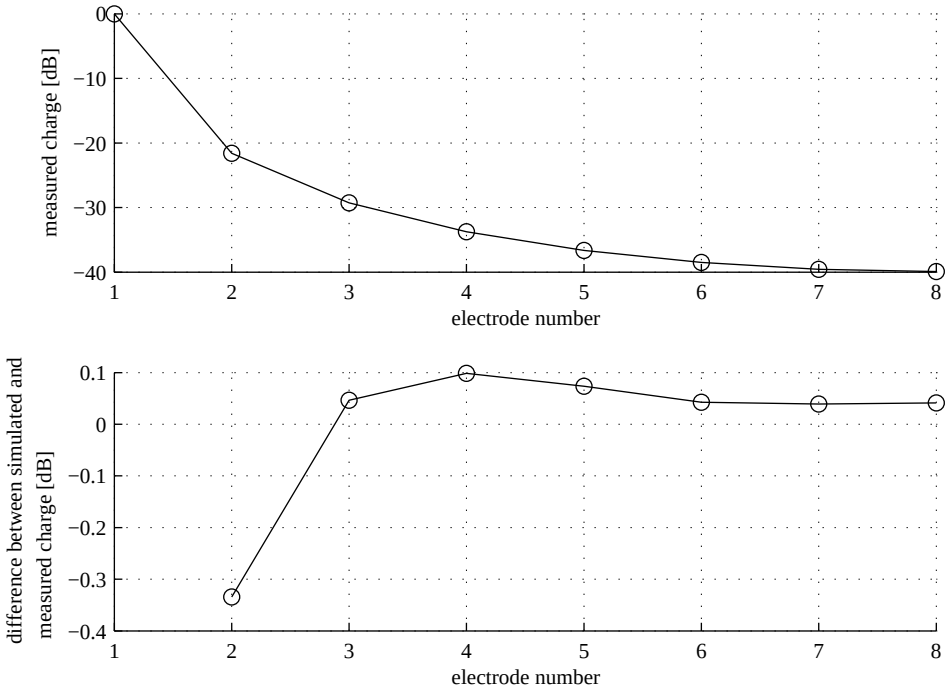

Figure 5.3: Decrease in the measured charges and their differences compared to the calculated ones for an empty sensor. The first electrode, which is located adjacent to the exciting one, is used as a reference electrode. The other electrodes are numbered consecutively (the last electrode is located opposite the exciting one).

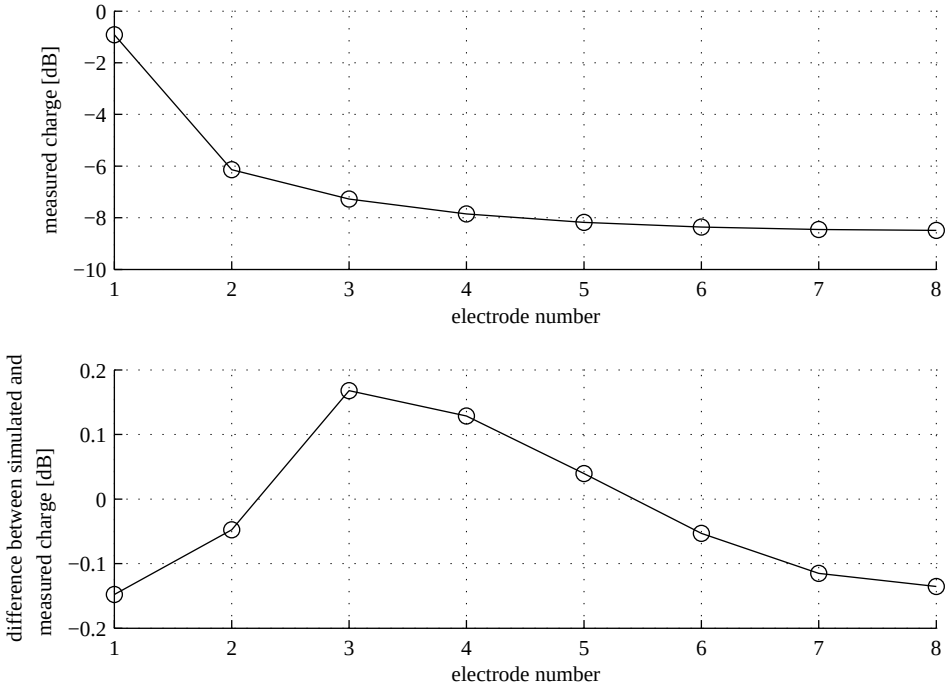

Figure 5.4: Measured charges for a sensor filled with tap water and their differences compared to the calculated ones.

determined by the geometry and by the material values of the objects. The advantage of the level set formulation is its flexibility. Thus the correct topology of the objects to be reconstructed has not necessarily to be available at the beginning. Tests have shown that a reasonable initial condition for the geometry is an object with the shape of a circle in the center of the pipe.

The reconstruction is summarized by following steps, which are evaluated iteratively:

1. track the boundary, assemble the node points to boundary elements, and find the region number of each object,
2. solve the field problems and calculate all necessary forward and adjoint problems by the superposition principle,
3. calculate the objective function, which consists of the least error squares and of the regularization term,
4. solve the boundary integrals to calculate the Jacobian (for the least error squares) and the gradient and the Hessian (for the regularization term),
5. calculate the search direction and consider the physical constraints by the active set method,
6. extend the velocity off the interface (velocity extension)
7. update the level set function and update the permittivity values,
8. reinitialize the level set function (reinitialization) and continue with step one.

Additionally to these points, a line search is performed to adjust the step size. This achieves an improvement of the convergence of the optimization algorithm. This convergence is measured by the decrease in the objective function. The algorithm is stopped, if this decrease is less than a certain constant. Another stopping condition is a small change in the unknown parameters. In other words the algorithm is terminated if the maximum absolute velocity value is less than a constant. This constant depends on the spatial discretization of the level set function. A similar condition is applied for the change in the material values.

5.1 Unknown Shape

At the moment only an unknown shape (and not unknown material values) is considered. The test distribution *A* in figure 5.1(a) is used for the reconstruction process. The first 9 iterations are shown in figure 5.5. As an initial condition, an object with the shape of a circle is used, which is located at the center of the region of interest and its diameter is 4 cm. The permittivity of the object is two ($\varepsilon_1 = 2$) and the background has a permittivity $\varepsilon_2 = 1$.

After only four iterations one can recognize the outline of the two objects. At iteration step six the shape divides into two parts. Each part is further described by its own level

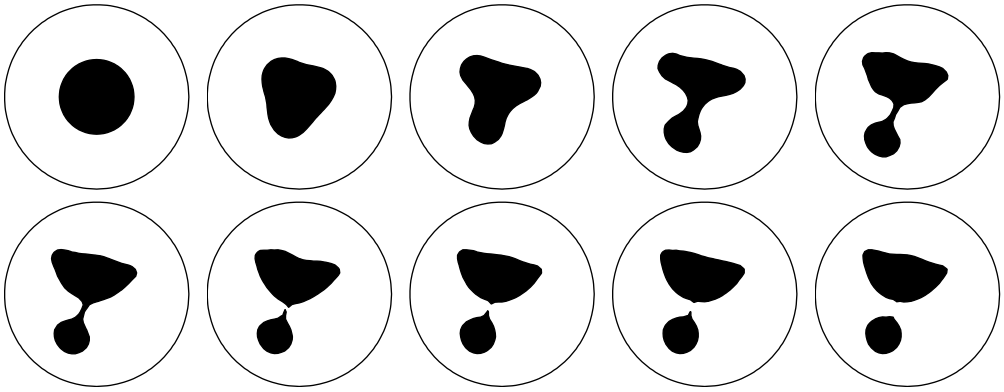

Figure 5.5: Iteratively deformed shape based on real world measurement data. The material values are constant during the deformation.

set function. The decrease in the objective function is plotted in figure 5.6. A good convergence behavior is obtained and the objective function is monotonously decreasing. The resulting surface area after convergence differs from the real area of the objects by only 1.7 percent.

The regularization parameter in this example, which is chosen empirically, is $\alpha^2 = 10^{-3.25}$. This parameter is constant for all iterations. One idea for a deterministic choice is the L-curve criterion, which is introduced in [34]. Figure 5.7 presents the L-curve for this example. One tunes the regularization parameter and the regularization term (second term of the objective function) is plotted against the least error squares (first term) in a logarithmic scale. The idea of the L-curve is to chose the α^2, which is located at the corner of the curve (at the point of maximum curvature). The figure demonstrates that a reasonable value of the regularization parameter can be found by this criterion.

Comparison between Steepest Descent and Newton-type Optimization. The minimization of the objective function is done by a Newton-type velocity function. As it is mentioned in the introduction a second order approach is superior to a gradient flow.

Figure 5.8 compares the decrease in the objective function of both possible optimization techniques. First the reconstruction is performed by the proposed Newton-type flow. Convergence is achieved after 13 iteration steps. The second curve corresponds to the flow in the steepest descent direction. An overall number of 83 iterations are necessary until a sufficient solution is reached. Between iteration step 25 and 53 one obtains only few decrease of the objective function. Until iteration step 53 only one object exists. At this point of the reconstruction the object splits into two parts.

Spatial Discretization of the Level Set Function. Figure 5.9 presents reconstructed contours whereas the grid space of the level set function is altered. Each node point of the boundary element mesh is marked by a dot. The resulting interfaces depend on the level of discretization. For a very coarse mesh (grid lines every 8 mm and 10 mm) the object does not split into two. However, the results of the last two discretization levels hardly differ. All further tests in this thesis are computed by a grid space of two millimeters.

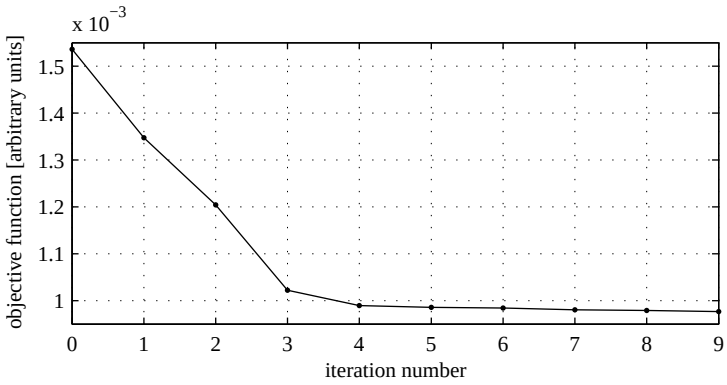

Figure 5.6: Convergence of the shape optimization problem. The objective function is plotted against the iteration numbers.

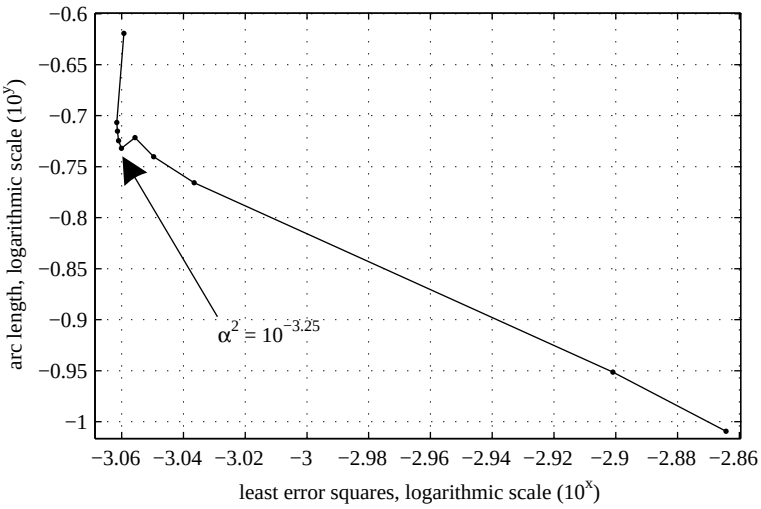

Figure 5.7: L-curve of the shape optimization problem. The least error squares are plotted against the regularization term for different regularization parameters.

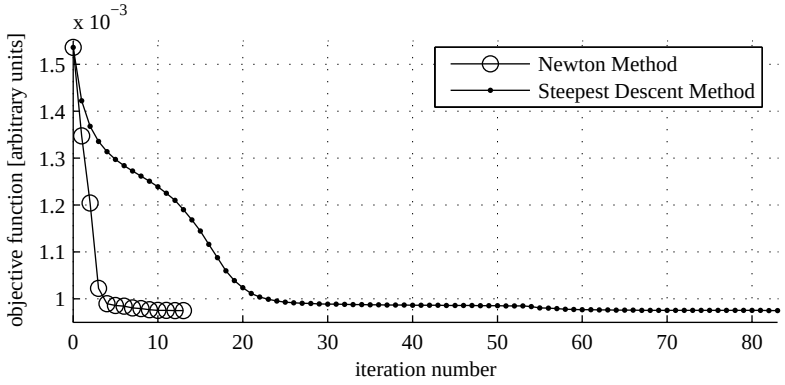

Figure 5.8: Comparison between steepest descent and Newton method.

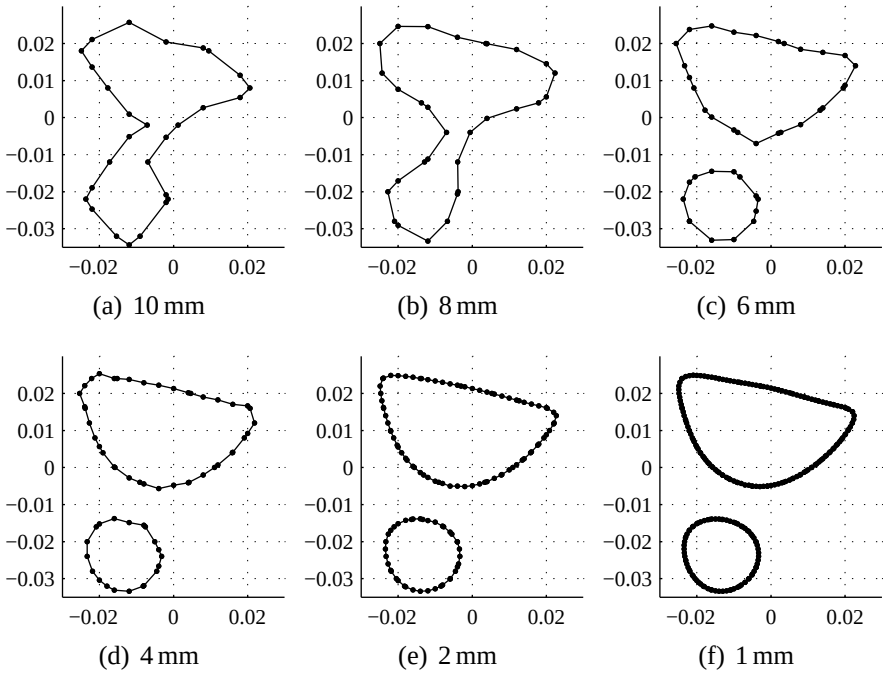

Figure 5.9: Reconstructed contours for different grid spaces of the level set function.

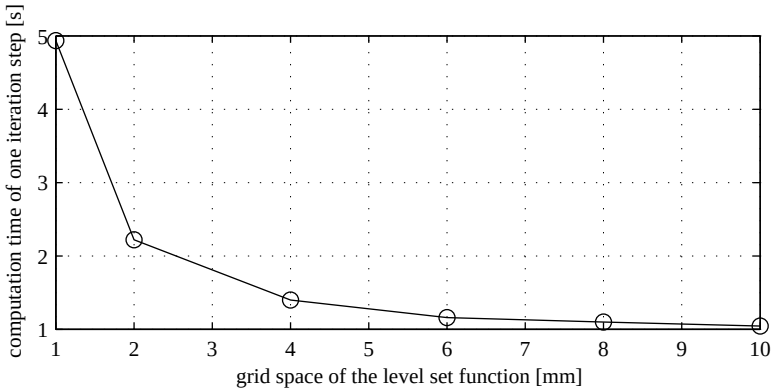

Figure 5.10: Computational effort of the first iteration step for different levels of discretization of the level set function.

The computing time of the level set framework is about 20 percent of the time, which is necessary for the boundary element method. In figure 5.10 the overall computation time of the first iteration step is plotted against the different levels of discretization of the level set function. Depending on the application one has to find a tradeoff between accuracy of the contour and computational time.

Correlation between Material Value and Reconstructed Shape. One important issue is the influence of the regularization parameter on the obtained image. Additionally, an alteration of the permittivity value of the interior object (ε_1) could probably change the reconstruction result. In figure 5.11 the regularization parameter and the permittivity

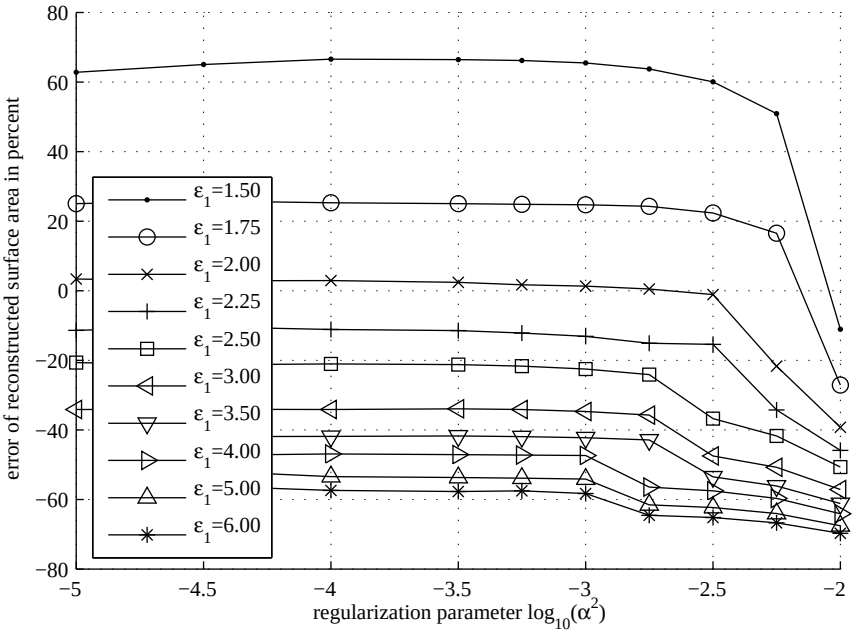

Figure 5.11: The relative error between the reconstructed and true surface area for different material values and regularization parameters.

value are varied and the obtained image quality is measured by the reconstructed surface area of the interior object. The surface area is measured in percent of the true area of the objects. The initial condition for this test remains the same as described above.

One can observe that the permittivity has a very strong influence on the reconstructed areas. A smaller permittivity value leads to an oversized surface area and vice versa. A possible interpretation of this impact is that an object with large area and a small permittivity value has a similar effect on the least squares than an object with high permittivity and small surface area.

An interesting fact, which is shown in this figure, is that less influence exists between regularization term and surface area for a wide range of regularization parameters. On the right hand side, which corresponds to strong regularization, the reconstructed area is too small. In this case the arc length of the contour is penalized too much such that the object can not split into two regions and the reconstruction fails. However, for values less than 10^{-3} the surface area is nearly constant.

There is a correlation between permittivity value and reconstructed surface area. This is an important issue if the permittivity value is not known a priori. Carefulness is necessary if the reconstruction of the shape and material values are performed simultaneously. A penalization of the arc length without a penalization of the jump in the material values leads to erroneously high permittivity values. In this case the reconstruction compensates a too small surface area by a disproportional high permittivity value.

5.2 Unknown Shape and Material Value

The results in this section are based on the regularization, which penalizes the squared jump in the material value across the interface multiplied by the arc length of the contour. This type of regularization is described in section 4.3.

Figure 5.12 presents the first iterations of the shape and material reconstruction of the measurement setup *A* whereas the regularization parameter is constant and $\alpha^2 = 10^{-3.75}$. For this test the same initial condition is used as above. At iteration step six the level set function splits (similar to the shape reconstruction) into two fragments. At this point two objects exist, each of them with its own material value in the subsequent iterations. The convergence behavior is shown in figure 5.13. A monotone decrease in the objective function is presented. Figure 5.14 illustrates the change in the material values. From iteration one to iteration six only two material values exist. Then each object (the circle and the semicircle) has its own permittivity.

The image at convergence is shown in figure 5.15(b). The reconstructed mean permittivity value [1] is $\varepsilon = 2.09$. The surface area is 2.2 percent less than the true shape.

Figure 5.15 presents results for different regularization parameters. The object does not split into two if the regularization parameter is too high. In this case the permittivity value is too low. Similar results are obtained for the test distribution *B* (shown in figure 5.16). For a small regularization parameter all three PVC rods are reconstructed. However, more artifacts are visible. The reconstructed surface area in figure 5.16(b) differs 5.4 percent from the true shape and the average permittivity value is $\varepsilon = 2.07$.

Influence of the Regularization Parameter. A deterministic approach for the choice of the regularization parameter is e.g. the L-curve. This curve is shown for the test distribution *A* in figure 5.17. Values for α^2, which are used above to demonstrate the results, are marked. The curvature can be used to identify a reasonable parameter. However, in this plot a corner can hardly be identified. The regularization parameter has a strong influence on the resulting image.

Figure 5.18 and figure 5.19 analyze the influence on the permittivity value and on the reconstructed surface area for the first and second test distribution, respectively. The regularization parameter works as tuning parameter. In both plots a strong correlation between the permittivity value and the area of the objects can be identified. The dependency between both attributes is shown in figure 5.20. Additionally, it is compared to the dependency in the shape reconstruction (figure 5.11). For the shape and material reconstruction the regularization parameter is altered, whereas this parameter is fixed for the shape reconstruction. In this case $\alpha^2 = 10^{-3.25}$ and the permittivity value is altered. Both curves are nearly identical. This leads to the conclusion that this behavior is an essential attribute of this kind of inverse problem. Even though the shape of the object can be identified, it is difficult to estimate correct volume fractions out of the tomographic images. A possible solution could be to apply further information about the permittivities or shapes of the objects to be reconstructed.

[1] A weighted average is used whereas each permittivity value is multiplied by the fraction of its surface area.

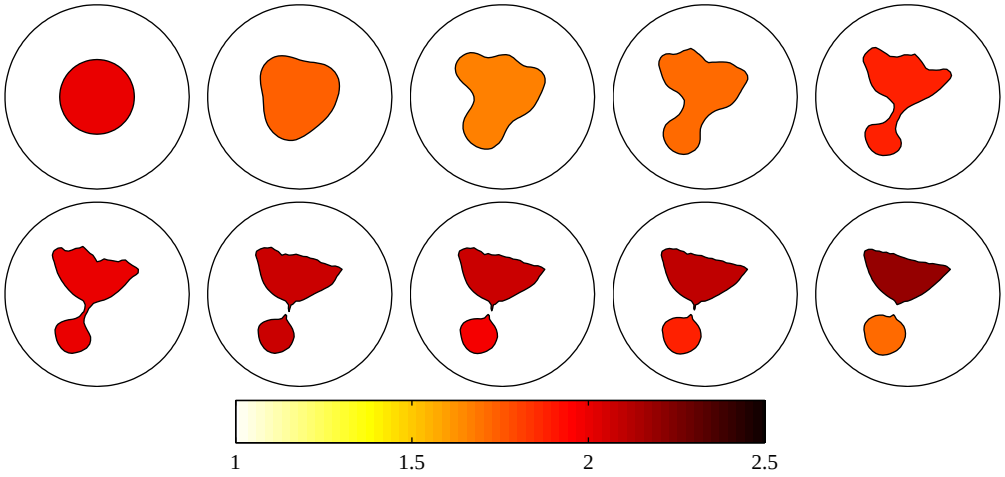

Figure 5.12: Reconstruction of the shape simultaneously to the material values. The first 9 iteration steps are shown.

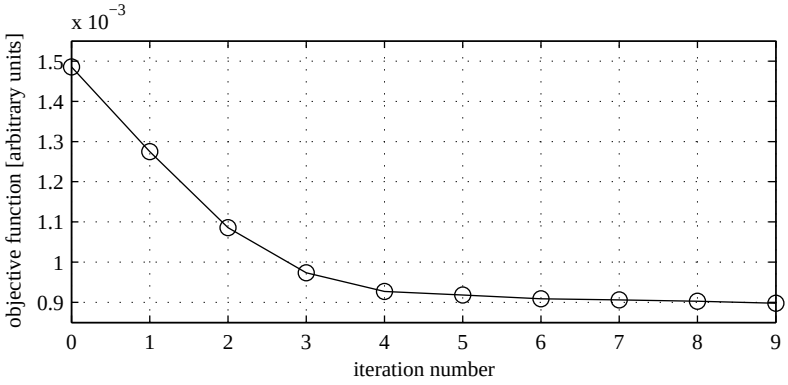

Figure 5.13: Convergence of the reconstruction problem.

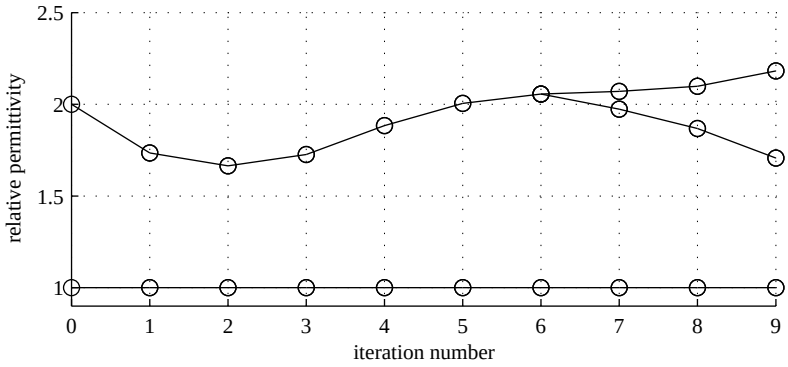

Figure 5.14: Material values of each reconstructed region. At iteration step six the shape splits into two objects. In the subsequent iterations each object is described by a distinct permittivity value.

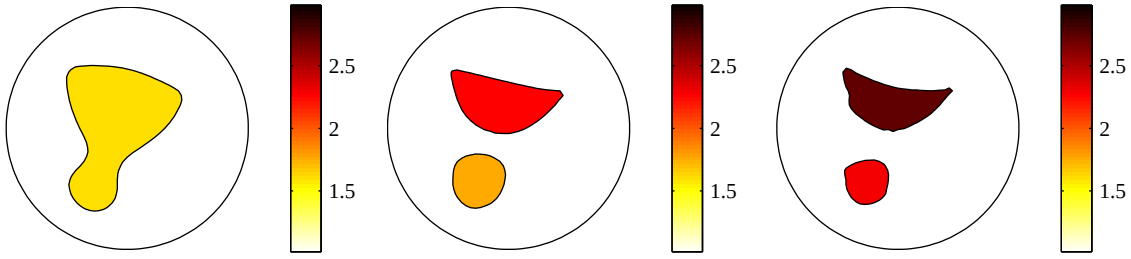

(a) $\alpha^2 = 10^{-3}$ (b) $\alpha^2 = 10^{-3.75}$ (c) $\alpha^2 = 10^{-4.5}$

Figure 5.15: Influence of the regularization parameter on the reconstructed shape.

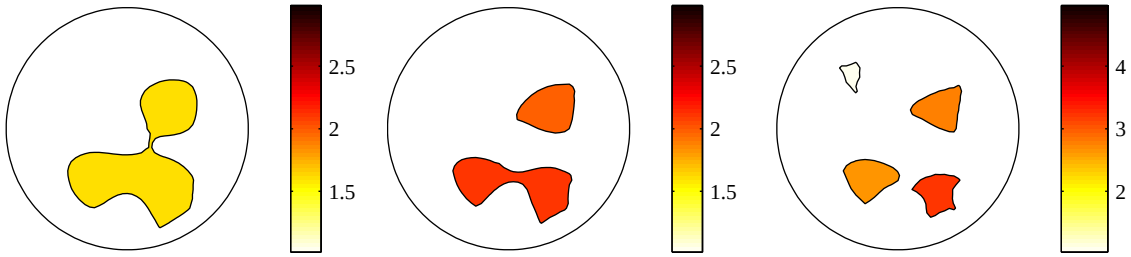

(a) $\alpha^2 = 10^{-3.25}$ (b) $\alpha^2 = 10^{-4}$ (c) $\alpha^2 = 10^{-4.75}$

Figure 5.16: Reconstruction results for the test distribution *A*.

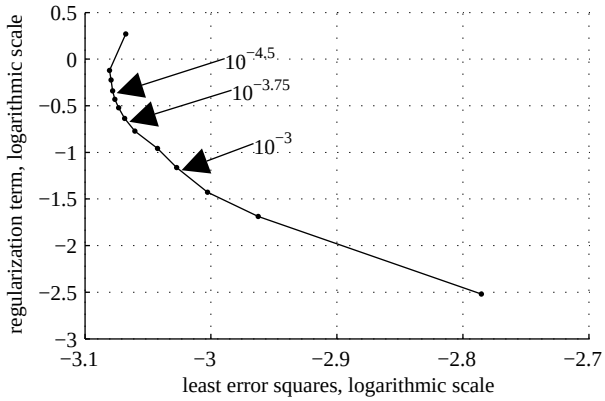

Figure 5.17: L-curve of the shape and material reconstruction for test distribution *A*.

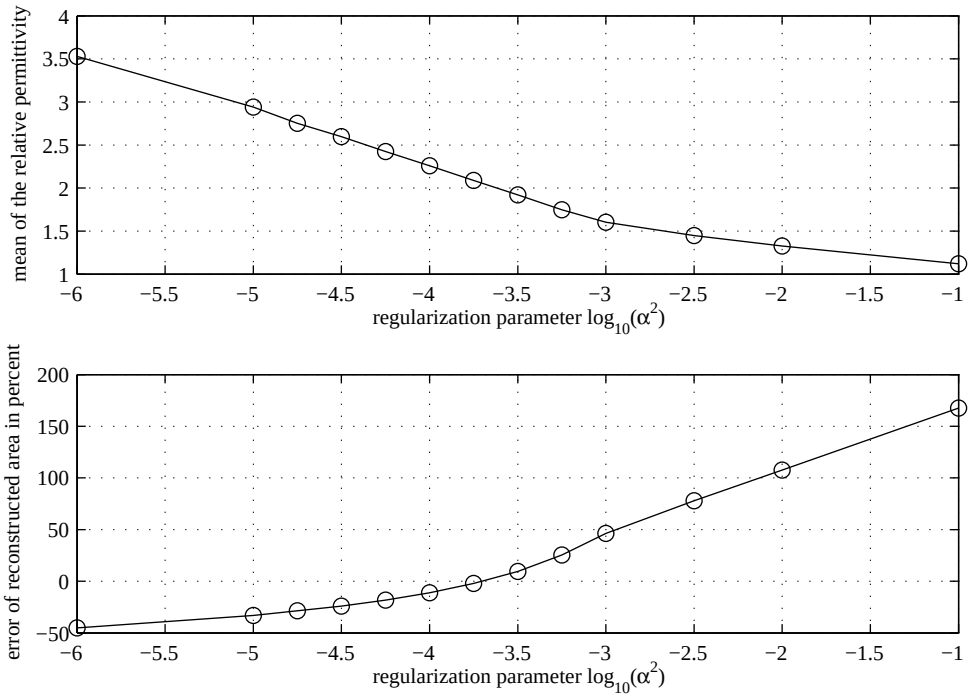

Figure 5.18: Reconstructed material value and surface area (error in percent) for different regularization parameters for the test distribution *A*.

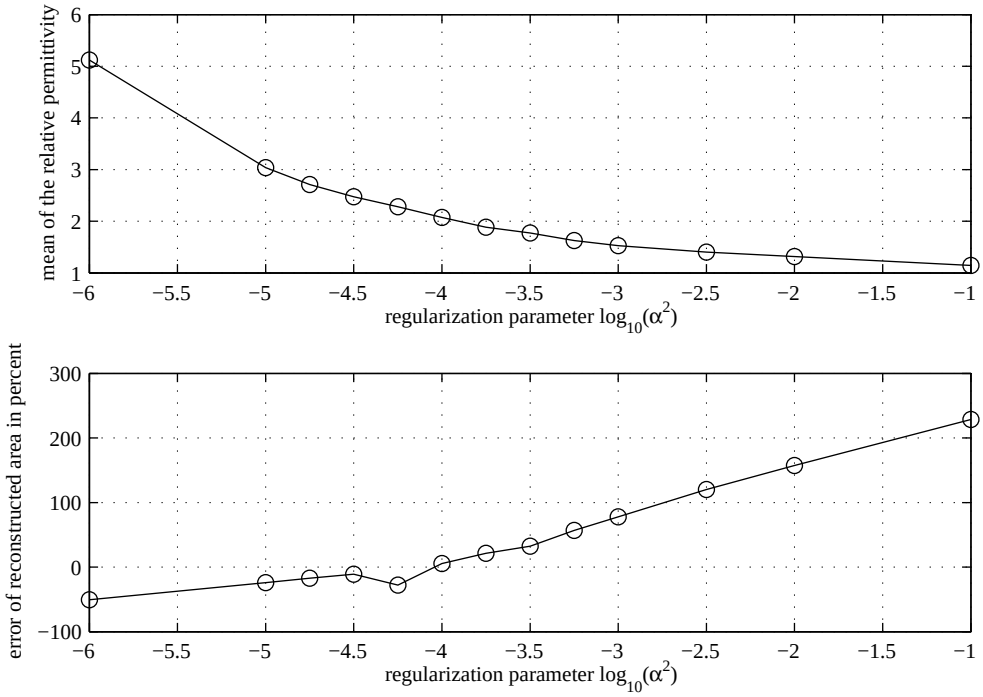

Figure 5.19: Reconstructed material value and surface area (error in percent) for different regularization parameters for the test distribution *B*.

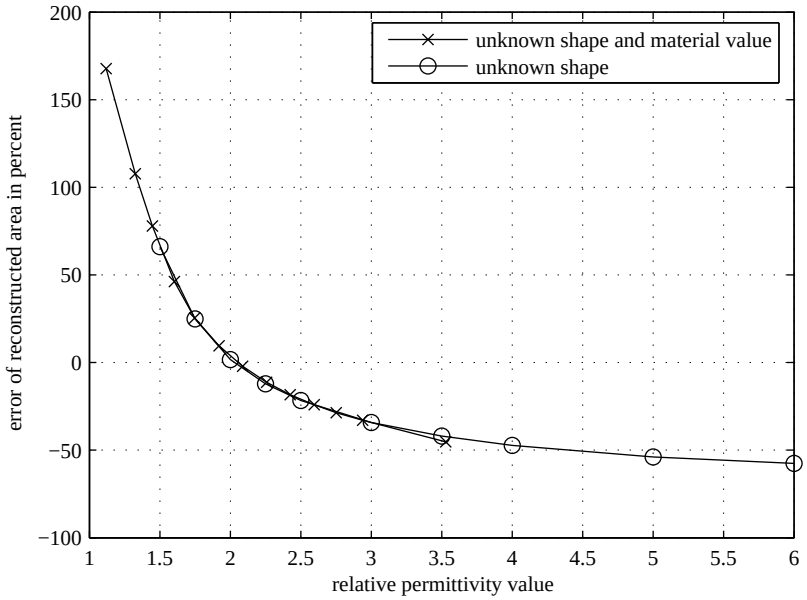

Figure 5.20: Correlation between permittivity value and surface area for both types of reconstruction. If both shape and material value are unknown the regularization parameter determines the points, which are marked with the symbol x. For the shape reconstruction, the material value is constant (second curve, points are marked with an o).

5.2.1 Measurement Noise

In ECT, the electrode capacitances are not sensible to a change in the permittivities in the center of pipe. Without regularization small perturbations in the data (measurement noise) strongly influence the reconstructed image. This section analyzes the stability of the reconstruction with respect to real world measurement noise.

The sensor frontends have a non-linear characteristics (a logarithmic demodulator is used) and the variance of the noise depends on the operating point of the amplifier. As shown in (1.7) the covariance matrix weights the measurement data. In figure 5.21 the reconstruction result is shown for the measurement setup A whereas each charge is weighted evenly. In other words the covariance matrix equals the identity matrix. The imaging process fails and the two objects can not be identified.

To qualify the stability of the imaging process, 160 measurements have been carried out for each test distribution whereas the objects remain fixed. In other words no process noise is considered. For each data a reconstruction is performed and the image is analyzed. For this process the regularization parameter ($\alpha^2 = 10^{-3.75}$) is constant and the initial condition is, as above, a centered circle with a relative permittivity of two. The reconstruction converges successfully for each sample. Table 5.1 summarizes sample mean values, standard deviations, and the minimum and maximum values of the obtained area, which is enclosed by the surface, and of its permittivity value. Different to the permittivity, which has a small variance, the area spreads in a wide range.

The reconstructed interfaces are visualized in figure 5.22(a). It is remarkable that the

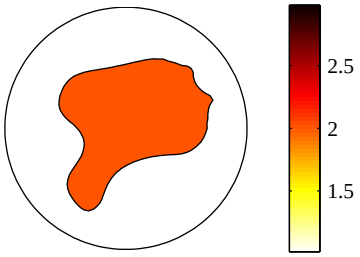

Figure 5.21: Reconstruction result where the measurement values are weighted equally.

	mean	3σ	min	max
surface error in percent	-6.3	5.70	-11.1	-2.0
relative permittivity	2.14	0.08	2.06	2.22

Table 5.1: Influence of real world measurement noise on the reconstruction. The mean, standard deviation σ, minimum, and maximum values are given.

contours spread similarly in all directions. This is contrary to the expected behavior that points on the contour near the center are more difficult to estimate than the points closer to the pipe wall. To characterize the results the centroids of the objects are calculated (visualized as points in the center of each object). One can observe that they hardly spread. For a further visualization the mean shapes [2], the mean centroids, and their associated confidence regions are plotted (shown in figure 5.22(b)). In this work the confidence region is defined as error ellipsoid, whose points have three times the standard deviation of the deviation of the centroids. For a closer look on the obtained images following quality parameters are introduced:

- the surface area, the relative permittivity ε_r, and the position c_x and c_y of the centroid of each object, and
- distance d between the two objects, which is measured by the distance between their centroids.

Similar as above the result of all 160 measurements is summarized in table 5.2. It is worth noting that the position of the semicircle is estimated with less deviation than the circular object, even though the semicircle is located closer to the center. The semicircle, however, has a greater influence on the displacement currents due to its larger surface area.

The correlation coefficients (Pearson product-moment), which are calculated by the covariance matrix of the quality parameters, are shown in table 5.3. These coefficients indicate the strength of a linear relationship between two criteria. Note that a careful interpretation of the coefficients is necessary because the Pearson matrix is an optimal estimator only for Gaussian data. Additionally, a coefficient near zero does not indicate that there is no correlation between two criteria (there exists probably a non-linear relationship

[2] To visualize the mean shape, the average over all level set functions of each object is calculated and its zero level contour is plotted. This is admissible under the assumption that each level set function is a signed distance function, which is fulfilled in this thesis.

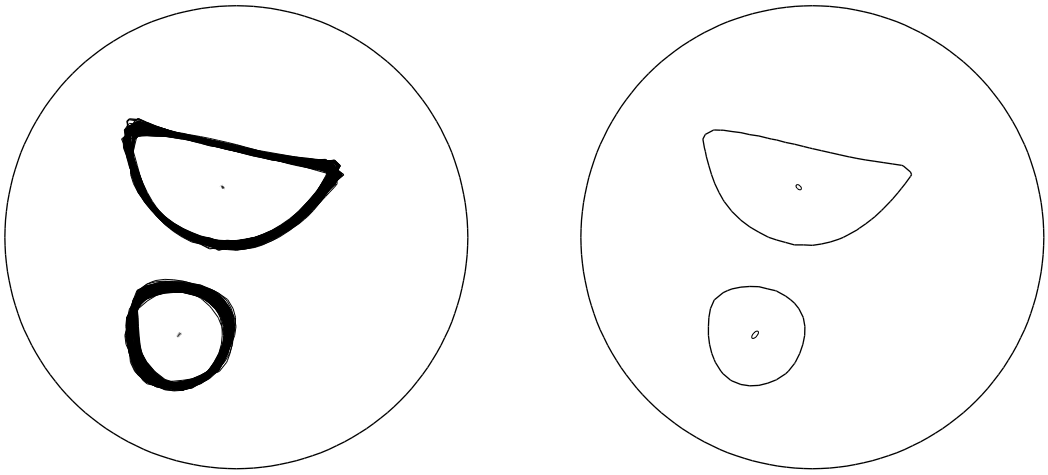

(a) Reconstructed contours (solid lines) and their centroids (points).

(b) Mean shape (solid line), mean centroids (points) and ellipsoids, which define the confidence region of the centroids.

Figure 5.22: Influence of the measurement noise on the reconstructed shape.

	circle				semicircle				distance
	area	ε_r	c_x	c_y	area	ε_r	c_x	c_y	d
	[cm^2]	[−]	[cm]	[cm]	[cm^2]	[−]	[cm]	[cm]	[cm]
true value	3.43				9.01				
mean value	3.89	1.83	−1.28	−2.19	7.77	2.30	−0.31	1.12	3.45
3σ	0.53	0.11	0.08	0.08	0.53	0.12	0.06	0.06	0.08

Table 5.2: Attributes to describe the reconstruction result: surface area, relative permittivity, position of the centroid, and the distance between both centroids (true values, mean values, and standard deviation σ).

		circle				semicircle				
		area	ε_r	c_x	c_y	area	ε_r	c_x	c_y	d
circle	area	1.00	**−0.82**	0.18	0.24	−0.12	0.15	0.17	0.15	−0.14
	ε_r		1.00	0.19	0.16	0.09	−0.04	−0.00	−0.03	−0.22
	c_x			1.00	**0.64**	−0.13	0.14	0.19	0.24	**−0.68**
	c_y				1.00	−0.37	0.25	0.17	**0.40**	**−0.83**
semicircle	area					1.00	**−0.63**	−0.02	−0.21	0.24
	ε_r						1.00	**0.58**	−0.36	**−0.40**
	c_x							1.00	**−0.46**	−0.32
	c_y								1.00	0.14
	d									1.00

Table 5.3: Correlation matrix of the reconstructed attributes. Values near ±1 indicate a linear correlation between two parameters. Absolute values above 0.4 are marked.

between them). The coefficients have values in the range between −1 and 1 and the direction of the linear relationship is indicated by its sign. All entries in the symmetric matrix with an absolute value greater than 0.4 are marked by bold fonts. As expected, there is a negative linear relation between surface area and permittivity value of each object (−0.82 and −0.63). Further the permittivity of the semicircle depends on the x-coordinate of its centroid. A small correlation can be identified between the parameters of the two objects

(with exception of 0.4, which is the coefficient of the y-coordinates of the centroids). The correlation of the distance is calculated by of the coordinates of the centroids. As it is mentioned above, the centroid of the semicircle has a smaller standard deviation than the circular object. Thus there is less correlation between the distance and the centroid of the semicircle than between the distance and the circular object.

5.2.2 Initial Condition

In this subsection the initial condition is altered. Until now, the initial condition is a centered circle (diameter of 4 cm) with a relative permittivity value of $\varepsilon_1 = 2$. For the outer region (background) ε_2 equals one. All simulations in this section are based on the test distribution A and the regularization parameter is fixed $\alpha^2 = 10^{-3.75}$. Table 5.4 presents the iteration numbers until convergence is obtained for different combinations of the initial permittivity values. Therefore the reconstruction starts with the centered circle as before and convergence is obtained if the objective function is less than $0.9 \cdot 10^{-3}$. At this point of the imaging process, a similar result as presented in iteration step nine of figure 5.12 is reconstructed. The reconstruction performs well for almost all initial conditions except in the case where $\varepsilon_1 = 1$ and $\varepsilon_2 = 5$. Even though the reconstruction is successful, the number of iterations increase if the contrast between the permittivities is changed (in other words the rate of convergence decreases if $\varepsilon_1 < \varepsilon_2$).

Not only the permittivity values but also the geometry can be altered. For this test the reconstruction starts with a circle located at the top on the left-hand side (figure 5.23) and with a circle, which is located at the bottom on the right-hand side (figure 5.24). Even though the reconstruction starts with an initial condition far away from the true distribution, one can recognize the approximate shape after few iterations. Obviously, more iterations are necessary until a sufficient image is reconstructed. For the first initial condition 157 out of 160 reconstructions are successful and for the second initial condition, which is far away from the true shape, 152 reconstructions achieve a satisfying result. The mean shapes and centroids are calculated for all convergent reconstructions and the obtained interfaces (the mean shapes for the three initial conditions: circle in the center, on the top left and bottom right hand) are presented in figure 5.25. The contours match almost perfectly. Table 5.5 summarizes the surface area of each object for the three conditions. The standard deviations slightly increase, if the initial circle is located at the bottom on the right-hand side. Similar results are obtained for the permittivity values, which are presented in table 5.6. It can be concluded that the reconstruction technique has a good

iteration numbers		ε_1 (interior region)				
		1	2	3	5	10
ε_2 (background)	1	10	9	9	10	10
	5	–	14	14	12	9
	10	15	16	16	13	13

Table 5.4: Iteration numbers until convergence is achieved (objective function less than $0.9 \cdot 10^{-3}$) for different initial conditions of the relative permittivities. The initial shape is a centered circle. The material values in the interior and exterior region are altered.

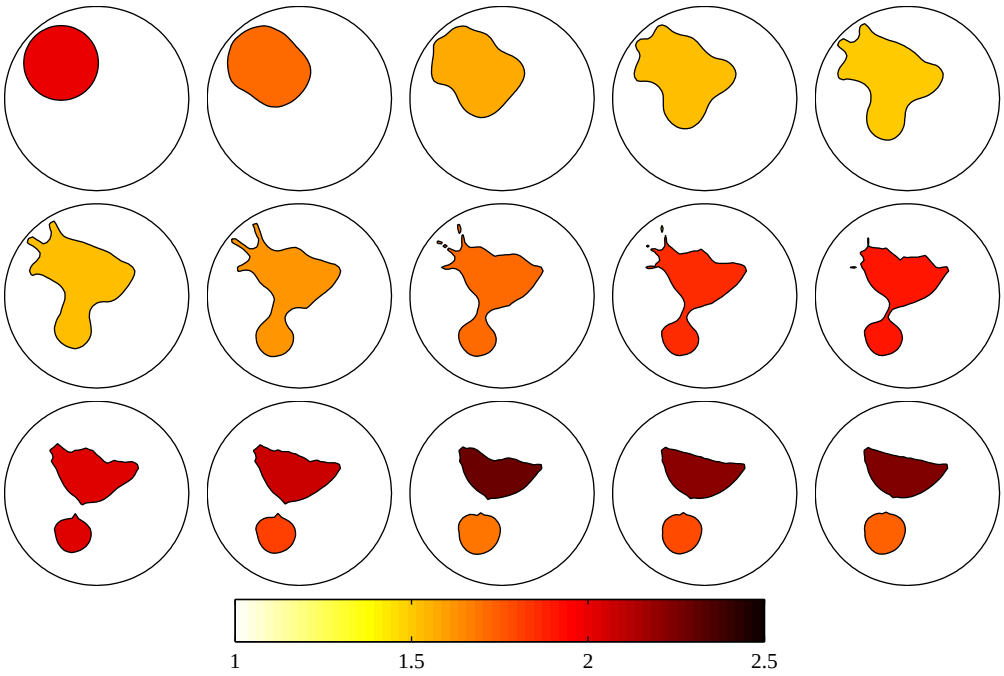

Figure 5.23: The first 14 iteration steps for a geometrically altered initial condition (circle on the top left).

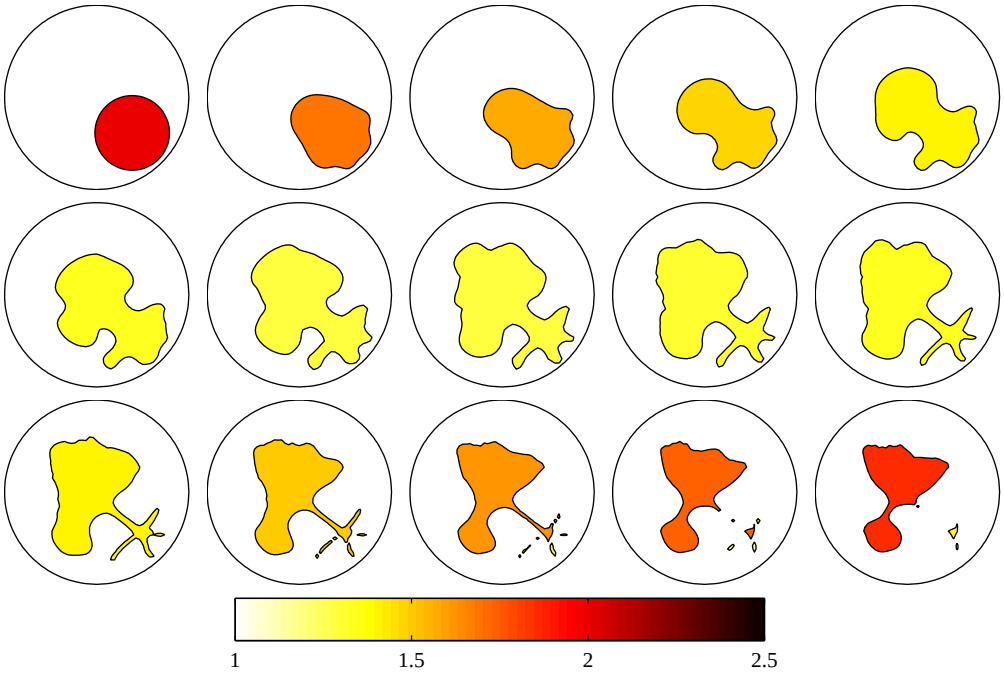

Figure 5.24: The first 14 iteration steps for a geometrically altered initial condition (circle on the bottom right).

global convergence behavior.

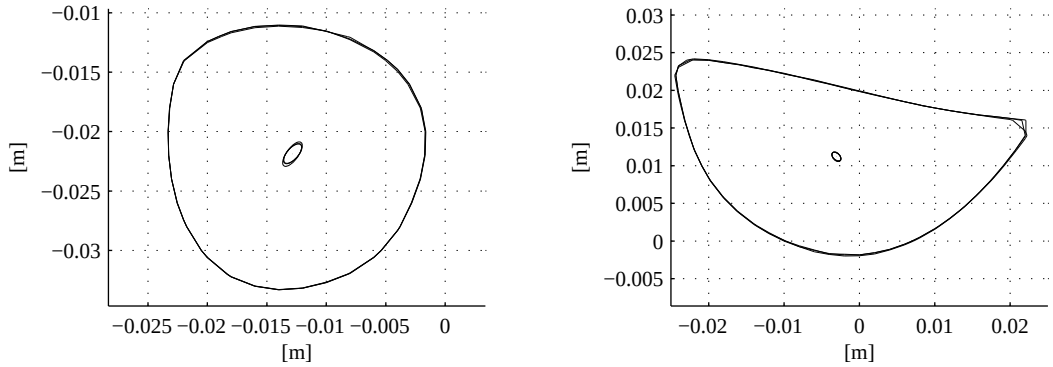

(a) PVC rod.

(b) Semicircle shaped PVC object.

Figure 5.25: Mean shape and mean centroid (with confidence region) for three different initial conditions.

surface [cm^2]		mean	3σ	min	max
circle	center	3.89	0.53	3.46	4.35
	top left	3.89	0.54	3.46	4.38
	bottom right	3.87	0.71	2.88	4.38
semicircle	center	7.77	0.53	7.43	8.19
	top left	7.78	0.55	7.39	8.21
	bottom right	7.84	0.89	7.43	9.61

Table 5.5: Influence of the initial condition on the reconstructed surface area.

relative permittivity		mean	3σ	min	max
circle	center	1.83	0.11	1.76	1.91
	top left	1.83	0.11	1.75	1.92
	bottom right	1.83	0.15	1.75	2.11
semicircle	center	2.30	0.12	2.21	2.40
	top left	2.29	0.12	2.20	2.39
	bottom right	2.28	0.16	2.04	2.39

Table 5.6: Influence of the initial condition on the reconstructed permittivity values.

5.2.3 Limitations of the Proposed Technique

Some limitations and problems of the proposed technique are summarized in this section. First of all figure 5.26(a) presents a test distribution where air bubbles are simulated in a liquid phase (i.e. tap water) by two PVC pipes, which are filled with air. The thickness of the pipe can be neglected. The reconstructed image is shown in figure 5.26(b) and its quality is not sufficient. The contrast of the permittivity values of the phases is too small and additionally the interfaces are blurred.

The small measuring range is unfavorable if the sensor is filled with water (compare with figure 5.4). The analog to digital converter is designed for a measuring range of 80db, which is much more than the necessary 8db. Additionally, the operating point of the amplifier is worse with respect to the measurement noise. Even though the values of the ADC have a very small standard deviation, the absolute deviation of the charges on the electrodes is much higher due to the logarithmic characteristic curve. However, the main issue is the dielectric screen effect, which means that the electric field is absorbed by a material with high permittivity. In other words objects with lower permittivity in a high permittivity component are more difficult to detect than vice versa.

Further test distributions are shown in figure 5.27. In this case the pipe is filled with different levels of water and diesel. The iterations of the optimization process of the first test distribution are shown in figure 5.28. The real fill level is marked with the dash and dot line (note that there is a small rotation of the model compared to the sensor).

After few iterations the phase with material value about $\varepsilon_1 = 2$, which is approximately the value of oil, can be identified. However, a small gap arises between interface and pipe wall. Numerical problems arise because the reconstructed interface is not identical with the pipe wall on the lower part of the region of interest. This can not be handled by the level set function due to the fact that the implicit representation describes only

(a) ECT sensor filled with water. There is air inside the two PVC pipes.

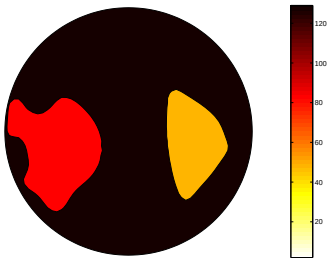

(b) Reconstruction with BEM and level set algorithm.

Figure 5.26: Reconstruction of objects with lower permittivity in a high permittivity component.

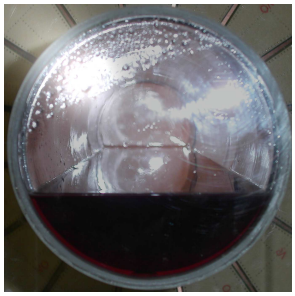

(a) Sensor filled with diesel.

(b) Transition between tap water (bottom), diesel, and air (top).

Figure 5.27: Detection of transitions between several phases.

closed contours. In this example the points of the interface are limited to 98 percent of the pipe radius (leaving 2 percent of air between the interior object and the pipe wall, which is an 1 mm thick tube). As shown in figure 5.29, the algorithm gets stuck at iteration step 7. The material values of the iteration steps are shown in figure 5.30.

The second test distribution (figure 5.27(b)) consists of three phases, namely water, diesel, and air (from bottom to top). Again the problem arises that the level set function can not describe an open contour. Additionally, the contrast between air and diesel is very low compared to the permittivity of water. At the present moment an image of sufficient quality can not be obtained. However, a possible solution for the contrast problem is the fusion with data from URT, which provides the necessary information about the location of the phase transitions.

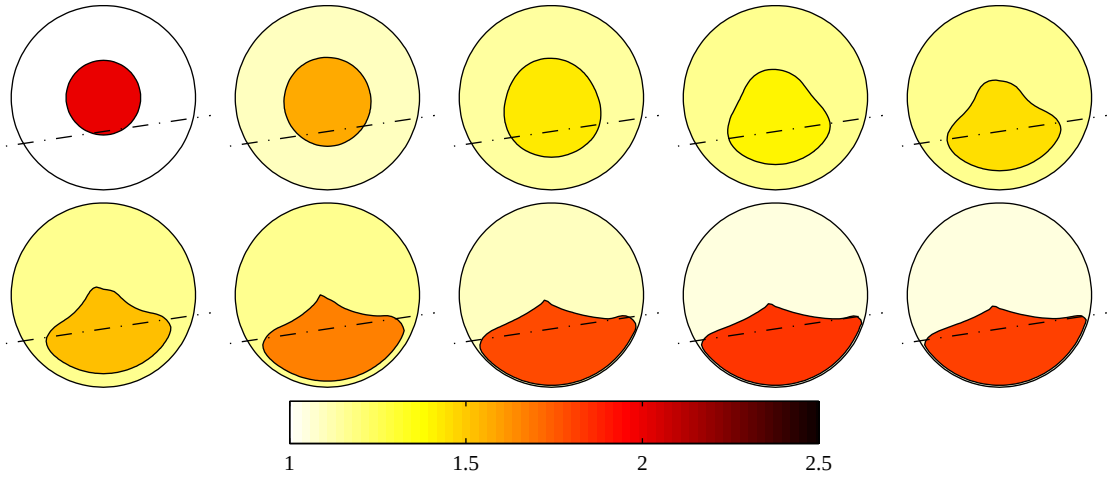

Figure 5.28: Reconstruction of the transition between diesel and air. The dot and dash line marks the real fill level.

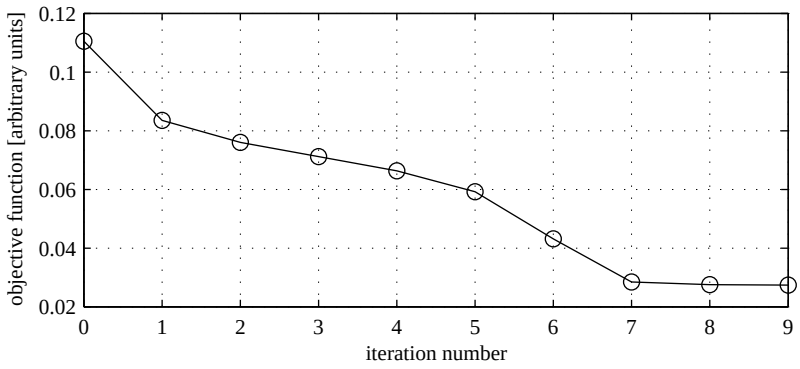

Figure 5.29: Convergence of the fill level reconstruction.

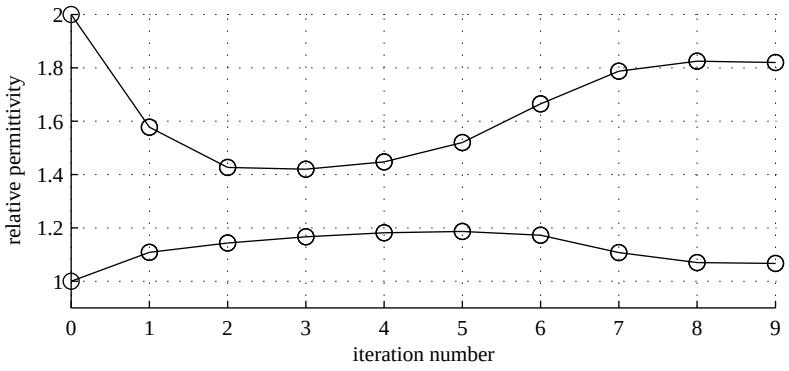

Figure 5.30: Material values of each reconstructed phase.

5.3 Conclusion

This thesis presents a shape reconstruction technique, which identifies the location of phase transitions and which determines the material value of each region. This algorithm overcomes difficulties, which are mainly caused by the soft field modality of electrical capacitance tomography. The blurring of reconstructed images is avoided because the inverse problem of ECT is formulated as shape optimization problem.

Commonly used reconstruction techniques rely on the FEM to solve the corresponding forward problems. A fine mesh is necessary to obtain images with high spatial accuracy. However the computational effort, which is required to solve the field problem and which is necessary to invert the Hessian matrix, strongly increases by the number of finite elements. On the other hand the BEM, which is utilized in this work, is of advantage if the unknown material distribution is described by means of piecewise constant permittivities. Additionally, shape and material derivatives are calculated easily by the adjoint variable method with few computational costs.

The level set framework is implemented in this thesis instead of a parameterization of the contour. This technique is an accurate and flexible description of objects and it is not essential to know the number of phases a priori. Regularization of Tikhonov type is utilized and the magnitude of the regularization is controlled by a regularization parameter.

The inverse problem is solved by a non-linear optimization technique. Fast and stable convergence is obtained by a Newton method with a line search algorithm. Additionally, physical constraints are incorporated by an active set method.

The suggested imaging technique has proven that it successfully reconstructs images of real world measurement data. Therefore experimental results are presented. For the data acquisition a prototype sensor, which is based on the measurement of displacement currents, is used. Furthermore, tests show that the reconstruction is stable with respect to measurement noise and with respect to the initial condition of the optimization process.

The resulting images can be used for the calculation of process relevant information, like the volume fraction of different phases. It is worth mentioning that no arbitrary threshold value is necessary to obtain this process parameter. Even though the regularization parameter has less influence on the result if the material values of the phases are

known, it strongly affects the reconstructed surface area if the permittivity values are unknown additionally to the shape. It is shown that this correlation is a fundamental attribute of this kind of inverse problem. In the case of unknown material values, supplementary information improves the accuracy of the image. For instance ultrasound reflection tomography can provide additional information about the location of phase transitions. A regularization technique, which relies on information from URT, is presented in this work. Experimental results on the basis of simulations are promising.

The accuracy of electrical capacitance tomography can be improved by a technique, which takes care of 3D aspects. Further development will focus on this topic. A 3D reconstruction becomes feasible what the computation time is concerned if a fast boundary element method is applied (e.g. multipole boundary element method [81]). Additionally, efficient solvers for the optimization problem are mandatory because the number of unknown variables increases. The extension of the level set formulation to 3D, however, is straight forward.

Bibliography

[1] D. Adalsteinsson and J. A. Sethian. The fast construction of extension velocities in level set methods. *Journal of Computational Physics*, 148(1):2–22, 1999.

[2] G. Bal and K. Ren. Reconstruction of singular surfaces by shape sensitivity analysis and level set method. preprint, 2005.

[3] L. K. Baxter. *Capacitive Sensors*. IEEE Press, New York, 1997.

[4] A. Blake and M. Isard. *Active Contours*. Springer, Berlin, 1998.

[5] M. Bonnet. BIE and material differentiation applied to the formulation of obstacle inverse problems. *Engineering Analysis with Boundary Elements*, 15(2):121–136, 1995.

[6] A. Borsic. *Regularisation Methods for Imaging from Electrical Measurements*. PhD thesis, Oxford Brookes University, 2002.

[7] J. E. Boyd and J. J. Little. Complementary data fusion for limited-angle tomography. In *IEEE Computer Society Conference on Computer Vision and Pattern Recognition*, pages 288–294, Los Alamitos, CA, USA, 1994.

[8] B. Brandstätter, G. Holler, and D. Watzenig. Reconstruction of inhomogeneities in fluids by means of capacitance tomography. *COMPEL International Journal for Computation and Mathematics in Electrical and Electronic Engineering*, 22(3):508–519, 2003.

[9] B. Brandstätter, G. Holler, and D. Watzenig. Spatially resolving dielectric analysis of fluids by means of electrical capacitance tomography. In *11th International Trade Fair and Conference (SENSOR 2003)*, pages 323–328, Nürnberg, Germany, 2003.

[10] B. Brandstätter, G. Steiner, B. Kortschak, H. Wegleiter, and D. Watzenig. Fusion of electrical capacitance with ultrasound tomography - analysis of methods. In *4th World Congress on Industrial Process Tomography*, pages 564–569, Aizu, Japan, 2005.

[11] B. Brandstätter, G. Steiner, B. Kortschak, H. Wegleiter, and D. Watzenig. Fusion of electrical capacitance with ultrasound tomography - implementation details and hardware setup. In *4th World Congress on Industrial Process Tomography*, pages 631–636, Aizu, Japan, 2005.

[12] G. Brasseur. Design rules for robust capacitive sensors. *IEEE Transactions on Instrumentation and Measurement*, 52(4):1261–1265, 2003.

[13] C. A. Brebbia. *The Boundary Element Method for Engineers*. Pentech Press, London, 1984.

[14] M. Burger. A framework for the construction of level set methods for shape optimization and reconstruction. *Interfaces and Free Boundaries*, 5:301–329, 2003.

[15] M. Burger. Levenberg-marquardt level set methods for inverse obstacle problems. Report 03-45, UCLA Computational and Applied Mathematics, 2003.

[16] M. Burger, B. Hackl, and W. Ring. Incorporating topological derivatives into level set methods. *Journal of Computational Physics*, 194:344–362, 2004.

[17] T. F. Chan and X. Tai. Identification of discontinuous coefficients in elliptic problems using total variation regularization. *SIAM Journal on Scientific Computing*, 25(3):881–904, 2003.

[18] T. F. Chan and X. Tai. Level set and total variation regularization for elliptic inverse problems with discontinuous coefficients. *Journal of Computational Physics*, 193:40–66, 2003.

[19] T. F. Chan and L. A. Vese. Active contours without edges. *IEEE Transactions on Image Processing*, 10(2):266–277, 2001.

[20] E. Chung, T. F. Chan, and X. Tai. Electrical impedance tomography using level set representation and total variational regularization. *Journal of Computational Physics*, 205(1):357–372, 2005.

[21] M. C. Delfour and J.-P. Zolesio. *Shapes and Geometries: Analysis, Differential Calculus, and Optimization*, volume 4 of *Advances in Design and Control*. SIAM, Philadelphia, 2001.

[22] S. Deng, K. Ito, and Z. Li. Three-dimensional elliptic solvers for interface problems and applications. *Journal of Computational Physics*, 184:215–243, 2003.

[23] F. J. Dickin, B. S. Hoyle, A. Hunt, S. M. Huang, O. Ilyas, C. Lenn, R. C. Waterfall, R. A. Williams, C. G. Xie, and M. S. Beck. Tomographic imaging of industrial process equipment: techniques and applications. *IEE Proceedings: Circuits, Devices and Systems*, 139(1):72–82, 1992.

[24] O. Dorn, E. Miller, and C. Rappaport. A shape reconstruction method for electromagnetic tomography using adjoint fields and level sets. *Inverse Problems*, 16:1119–1156, 2000.

[25] R. Duraiswami, G. L. Chahine, and K. Sarkar. Efficient 2D and 3D electrical impedance tomography using boundary element methods. *Chemical Engineering Science*, 52:2185–2196, 1997.

[26] R. Duraiswami, K. Sarkar, and G. L. Chahine. Efficient dual-reciprocity boundary element techniques for electrical impedance tomography. *Engineering Analysis with Boundary Elements*, 22:13–31, 1998.

[27] T. Dyakowski, R. B. Edwards, C. G. Xie, and R. A. Williams. Application of capacitance tomography to gas-solid flows. *Chemical Engineering Science*, 52(13):2099–2110, 1997.

[28] H. W. Engl, M. Hanke, and A. Neubauer. *Regularization of Inverse Problems*. Mathematics and its Applications. Kluwer, Dordrecht, 1996.

[29] R. Fletcher. *Practical Methods of Optimization*. Wiley, New York, 2nd edition, 2000.

[30] A. Fuchs, B. Brandstätter, D. Watzenig, G. Holler, and B. Kortschak. Flow profile estimator for closed pipes based on electrical capacitance tomography techniques. In *Instrumentation and Measurement Technology Conference (IMTC)*, pages 2326–2331, Como, Italy, 2004.

[31] A. Fuchs, B. Kortschak, G. Holler, H. Wegleiter, and G. Brasseur. Flow property determination in homogeneous media by means of perturbation injection. In *4th IEEE Conference on Sensors*, pages 680–683, Irvine, California, 2005.

[32] J. C. Gamioa, J. Castroa, L. Riveraa, J. Alamillaa, F. Garcia-Nocettib, and L. Aguilarb. Visualisation of gas oil two-phase flows in pressurised pipes using electrical capacitance tomography. *Flow Measurement and Instrumentation*, 16:129–134, 2005.

[33] P. Gill, W. Murray, and M. Wright. *Practical Optimization*. Academic Press, London, 1981.

[34] P. C. Hansen. Analysis of discrete ill-posed problems by means of the l-curve. *SIAM Rev.*, 34(4):561–580, 1992.

[35] M. Hintermüller and W. Ring. A second order shape optimization approach for image segmentation. *SIAM Journal on Applied Mathematics*, 64(2):442–467, 2003.

[36] M. Hintermüller and W. Ring. An inexact Newton-CG-type active contour approach for the minimization of the Mumford-Shah functional. *Journal of Mathematical Imaging and Vision*, 20:19–42, 2004.

[37] G. Holler, A. Fuchs, and B. Schweighofer. Hardware design and measurement results for an electrical capacitance tomography system. In *6th International Conference on Electronic Measurement and Instruments (ICEMI 2003)*, pages 1–6, Taiyuan, China, 2003.

[38] G. Holler, T. Thurner, H. Zangl, and G. Brasseur. A novel capacitance sensor principle applicable for spatially resolving downhole measurements. In *19th IEEE Instrumentation and Measurement Technology Conference (IMTC 2002)*, page 1157 1160, Anchorage, Alaska, 2002.

[39] B. S. Hoyle, X. Jia, F. J. W. Podd, H. I. Schlaberg, H. S. Tan, M. Wang, R. M. West, R. A. Williams, and T. A. York. Design and application of a multi-modal process tomography system. *Measurement Science and Technology*, 12:1157–1165, 2001.

[40] C.-T. Hsiao, G. Chahine, and N. Gumerov. Application of a hybrid genetic/powell algorithm and a boundary element method to electrical impedance tomography. *Journal of Computational Physics*, 173:433–454, 2001.

[41] K. Ito. Level set methods for variational problems and application. *Control and Estimation of Distributed Parameter Systems, ISNM*, 143:203–217, 2002.

[42] K. Ito, K. Kunisch, and Z. Li. Level-set function approach to an inverse interface problem. *Inverse Problems*, 17(5):1225–1242, 2001.

[43] H. J. Jeon, J. H. Kim, B. Y. Choi, K. Y. Kim, M. C. Kim, and S. Kim. Electrical impedance imaging of binary mixtures with boundary estimation approach based on multilayer neural network. *IEEE Sensors Journal*, 5(2):313–320, 2005.

[44] G. Jiang and D. Peng. Weighted ENO schemes for Hamilton–Jacobi equations. *SIAM Journal on Scientific Computing*, 21(6):2126–2143, 2000.

[45] K. Y. Kim, B. S. Kim, M. C. Kim, S. Kim, Y. J. Lee, H. J. Jeon, B. Y. Choi, and M. Vauhkonen. Electrical impedance imaging of two-phase fields with an adaptive mesh grouping scheme. *IEEE Transactions on Magnetics*, 40(2):1124–1127, 2004.

[46] M. C. Kim, S. Kim, K. Y. Kim, K. H. Seo, H. J. Jeon, J. H. Kim, and B. Y. Choi. Estimation of phase boundary by front points method in electical impedance tomography. In *Inverse Problems, Design and Optimization Symposium*, volume 2, pages 101–107, Rio de Janeiro, Brazil, 2004.

[47] M. C. Kim, S. Kim, K. J. Lee, and K. Y. Kim. Improvement of the electrical impedance tomographic image for the two-phase system with adaptive element grouping technique. *Measurement Science and Technology*, 15:1391–1401, 2004.

[48] V. Kolehmainen, S. R. Arridge, W. R. B. Lionheart, M. Vauhkonen, and J. P. Kaipio. Recovery of region boundaries of piecewise constant coefficients of an elliptic PDE from boundary data. *Inverse Problems*, 15:1375–1391, 1999.

[49] B. Kortschak and B. Brandstätter. A FEM-BEM approach using level-sets in electrical capacitance tomography. In *11th International IGTE Symposium on Numerical Field Calculation in Electrical Engineering*, pages 301–307, Seggauberg, Austria, 2004.

[50] B. Kortschak and B. Brandstätter. Comparison of two functionals for different measurement principles for non-linear capacitance tomography. In *5th International Conference on Inverse Problems in Engineering: Theory and Practice*, volume 2, Cambridge, UK, 2005.

[51] B. Kortschak and B. Brandstätter. A FEM-BEM approach using level-sets in electrical capacitance tomography. *COMPEL International Journal for Computation and Mathematics in Electrical and Electronic Engineering*, 24(2):591–605, 2005.

[52] B. Kortschak, H. Wegleiter, and B. Brandstätter. Formulation of cost functionals for different measurement principles in non-linear capacitancetomography. *submitted to Measurement Science and Technology*, 2006.

[53] D. Lesnic and L. Marin. Tutorial on inverse analysis with boundary elements. In *Inverse Problems, Design and Optimization Symposium*, volume 1, pages 69–78, Rio de Janeiro, Brazil, 2004.

[54] W. R. B. Lionheart. Eit reconstruction algorithms: pitfalls, challenges and recent developments. *Physiological Measurement*, 25:125–142, 2004.

[55] A. Litman, D. Lesselier, and F. Santosa. Reconstruction of a two-dimensional binary obstacle by controlled evolution of a level-set. *Inverse Problems*, 14:685–706, 1998.

[56] R. A. Meric. Differential and integral sensitivity formulations and shape optimization by BEM. *Engineering Analysis with Boundary Elements*, 15:181–188, 1995.

[57] J. Montagnat, H. Delingette, and N. Ayache. A review of deformable surfaces: topology, geometry and deformation. *Image and Vision Computing*, 19(14):1023–1040, 2001.

[58] S. Osher. *Geometric level set methods in imaging, vision, and graphics*. Springer, New York, 2003.

[59] S. Osher and R. Fedkiw. *Level Set Methods and Dynamic Implicit Surfaces*. Number 153 in Applied Mathematical Sciences. Springer, New York, 2003.

[60] S. Osher and R. P. Fedkiw. Level set methods: An overview and some recent results. *Journal of Computational Physics*, 169:463–502, 2001.

[61] S. Osher and J. A. Sethian. Fronts propagating with curvature-dependent speed: Algorithms based on Hamilton-Jacobi formulations. *Journal of Computational Physics*, 79:12–49, 1988.

[62] D. M. Otten and B. Rubinsky. Front-tracking image reconstruction algorithm for EIT-monitored cryosurgery using the boundary element method. *Physiological Measurement*, 26:503–516, 2005.

[63] D. Peng, B. Merriman, S. Osher, H. Zhao, and M. Kang. A PDE–based fast local level set method. *Journal of Computational Physics*, 155:410–438, 1999.

[64] A. Plaskowski, M. S. Beck, R. Thorn, and T. Dyakowski. *Imaging industrial flows, applications of electrical process tomography*. Inst. of Physics Publ., Bristol, 1995.

[65] C. Pröll. Bayesian recursive filter approaches to solve the inverse problem in electrical capacitance tomography. diploma theses, Graz University of Technology, 2005.

[66] L. Rondi and F. Santosa. Enhanced electrical impedance tomography via the Mumford-Shah functional. *ESAIM: Control, Optimisation and Calculus of Variations*, 6:517–538, 2001.

[67] L. I. Rudin and S. Osher. Total variation based image restoration with free local constraints. *IEEE International Conference on Image Processing*, 1:31–35, 1994.

[68] F. Santosa. A level-set approach for inverse problems involving obstacles. *ESAIM: Control, Optimisation and Calculus of Variations*, 1:17–33, 1996.

[69] H. I. Schlaberg, F. J. W. Podd, and B. S. Hoyle. Ultrasound process tomography system for hydrocyclones. *Ultrasonics*, 38:813–816, 2000.

[70] H. I. Schlaberg, M. Yang, and B. S. Hoyle. Ultrasound reflection tomography for industrial processes. *Ultrasonics*, 36:297–303, 1998.

[71] D.M. Scott and H. McCann, editors. *Process imaging for automatic control*, volume 124 of *Electrical and computer engineering*. Taylor and Francis, Boca Raton, Fla., 2005.

[72] J. A. Sethian. Adaptive fast marching and level set methods for propagating interfaces. *Acta Math. Univ. Comenianae*, LXVII(1):3–15, 1998.

[73] J. A. Sethian. *Level Set Methods and Fast Marching Methods*, volume 3 of *Cambridge monographs on applied and computational mathematics*. Cambridge University Press, 2 edition, 1999.

[74] H. Shim. Level set based simulations of two-phase oil-water flows in pipes. Report 00-18, UCLA Computational and Applied Mathematics, University of California, 2000.

[75] J. Sokolowski and A. Zochowski. On the topological derivative in shape optimization. *SIAM Journal on Control and Optimization*, 37(4):1251–1272, 1999.

[76] J. Sokolowski and J.-P. Zolesio. *Introduction to Shape Optimization: Shape Sensitivity Analysis*. Springer Series in Computational Mathematics. Springer, Berlin, 1992.

[77] M. Soleimani. *Image and Shape Reconstruction methods in Magnetic Induction Tomography*. PhD thesis, University of Manchester, 2005.

[78] M. Soleimani, R. G. Aykroyd, S. Freear, W. R. B. Lionheart, and F. Podd. Multimodal data for enhanced imaging applied to 3d ERT with ultrasound time of flight data. In *4th World Congress on Industrial Process Tomography*, pages 663–668, Aizu, Japan, 2005.

[79] M. Soleimani and W. R. B. Lionheart. Nonlinear image reconstruction for electrical capacitance tomography using experimental data. *Measurement Science and Technology*, 16:1987–1996, 2005.

[80] M. Sonka, V. Hlavac, and R. Boyle. *Image processing, analysis, and machine vision*. PWS Publ., Pacific Grove, Calif., 2. ed. edition, 1999.

[81] O. Steinbach. *Numerische Näherungsverfahren für elliptische Randwertprobleme*. Teubner, Wiesbaden, 2003.

[82] G. Steiner, D. Watzenig, B. Brandstätter, and B. Kortschak. A sequential ultrasonic and electrical capacitance process tomography system. In *5th International Conference on Inverse Problems in Engineering: Theory and Practice*, volume 3, Cambridge, UK, 2005.

[83] A. Tamburrino and G. Rubinacci. A new non-iterative inversion method for electrical resistance tomography. *Inverse Problems*, 18:1809–1829, 2002.

[84] S. R. Titus, A. O. Hero, and J. A. Fessler. NMR object boundaries: B-spline modeling and estimator performance. In *International Conference on Acoustics, Speech, and Signal Processing*, volume 4, pages 2423–2426, 1995.

[85] O.-P. Tossavainen, M. Vauhkonen, L. M. Heikkinen, and T. Savolainen. Estimating shapes and free surfaces with electrical impedance tomography. *Measurement Science and Technology*, 15(7):1402–1411, 2004.

[86] L. A. Vese and T. F. Chan. A multiphase level set framework for image segmentation using the Mumford and Shah model. *International Journal of Computer Vision*, 50(3):271–293, 2002.

[87] C. R. Vogel. *Computational Methods for Inverse Problems*. Frontiers in Applied Mathematics. SIAM, Philadelphia, 2002.

[88] M. Y. Wang, X. Wang, and D. Guo. A level set method for structural topology optimization. *Computer Methods in Applied Mechanics and Engineering*, 192:227–246, 2003.

[89] H. Wegleiter, A. Fuchs, G. Holler, and B. Kortschak. Analysis of hardware concepts for electrical capacitance tomography applications. In *4th IEEE Conference on Sensors*, pages 688–691, Irvine, California, 2005.

[90] Q. Xia, M. Y. Wang, S. Y. Wang, and S. K. Chen. Semi-Lagrange method for level-set based structural topology and shape optimization. Structural and Multidisciplinary Optimization, 2005.

[91] C. G. Xie, S. M. Huang, B. S. Hoyle, R. Thorn, C. Lenn, D. Snowden, and M. S. Beck. Electrical capacitance tomography for flow imaging: system model for development of image reconstruction algorithms and design of primary sensors. *IEE Proceedings: Circuits, Devices and Systems*, 138(1):89–98, 1992.

[92] Lijun Xu, Yongtao Han, Ling-An Xu, and Jisheng Yang. Application of ultrasonic tomography to monitoring gas/liquid flow. *Chemical Engineering Science*, 52(13):2171–2183, 1997.

[93] H. Zhao, X. Gu, and H. Jiang. Imaging small absorbing and scattering objects in turbid media using diffuse optical tomography structurally guided by reconstructive ultrasound tomography. *Optics Communications*, 238:51–55, 2004.

List of Figures

List of Tables

List of Abbreviations

ADC analog to digital converter
AVM adjoint variable method
BEM boundary element method
CFL Courant, Friedrichs, and Lewy
CT computed tomography
DOT diffuse optical tomography
ECT electrical capacitance tomography
EIT electrical impedance tomography
EMC electromagnetic compatibility
ERT electrical resistance tomography
et al. et alteri/alterae/altera
etc. et cetera
e.c. exempli causa
e.g. exempli gratia
FEM finite element method
GCV generalized cross validation
i.e. id est
MAP maximum a posteriori
MIT magnetic induction tomography
ODE ordinary differential equation
PDE partial differential equation
SNR signal to noise ratio
SQP sequential quadratic programming
TOF time-of-flight
TVR total variational regularization
URT ultrasound reflection tomography

List of Symbols and Variables

$\circ$ composed with

∇_Γ tangential gradient (if applied to a scalar)

$f|_{x=a}$ function value evaluated at point $x = a$; $f|_a^b = f|_{x=b} - f|_{x=a}$

$\mathbf{C}$ covariance matrix of the measurement noise

c_x, c_y coordinate of the centroid of a reconstructed object

D^+, D^- forward and backward finite difference quotient

D region of interest, interior of the PVC pipe

ds arc length measure

E appropriate set of domains i.e. *smooth enough*

F, G normal component of the velocity defined on the unknown interface

$\tilde{F}$ normal component of the velocity extended to the whole domain

g image of prior information about phase transition from URT

$H(\Phi)$ Heaviside function

$\mathbf{J}_\Gamma$ Jacobian with respect to a geometrical deformation

$\mathbf{J}_\varepsilon$ Jacobian with respect to the material values

N linear shape function

$\vec{n}$ outward or inward unit normal vector

$\vec{q}_m$ vector of all measured charges

$\vec{q}(\varepsilon)$ calculated charges in dependency of the spatial distributed permittivity

$R(\vec{\varepsilon}, \Gamma)$ regularization term

$S(\Phi)$ signature of the level set function

t artificial time of the reconstruction process

u spatial distributed electric potential

u' shape derivative (fixed coordinate system)

$\dot{u}$ material derivative (moving coordinate system)

$\overline{u}$ adjoint variable

$U^*(\vec{x},\vec{y})$ fundamental solution

$\vec{V}_F$ velocity field

$\vec{X}$ initial point at the beginning of the deformation ($t = 0$)

ε spatial distributed permittivity value

ε_r relative permittivity of a reconstructed object

κ curvature

Γ_0 surface of the exciting electrode

Γ_e surface of the measuring electrode

Γ_t perturbation of a surface

$\Phi(\vec{x},t)$ spatial distributed and time dependent level set function

Ω_e domain of the measuring electrode

Ω_t perturbation of a domain

Indices

q_i calculated charge on electrode i, n_i is the number of all charges

F_j deformation speed on nodal point j or boundary element j, $\vec{F}$ is of size n_j

k iteration step

ε_l material value of phase l, n_l number of all phases

Φ_p level set function p, n_p number of all level set functions

Appendix A

1D Example of Shape Derivatives

In this appendix a plate capacitor with infinite extension and finite distance of the plate is considered as shown in figure A.1. It consists of two regions with different permittivities ε_1 and ε_2. Dirichlet boundary conditions are applied on the other two sides and the boundary value problem

$$\frac{\partial}{\partial x}\left(\varepsilon\frac{\partial}{\partial x}u\right) = 0 \tag{A.1}$$

with

$$u(0) = 0 \tag{A.2}$$
$$u(1) = 1 \tag{A.3}$$

is considered. The permittivity value ε has a discontinuity at $x = a$ and the permittivity is

$$\varepsilon(x) = \begin{cases} \varepsilon_1 & \text{if } x \in (0,a) \\ \varepsilon_2 & \text{if } x \in (a,1) \end{cases}. \tag{A.4}$$

In the following two sections, the direct differentiation approach is compared with the adjoint variable method for the displacement field at $x = 0$. This displacement is defined by

$$D = -\varepsilon_1 \frac{\partial u}{\partial x}\bigg|_{x=0}. \tag{A.5}$$

A.1 Direct Differentiation

The electric potential is linear in each region and the linear functions

$$u_1 = \xi_1 x + \zeta_1 \tag{A.6}$$
$$u_2 = \xi_2 x + \zeta_2 \tag{A.7}$$

are introduced. At $x = a$ the equations

$$u_1 = u_2 \tag{A.8}$$
$$\varepsilon_1 \frac{\partial u_1}{\partial x} = \varepsilon_2 \frac{\partial u_2}{\partial x} \tag{A.9}$$

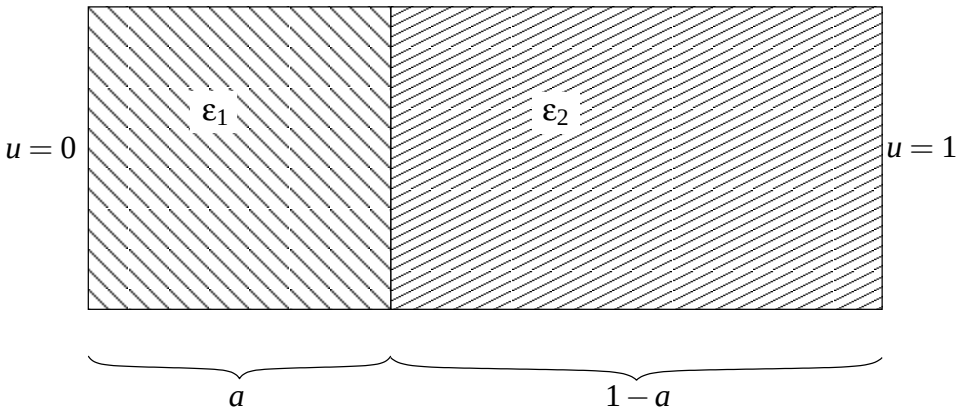

Figure A.1: Example of a plate capacitor with two different materials.

are satisfied and with the boundary conditions (A.2) and (A.3) the coefficients are determined as

$$\xi_1 = \frac{\varepsilon_2}{\varepsilon_1(1-a)+\varepsilon_2 a} \tag{A.10}$$

$$\zeta_1 = 0 \tag{A.11}$$

$$\xi_2 = \frac{\varepsilon_1}{\varepsilon_1(1-a)+\varepsilon_2 a} \tag{A.12}$$

$$\zeta_2 = \frac{a(\varepsilon_2-\varepsilon_1)}{\varepsilon_1(1-a)+\varepsilon_2 a}. \tag{A.13}$$

For the displacement at $x = 0$ one obtains

$$D = -\frac{\varepsilon_1\varepsilon_2}{\varepsilon_1(1-a)+\varepsilon_2 a}. \tag{A.14}$$

In this simple example an analytical solution exists and it is straightforward to calculate the derivative with respect to a, ε_1, and ε_2.

$$\frac{\partial}{\partial a}D = \frac{\varepsilon_1\varepsilon_2(\varepsilon_2-\varepsilon_1)}{(\varepsilon_1(1-a)+\varepsilon_2 a)^2} \tag{A.15}$$

$$\frac{\partial}{\partial \varepsilon_1}D = \frac{-{\varepsilon_2}^2 a}{(\varepsilon_1(1-a)+\varepsilon_2 a)^2} \tag{A.16}$$

$$\frac{\partial}{\partial \varepsilon_2}D = \frac{-{\varepsilon_1}^2(1-a)}{(\varepsilon_1(1-a)+\varepsilon_2 a)^2} \tag{A.17}$$

A.2 Adjoint Variable Approach

Commonly, an analytical solution can not be obtained. In this case the adjoint variable method offers an attractive way to calculate the shape derivative. In this work the adjoint

variable is introduced similar to the method explained in [56]. Multiplication of (A.1) with a weighting function $\bar{u}$ and integration by parts yield

$$S_1 = \int_0^a \varepsilon_1 \frac{\partial u_1}{\partial x}\frac{\partial \bar{u}_1}{\partial x}\,\mathrm{d}x - \bar{u}_1\varepsilon_1\frac{\partial u_1}{\partial x}\bigg|_0^a = 0 \tag{A.18}$$

and

$$S_2 = \int_a^1 \varepsilon_2 \frac{\partial u_2}{\partial x}\frac{\partial \bar{u}_2}{\partial x}\,\mathrm{d}x - \bar{u}_2\varepsilon_2\frac{\partial u_2}{\partial x}\bigg|_a^1 = 0. \tag{A.19}$$

Next one can define a velocity $F = \frac{\mathrm{d}a}{\mathrm{d}t}$, which is zero at $x = 0$ and $x = 1$. The shape derivative of S_1 leads to

$$\begin{aligned}\mathrm{d}S_1(F) = &\int_0^a \left(\varepsilon_1 \frac{\partial u_1}{\partial x}\frac{\partial \bar{u}_1}{\partial x}\right)' \mathrm{d}x + \varepsilon_1\frac{\partial u_1}{\partial x}\frac{\partial \bar{u}_1}{\partial x}F\bigg|_{x=a} \\ &- \dot{\bar{u}}_1\varepsilon_1\frac{\partial u_1}{\partial x}\bigg|_0^a - \bar{u}_1\left(\varepsilon_1\frac{\partial u_1}{\partial x}\right)^{\cdot}\bigg|_0^a = 0\end{aligned} \tag{A.20}$$

where $(x)^{\cdot}$ denotes the material derivative. Now the aim is to define an appropriate adjoint problem such that the last equation can be simplified. To eliminate the shape derivative of the variables u and $\bar{u}$ in the integral term, one can carry out partial integration

$$\begin{aligned}\int_0^a \left(\varepsilon_1 \frac{\partial u_1}{\partial x}\frac{\partial \bar{u}_1}{\partial x}\right)' \mathrm{d}x = &\int_0^a \left(\varepsilon_1' \frac{\partial u_1}{\partial x}\frac{\partial \bar{u}_1}{\partial x} - \varepsilon_1 u_1' \frac{\partial^2 \bar{u}_1}{\partial x^2} - \varepsilon_1 \bar{u}_1' \frac{\partial^2 u_1}{\partial x^2}\right)\mathrm{d}x \\ &+ u_1'\varepsilon_1\frac{\partial \bar{u}_1}{\partial x}\bigg|_0^a + \bar{u}_1'\varepsilon_1\frac{\partial u_1}{\partial x}\bigg|_0^a.\end{aligned} \tag{A.21}$$

The last equation is simplified if the adjoint variable fulfills $\varepsilon_1\frac{\partial^2}{\partial x^2}\bar{u}_1 = 0$. Additionally, the definition of the shape derivative $u_1' = \dot{u}_1 - \frac{\partial}{\partial x}u_1 F$ and $\bar{u}_1' = \dot{\bar{u}}_1 - \frac{\partial}{\partial x}\bar{u}_1 F$ is used. These results are applied to (A.20) and one obtains

$$\mathrm{d}S_1(F) = \int_0^a \varepsilon_1' \frac{\partial u_1}{\partial x}\frac{\partial \bar{u}_1}{\partial x}\,\mathrm{d}x - \bar{u}_1\left(\varepsilon_1\frac{\partial u_1}{\partial x}\right)^{\cdot}\bigg|_0^a + \dot{u}_1\varepsilon_1\frac{\partial \bar{u}_1}{\partial x}\bigg|_0^a - \varepsilon_1\,\frac{\partial u_1}{\partial x}\frac{\partial \bar{u}_1}{\partial x}F\bigg|_{x=a}. \tag{A.22}$$

A similar result for the second region is obtained with $\varepsilon_2\frac{\partial^2}{\partial x^2}\bar{u}_2 = 0$

$$\mathrm{d}S_2(F) = \int_a^1 \varepsilon_2' \frac{\partial u_2}{\partial x}\frac{\partial \bar{u}_2}{\partial x}\,\mathrm{d}x - \bar{u}_2\left(\varepsilon_2\frac{\partial u_2}{\partial x}\right)^{\cdot}\bigg|_a^1 + \dot{u}_2\varepsilon_2\frac{\partial \bar{u}_2}{\partial x}\bigg|_a^1 + \varepsilon_2\,\frac{\partial u_2}{\partial x}\frac{\partial \bar{u}_2}{\partial x}F\bigg|_{x=a}. \tag{A.23}$$

Before the two shape derivatives $\mathrm{d}S_1(F)$ and $\mathrm{d}S_2(F)$ are combined, a few additional equalities are derived. The material derivatives (moving coordinate system) of the interface conditions (A.8) and (A.9) at $x = a$ yield following identity

$$\dot{u}_1 = \dot{u}_2 \tag{A.24}$$

$$\left(\varepsilon_1\frac{\partial u_1}{\partial x}\right)^{\cdot} = \left(\varepsilon_2\frac{\partial u_2}{\partial x}\right)^{\cdot}. \tag{A.25}$$

Additionally, the material derivatives of the boundary conditions (A.2) and (A.3) yield

$$\dot{u}_1|_{x=0} = 0 \tag{A.26}$$
$$\dot{u}_2|_{x=1} = 0. \tag{A.27}$$

Further similar interface conditions as for the primary variable are introduced for the adjoint variable at $x = a$

$$\overline{u}_1 = \overline{u}_2 \tag{A.28}$$
$$\varepsilon_1 \frac{\partial \overline{u}_1}{\partial x} = \varepsilon_2 \frac{\partial \overline{u}_2}{\partial x}. \tag{A.29}$$

Now the addition of the equations (A.22) and (A.23) leads to

$$\overline{u}_1 \left(\varepsilon_1 \frac{\partial u_1}{\partial x} \right)^{\cdot} \Bigg|_0^1 = \int_0^1 \varepsilon' \frac{\partial u}{\partial x} \frac{\partial \overline{u}}{\partial x} \mathrm{d}x + \left(\varepsilon_2 \frac{\partial u_2}{\partial x} \frac{\partial \overline{u}_2}{\partial x} F - \varepsilon_1 \frac{\partial u_1}{\partial x} \frac{\partial \overline{u}_1}{\partial x} F \right) \Bigg|_{x=a} \tag{A.30}$$

The boundary conditions of the adjoint problem are chosen such that the derivative of (A.5) is obtained

$$\overline{u}_1(0) = 1 \tag{A.31}$$
$$\overline{u}_2(1) = 0 \tag{A.32}$$

and this leads to

$$\dot{D} = \int_0^1 \varepsilon' \frac{\partial u}{\partial x} \frac{\partial \overline{u}}{\partial x} \mathrm{d}x + (\varepsilon_1 - \varepsilon_2) \frac{\partial u_1}{\partial x} \frac{\partial \overline{u}_2}{\partial x} F \Bigg|_{x=a}. \tag{A.33}$$

The solution of one additional field problem is required to calculate the material derivative in (A.33). The first term in (A.33) corresponds to a change in the permittivity value and the second term is the sensitivity of a movement of the interface. The adjoint problem is summarized as follows.

$$\frac{\partial}{\partial x} \left(\varepsilon \frac{\partial}{\partial x} \overline{u} \right) = 0 \tag{A.34}$$
$$\overline{u}|_0 = 1 \tag{A.35}$$
$$\overline{u}|_1 = 0 \tag{A.36}$$

The advantage of the adjoint variable method is that an analytical solution is not necessary. This formulation can be used for more complex geometries. The method can be summarized as follows.

1. One starts with the weak formulation in each region of constant permittivity.
2. The shape derivative is performed for each integral.
3. The material derivative of the primary variable is performed. This yields material derivatives of the boundary and interface conditions.

4. An adjoint problem is defined, which fulfills the same partial differential equation and has similar interface conditions.

5. These results are combined and this leads to simple equations with different terms. It consists of the material derivative of the primary variable, the sensitivity with respect to the permittivity, and the sensitivity with respect to the deformation velocity.

6. At last the boundary conditions of the adjoint problem are defined such that the desired material derivative of the primary variable is obtained.

In this special case one can compare the result of the direct differentiation with the adjoint variable method due to the existence of the analytical solution. By substituting the solution of the forward and adjoint problem in (A.33) one obtains the same result as (A.15), (A.16), and (A.17).

Appendix B

Discrete Gradient and Hessian of the Regularization Term

The discretization of the shape derivatives of the regularization term is a cumbersome task. The approximation must be accurate and furthermore the discrete Hessian must be positive definite and symmetric. In the first section, the regularization of the arc length is discussed and in this case the material values are constant. More complex calculations are necessary for the following regularization, which includes the squared jump in the material value.

B.1 Regularization by the Arc Length

Consider the definition of the Newton-type flow (4.1) and the first and second order shape derivatives (4.3) and (4.4), these results are summarized as follows.

$$\underbrace{\int_\Gamma \nabla_\Gamma F \cdot \nabla_\Gamma G \,\mathrm{d}s}_{\mathcal{A}} = -\underbrace{\int_\Gamma \kappa G \,\mathrm{d}s}_{\mathcal{B}} \qquad \text{for all } G : \Gamma \to \mathbb{R} \tag{B.1}$$

To assemble the gradient and the Hessian matrix a spatial discretization is necessary. Therefore one needs a discrete model of Γ. In this work the boundary elements are used as underlying grid. Additionally, an approximation of F, G, and κ is necessary. These functions are assumed to be piecewise linear on each boundary element. Figure B.1 shows for instance two boundary elements with the points p_1, the common point p_2, and p_3 (local indices). The arc length is denoted by s_1 and s_2. The values on the nodal points are denoted by F_i, G_i and κ_i. Note that κ_i is calculated by (2.8). The shape function for point p_2 is linear and $N_j(p_1) = 0$, $N_j(p_2) = 1$ and $N_j(p_3) = 0$ (j is the global index of node point p_2).

The discretization of (B.1) can be written in matrix form as

$$\mathbf{L}\vec{F} = -\vec{k} \tag{B.2}$$

The rows of the gradient $\vec{k}$ (size n_j) and Hessian $\mathbf{L}$ (size $n_j \times n_j$) are calculated by independent test functions G. A natural choice for the test function is to use the shape function. In

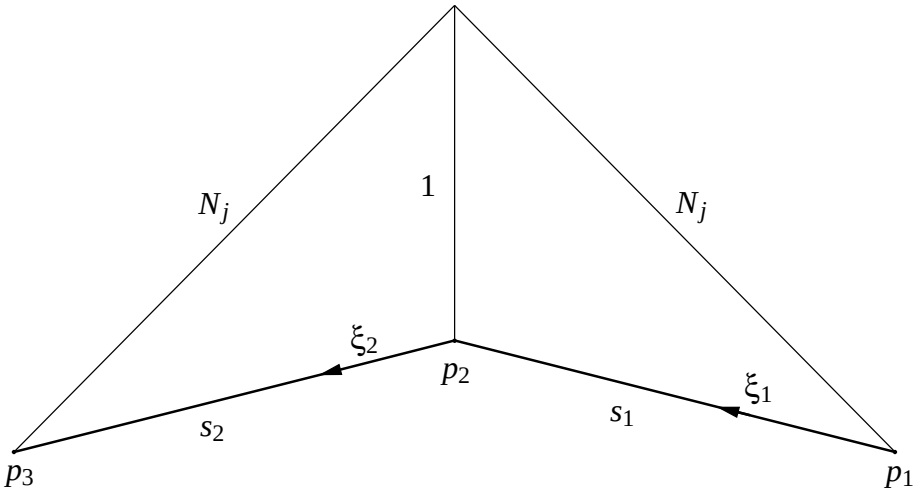

Figure B.1: Shape function N_j for a linear approximation. This example illustrates two boundary elements with the points $p1$, $p2$, and $p3$.

other words, one row is calculated by the solution of the boundary integrals for $G = N_j$. For each nodal point of the boundary element mesh, a distinct row of the gradient and Hessian is obtained. The integrals are written in terms of the local coordinates ξ_1 and ξ_2. The linear approximations of the functions F, G, and κ are written for the first boundary element as

$$\begin{aligned} F &= F_1(1-\xi_1)+F_2\xi_1 && \text{(B.3)}\\ G &= \xi_1 && \text{(B.4)}\\ \kappa &= \kappa_1(1-\xi_1)+\kappa_2\xi_1 && \text{(B.5)} \end{aligned}$$

and for the second boundary element one has

$$\begin{aligned} F &= F_2(1-\xi_2)+F_3\xi_2 && \text{(B.6)}\\ G &= 1-\xi_2 && \text{(B.7)}\\ \kappa &= \kappa_2(1-\xi_2)+\kappa_3\xi_2 && \text{(B.8)} \end{aligned}$$

The tangential gradient, which occurs in term $\mathcal{A}$, is for the first boundary element equal to $\frac{F_2-F_1}{s_1}$ and is a vector in tangential direction from $p1$ to $p2$. A similar result is obtained for the second boundary element. With these definitions the integral $\mathcal{B}$ yields

$$\int_\Gamma \kappa G \,\mathrm{d}s = \frac{1}{6}(\kappa_1+2\kappa_2)s_1+\frac{1}{6}(2\kappa_2+\kappa_3)s_2 \tag{B.9}$$

and it defines one element of $\vec{k}$. The integral $\mathcal{A}$ yields

$$\int_\Gamma \nabla_\Gamma F\cdot\nabla_\Gamma G \,\mathrm{d}s = \underbrace{-\frac{1}{s_1}}_{a}F_1+\underbrace{\left(\frac{1}{s_1}+\frac{1}{s_2}\right)}_{b}F_2\underbrace{-\frac{1}{s_2}}_{c}F_3 \tag{B.10}$$

and it defines one row of $\mathbf{L}$. The coefficients a, b, and c are the elements in the corresponding column (To find the correct column, one has to transform the local indices into global ones). The coefficient b is positive and is an element on the leading diagonal. The matrix $\mathbf{L}$, which is the discrete and negative Laplace-Beltrami operator, is positive definite and symmetric.

B.2 Squared Jump and Arc Length

Recall the shape derivatives of the the regularization term (4.5).

$$\mathrm{d}R_{SJ}(\Gamma;\vec{V}_G) = \underbrace{(\varepsilon_1-\varepsilon_2)^2\int_\Gamma \kappa G\,\mathrm{d}s}_{\mathcal{C}} + \underbrace{2(\delta\varepsilon_1-\delta\varepsilon_2)(\varepsilon_1-\varepsilon_2)\int_\Gamma \mathrm{d}s}_{\mathcal{D}} \tag{B.11}$$

$$\begin{aligned}\mathrm{d}^2R^*_{SJ}(\Gamma;\vec{V}_F;\vec{V}_G) = &\underbrace{(\varepsilon_1-\varepsilon_2)^2\int_\Gamma \nabla_\Gamma F\cdot\nabla_\Gamma G\,\mathrm{d}s}_{\mathcal{E}} + \underbrace{2(\varepsilon_1-\varepsilon_2)^2\int_\Gamma \kappa^2 FG\,\mathrm{d}s}_{\mathcal{F}}\\ &+\underbrace{2(\delta\varepsilon_1-\delta\varepsilon_2)^2\int_\Gamma \mathrm{d}s}_{\mathcal{G}} + \underbrace{2(\delta\varepsilon_1-\delta\varepsilon_2)(\varepsilon_1-\varepsilon_2)\int_\Gamma \kappa(F+G)\,\mathrm{d}s}_{\mathcal{H}}.\end{aligned} \tag{B.12}$$

The discretization of these integrals is a complex task. Different to section B.1, the material values are unknown as well. The aim of this section is to find vector and matrix representation of these shape derivatives in the form

$$\underbrace{\begin{pmatrix}\mathbf{L}_{11} & \mathbf{L}_{12}\\ \mathbf{L}_{21} & \mathbf{L}_{22}\end{pmatrix}}_{\mathbf{G}_2}\vec{\delta} = -\underbrace{\begin{pmatrix}\vec{k}_1\\ \vec{k}_2\end{pmatrix}}_{\vec{g}_2} \tag{B.13}$$

where the same notation as in section 3.2.1 is used to denote the Hessian and the gradient, i.e. $\mathbf{G}_2$ and $\vec{g}_2$. The step $\vec{\delta}$ indicates the change in geometry and material values

$$\vec{\delta} = \begin{pmatrix}\vec{F}\\ \vec{\delta\varepsilon}\end{pmatrix}. \tag{B.14}$$

The terms in the shape derivatives and the vectors and matrices can be identified as follows,

- $\vec{k}_1$ (size n_j) and term $\mathcal{C}$,
- $\vec{k}_2$ (size n_l) and term $\mathcal{D}$,
- $\mathbf{L}_{11}$ (size $n_j \times n_j$) and terms $\mathcal{E}$ and $\mathcal{F}$,
- $\mathbf{L}_{22}$ (size $n_l \times n_l$) and term $\mathcal{G}$,

- $\mathbf{L}_{12}$ (size $n_j \times n_l$) and $\mathbf{L}_{21}$ and term $\mathcal{H}$,

In the following paragraphs each component is discussed for itself. For better understanding it is useful to consider following equation

$$\begin{pmatrix} \vec{G} \\ \vec{\delta\varepsilon} \end{pmatrix}' \begin{pmatrix} \vec{k}_1 \\ \vec{k}_2 \end{pmatrix}, \tag{B.15}$$

which is the discrete version of (B.11). The discrete version of the Hessian (B.12) is

$$\begin{pmatrix} \vec{G} \\ \vec{\delta\varepsilon} \end{pmatrix}' \begin{pmatrix} \mathbf{L}_{11} & \mathbf{L}_{12} \\ \mathbf{L}_{21} & \mathbf{L}_{22} \end{pmatrix} \begin{pmatrix} \vec{F} \\ \vec{\delta\varepsilon} \end{pmatrix}. \tag{B.16}$$

Vector $\vec{k}_1$. Term $\mathcal{C}$ is similar to term $\mathcal{B}$ of section B.1 and the same discretization of the integral is used. This leads to

$$\vec{k}_1 = (\varepsilon_1 - \varepsilon_2)^2 \vec{k}. \tag{B.17}$$

Vector $\vec{k}_2$. This vector corresponds to term $\mathcal{B}$. The arc length, denoted by s, is calculated easily by the sum over all boundary elements. The vector is defined by

$$\vec{k}_2 = 2s(\varepsilon_1 - \varepsilon_2) \begin{pmatrix} 1 \\ -1 \end{pmatrix} \tag{B.18}$$

Note that this simple structure is obtained under the assumption that only one level set function exists. However, for more than two regions a similar result is obtained.

Matrix $\mathbf{L}_{11}$. This part of the Hessian is independent of the change in the material value. Term $\mathcal{E}$ is similar to the already calculated term $\mathcal{A}$. The discretization of term $\mathcal{F}$ is missing. The discrete counterpart of the integral in term $\mathcal{F}$ is denoted by $\mathbf{L}^*$ (size $n_j \times n_j$). Following equation defines one row of this matrix and it is obtained by the substitution of the linear approximations for F, G, and κ.

$$\begin{aligned} \int_\Gamma \kappa^2 FG \, \mathrm{d}s = \frac{1}{60} [& (3\kappa_1{}^2 + 4\kappa_1\kappa_2 + 3\kappa_2{}^2) s_1 F_1 \\ & + (12\kappa_2{}^2 + 6\kappa_1\kappa_2 + 2\kappa_1{}^2) s_1 F_2 \\ & + (12\kappa_2{}^2 + 6\kappa_2\kappa_3 + 2\kappa_3{}^2) s_2 F_2 \\ & + (3\kappa_2{}^2 + 4\kappa_2\kappa_3 + 3\kappa_3{}^2) s_2 F_3] \end{aligned} \tag{B.19}$$

The coefficients of F_1, F_2, and F_3 (local indices) are the values in their corresponding columns (global indices). The matrix $\mathbf{L}^*$ is again symmetric and positive definite. This part of the shape Hessian is defined as follows.

$$\mathbf{L}_{11} = (\varepsilon_1 - \varepsilon_2)^2 (\mathbf{L} + 2\mathbf{L}^*) \tag{B.20}$$

Matrix $\mathbf{L}_{22}$. This part of the Hessian is determined by $\mathcal{G}$. It only depends on the change in the material values. The integral over the boundary, the arc length of the interface, is denoted by s.

$$\mathbf{L}_{22} = 2s \begin{pmatrix} 1 & -1 \\ -1 & 1 \end{pmatrix} \tag{B.21}$$

Matrices $\mathbf{L}_{12}$ and $\mathbf{L}_{21}$. The term $\mathcal{H}$, which corresponds to these matrices, consists of a combination of change in shape and material. The term

$$2(\delta\varepsilon_1 - \delta\varepsilon_2)(\varepsilon_1 - \varepsilon_2) \int_\Gamma \kappa G \, \mathrm{d}s \tag{B.22}$$

defines the matrix $\mathbf{L}_{12}$. The integral is equal to term $\mathcal{B}$ (its discretization is denoted by $\vec{k}$). Thus, the matrix is defined by

$$\mathbf{L}_{12} = 2(\varepsilon_1 - \varepsilon_2) \begin{pmatrix} \vec{k} & -\vec{k} \end{pmatrix}. \tag{B.23}$$

The matrix $\mathbf{L}_{21}$ corresponds to

$$2(\delta\varepsilon_1 - \delta\varepsilon_2)(\varepsilon_1 - \varepsilon_2) \int_\Gamma \kappa F \, \mathrm{d}s. \tag{B.24}$$

The discrete version of this integral leads to ${\mathbf{L}_{12}}^T$ (not shown here) and the resulting Hessian matrix is symmetric.